12-5-2017

Development of Molecular Catalysts for CO2 Reduction and Nanomaterial Catalysts for Oxidation Reactions

Kankana Mullick
University of Connecticut, kankana.mullick@uconn.edu

Development of Molecular Catalysts for CO_2 Reduction and Nanomaterial Catalysts for Oxidation Reactions

Kankana Mullick

University of Connecticut, 2017

The thesis presented here is focused on two aspects of transition metal mediated catalysis research- one is designing homogeneous rhenium complex with suitable ligand framework for electrochemical reduction of carbon dioxide to address dual issues regarding green house gas removal and hydrocarbon fuel production; another being fabrication of heterogeneous mesoporous manganese oxide to catalyze organic fine chemical synthesis under aerobic atmospheric condition. The quest for conquering fossil fuel energy dependence leads us to develop methodologies for using CO_2 as a renewable resource. Electrochemical reduction of CO_2 has been considered as a promising procedure for this purpose. Coordination complexes of rhenium and α-diimine ligands are known to resolve the bottleneck of activating the thermally stable and kinetically inert CO_2 molecule. In the beginning of the thesis, I have described the development of a new family of α-diimine ligand coordinated rhenium complexes that exhibits remarkable catalytic activity compared to the existing list of analogous systems. The reported compounds in this work consist of three different ligand systems- quinoline, naphthyridine and benzonaphthyridine bound to pyridine or thiazole moieties in the coordination sphere. It has been shown that rate of CO_2 reduction and turn over frequency depends significantly on the nature of the ligands. Overall, complexes that have pyridine

outperform those having thiazole, with the benzonaphthyridine complexes showing superior activity with rate constant and catalytic turnover of 10^3 orders.

The second part of my thesis describes the design and application of thermally stable and tunable mesoporous manganese oxide to catalyze coupling and aromatization reactions. From the viewpoint of green chemistry, synthesizing valuable organic molecules by using no or minimum additive and maintaining mild reaction condition is of utter importance. We demonstrate synthesis of aromatic nitrogen containing heterocyclic molecules from their non aromatic counterparts by employing robust and inexpensive manganese oxide catalyst in the presence of no other oxidant/additive but air. The same manganese oxide material when fabricated to act as a support for copper oxide catalyst exhibited excellent efficiency for C-O, C-N and C-S bond formation in Ullmann type reaction. Not only the synthetic methodology but the underlying mechanism and role of lattice oxygen present in the structure of catalyst are explained in details following experimental and theoretical studies. The catalytic protocols discussed here have several advantages over the already reported procedures in terms of product separation, reusability of the catalyst, absence of additive, water as by product and air as the terminal oxidant.

Development of Molecular Catalysts for CO_2 Reduction and Nanomaterial Catalysts for Oxidation Reactions

Kankana Mullick

B.Sc., Calcutta University, Kolkata, India. 2008

M.Sc., Indian Institute of Technology, Madras, India. 2011

A Dissertation

Submitted in Partial Fulfillment of the

Requirement for the Degree of

Doctor of Philosophy

At the

University of Connecticut

2017

APPROVAL PAGE

Doctor of Philosophy Dissertation

Development of Molecular Catalysts for CO_2 Reduction and Nanomaterial Catalysts for Oxidation Reactions

Presented by

Kankana Mullick

Major Advisor_____

Alfredo Angeles-Boza

Associate Advisor_____

Nicholas Leadbeater

Associate Advisor_____

Mark Peczuh

University of Connecticut

2017

Dedicated to my parents, my sister and my beloved husband

Acknowledgements

First and foremost I would like to express my sincere gratitude to my major advisor, Dr. Alfredo Angeles-Boza for his patience, motivation, enthusiasm, immense knowledge and continuous support throughout my study and research. I appreciate all of his contributions of time and resource whilst allowing me the room to work in my own way.

I would like to thank my associate advisors Dr. Nicholas Leadbeater, Dr. Mark Peczuh, Dr. Jing Zhao and Dr. Fatma Selampinar for their guidance, encouragement and insightful comments.

I thank my fellow lab mates- John Nganga, Taylor Schneider, Daben Libardo and Samuel Juliano. Their cheerful, friendly and helpful nature had been a great support from the beginning to the end of my Ph.D. career.

My appreciation goes to the people from Dr. Suib's group - Dr. Lakshitha Pahlagedara, Dr. Saiful Seraji, MD Shakil, Biswanath Dutta and Harshul Khanna who have helped me a lot during my stay here at UConn.

A special note of gratitude goes to Shamima Nasreen for being a wonderful friend, in every way.

I am grateful to the Department of Chemistry, University of Connecticut and its employees for their support during my graduate studies. Special thanks to Dr. You-Jun Fu, Charlene Fuller, and Ashley Orcutt for their assistance. I also acknowledge the financial support from the Graduate School of the University of Connecticut.

I also want to thank my parents and my sister; they are God's gift to me. Lastly, I would like to express my heartiest gratitude to my husband Dr. Sourav Biswas for the endless love and support he has bestowed on me standing beside me like bedrock.

Table of Contents

Chapter 4. Heterogeneous Mesoporous Manganese Oxide Catalyst for Aerobic and Additive-Free Oxidative Aromatization of *N*-Heterocycles

LIST OF FIGURES

LIST OF TABLES

LIST OF SCHEMES

CHAPTER 1. Introduction

1.1 Catalysis- homogeneous and heterogeneous

In the history of chemical science, the term 'catalyst' was first mentioned by Berzelius (in 1836) to describe a promoting reagent in a reaction. Since then catalysis have emerged as the eminent method to speed up reaction rates in research and development as well as industrial processes. A steady growth in the field of catalysis has occurred during the twentieth century leading to the current situation when ~ 95% chemical production goes through at least one catalytic step. A catalyst can have dual role in a reaction- acceleration of reaction rate by lowering activation energy barrier and/or modification of the product distribution by offering a new reaction pathway under kinetically controlled setting.[1]

Depending on the coherence of phases catalysts are classified as- homogeneous, when the catalyst and the substrate are in same phase, typically liquid phase; and heterogeneous, when the catalyst is solid but the reaction occurs in liquid (or gas) phase. Needless to say, both types having their own advantages and drawbacks, have found paramount importance in science and engineering.

Homogeneous catalysts can be metal complexes, Bronsted and Lewis acids/bases, organometallic compounds, metal ions and enzymes. As the catalyst mixes into the reaction mixture, it allows a very high degree of interaction between catalyst and the reaction molecules. On the other hand, the surface of a heterogeneous catalyst possesses the active sites where reactant molecules get adsorbed first, followed by reaction and desorption of product. Examples of such systems are metal oxides and supported metal particles. Therefore not only

the chemical composition of the catalyst but the particle dimension and surface area plays a major role in its performance. Additionally, choice of support becomes a critical variable in order to obtain the desired functionality. Depending on the nature of the support complete alteration, prevention or improvement in the course of the reaction can be achieved. In terms of product separation, a heterogeneous system having easy and inexpensive isolation is superior to homogeneous methods. Moreover longer shelf-life, higher thermal stability and steady reproducibility of heterogeneous catalysts have led to its use in processes such as, hydrogenation, fuel cell, catalytic converter and ammonia synthesis.[2-5] A concise list of comparative features of homo and heterogeneous catalysts is depicted in table 1.

Table 1. Comparison between homogeneous and heterogeneous catalyst

Property	Homogeneous	Heterogeneous
Thermal stability	poor	good
Active center	all atoms	only surface atoms
Selectivity	high	low
Structure/mechanism	defined	undefined
Catalyst separation	tedious	easy
Reusability	difficult, costly	easy, cheap

1.2 Overview of carbon dioxide reduction

Amidst the current political and scientific debate on 'climate change', the effect of green house gases calls for major attention. An integral part of the issue is continuous elevation in carbon dioxide concentration in the atmosphere. Current concentration of CO_2 in the atmosphere is about 0.04% or 400 parts per million (ppm).[6] Despite being a trace amount, CO_2 is the most important long lived global warming gas, and its concentration has increased

steadily from 280 ppm in the 1950s to current levels.[6] The presence of CO_2 is inevitable as is part of the carbon cycle in biogeochemical sphere. The amount of CO_2 added in atmosphere by respiration, decomposition, fire and aquatic release gets compensated by photosynthesis and oceanic dissolution, 120 and 115 Gt C yr^{-1}. However anthropogenic emissions due to fossil fuel burning, cement manufacture and land use raise the amount by 5-8Gt C yr^{-1}, that unfortunately causes imbalance in atmospheric CO_2 compensation.[7] An obvious solution to improve the situation seems to be reducing emission of carbon dioxide that can be achieved by decreasing our dependence on fossil fuels for energy. Another promising path is carbon capture and sequestration under ocean or soil. A more feasible and alluring process is chemical or electrochemical transformation of carbon dioxide to useful organic chemicals. Quite a few chemicals, urea, salicylic acid, methanol and polycarbonates are being produced from carbon dioxide. But the extent of research in CO_2 activation is still limited compared to the necessary action of limiting CO_2 emission by 50-80% by 2050.[8]

1.2.1 Process of activation of CO_2 by metal complexes

Both homogeneous and heterogeneous catalysts have been employed in CO_2 activation by thermal, photochemical, biochemical and electrochemical procedure.[9-12] In our study we have focused on homogeneous molecular electrocatalysis by rhenium complexes.

Carbon dioxide can act as a monodentate ligand or a bridging ligand depending upon the number of metals it is binding to. In our work we mostly concentrate in mononuclear complexes of CO_2 hence we pay the most attention to the possible binding modes of CO_2 to only one transition metal center (figure 1.1). CO_2 is a linear triatomic molecule having sp

hybridization on the central carbon atom and C-O bond length 1.16Å, shorter than that of sp^2 C-O bond. Due to difference in electronegativities carbon gets partial positive charge while oxygen atoms gain partially negative polarization. These characteristics generate different electronic features on C, O and π-bond and affects metal binding mode. In detail, the central carbon in CO_2 acts as a Lewis base and coordinates with electron rich metals; terminal oxygen may behave as Lewis acid and hence tend to bond with electron deficient metals; the π-bond can participate in π-complexation upon suitable matching of orbitals (Dewar-Chatt-Duncanson). The first two binding modes- η^1 (C) and side on η^2 (C, O) were observed in $[Rh(diars)_2(Cl)(\eta^1\text{-}CO_2)]$ and in $[Ni(\eta^2\text{-}CO_2)(PCy_3)_2]$, respectively, by x-ray crystallography. The η^1 (C) mode is usually favorable for such transition metal fragment where metal is in a low oxidation state and has high energy, doubly occupied dσ orbital. Whereas, η^2 (C, O) binding is predominant for metals having filled high energy dπ and empty dσ orbitals. In literature occurs a variety of such complexes bearing η^2 (C, O) mode- $[Ni(\eta^2\text{-}CO_2)(PR_3)_2]$ (R= Cy, Ph, Bu, Et); $[Fe(\eta^2\text{-}CO_2)(PMe_3)_4]$; $[Cp_2Mo(\eta^2\text{-}CO_2)]$; *trans*-$[Mo(\eta^2\text{-}CO_2)_2(Me_3)_4]$.[13,14]

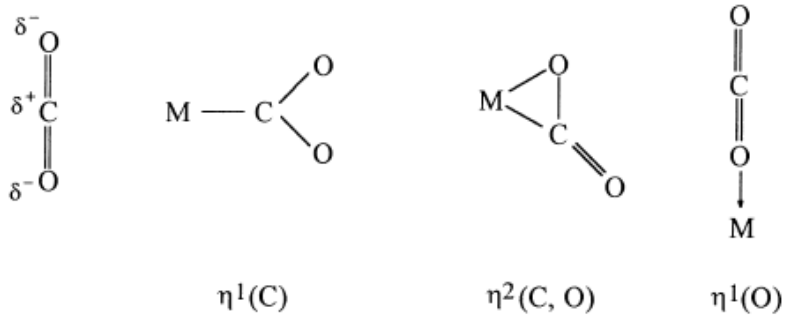

Figure 1.1 Possible binding modes of CO_2

1.2.2 Molecular electrocatalysts for CO_2 reduction

Early twentieth century marks the beginning of CO_2 electroreduction by metal cathodes. The most crucial challenge the researchers had to face was overcoming the unfavorable one electron reduction of CO_2 to $CO_2^{-\bullet}$ for its very high formal reduction potential, -2.14Vvs SCE. Upon gaining an electron, linear CO_2 transforms to bent species and this structural rearrangement causes kinetic restrictions, resulting in 0.6V overpotential for rapid reduction. An alternative is reducing CO_2 through proton coupled multi-electron transfer pathways as shown below.

$$CO_2 + 2H^+ + 2e^- \longrightarrow CO + H_2O,\ E^{\circ\prime} = -0.52V$$

$$CO_2 + 2H^+ + 2e^- \longrightarrow HCOOH,\ E^{\circ\prime} = -0.61V$$

$$CO_2 + 4H^+ + 4e^- \longrightarrow HCHO + H_2O,\ E^{\circ\prime} = -0.48V$$

$$CO_2 + 6H^+ + 6e^- \longrightarrow CH_3OH + H_2O,\ E^{\circ\prime} = -0.38V$$

$$CO_2 + 8H^+ + 8e^- \longrightarrow CH_4 + 2\ H_2O,\ E^{\circ\prime} = -0.24V$$

Employing metal cathodes for CO_2 reduction in aqueous or protic solvent has been emerged as a well accepted technique. Various metals have moderate to excellent performance in this method of CO_2 catalysis- mercury cathode produced oxalate; iridium worked in low overpotential; rhodium and ruthenium produced highly reduced products, methanol and methane but with low selectivity; molybdenum yielded methanol at low overpotential whereas copper produced methane; gold too, transformed bicarbonate to CO with high faradaic efficiency.

A simpler and more convenient method is to exploit solution state electrocatalysis, where the catalyst (preferably a molecular catalyst) remain dissolved in a solution of supporting electrolyte in presence of a chemically inert cathode (scheme 1.1)

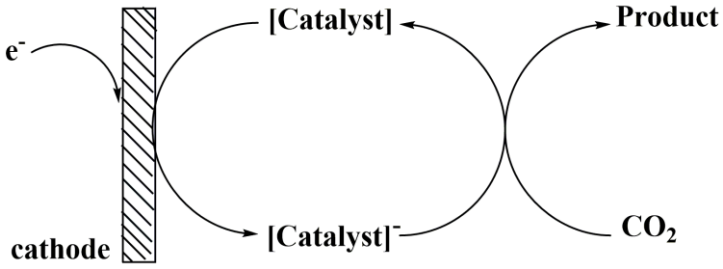

Scheme 1.1 General working principle of soluble molecular electrocatalyst

in an electrochemical cell. These systems can be classified in two major groups- transition metals with i) macrocyclic ligands and ii) bipyridine and similar aromatic ligands. Again, macrocyclic ligands can have two subdivisions- a) porphyrins and phthalocyanines and b) non-porphyrinic ligands.[15,16]

Macrocyclic ligands

Water soluble tetrasulphonated phthalocyanine complexes of nickel and cobalt are the first examples of macrocyclic ligands taking part in CO_2 electrocatalysis. In 1991, Saveant reported Fe(0)-porphyrin compound as an effective CO_2 reduction catalyst to produce CO.[17,18] They were also able to improve the stability and turnover of the catalyst by using alkali/alkaline metal ions or weak Bronsted acid cocatalyst.[19] In subsequent times Co(II), Ag(II), Pd(II)-porphyrin and zinc porphyrin- rhenium bipyridyl dyad complexes have been explored to reach several reduction products from CO_2 depending upon solvent and electrolyte.[20-22] Corrole ring bearing cobalt and iron also acted as strong reducing catalyst for CO_2.[23] Porphyrin like metal

functionalized graphene[24] and cobalt porphyrin- derived two dimensional organic frameworks[25] are few examples of modern research progress in this area.

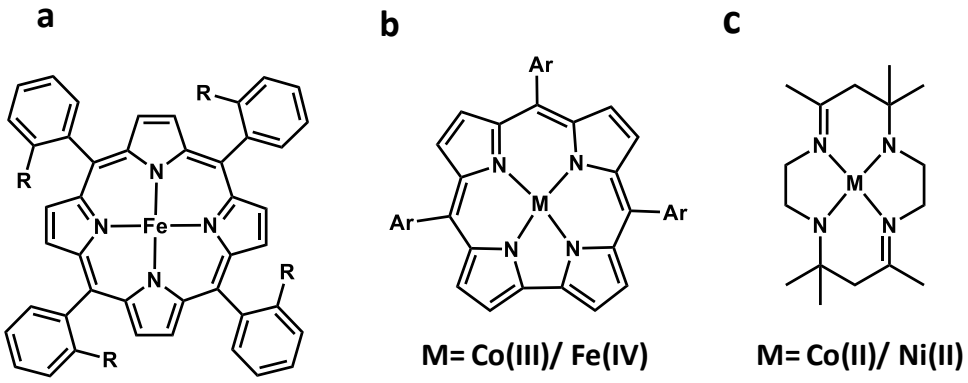

Figure 1.2 Metal macrocycles- a) tetraphenylporphyrin, b) corrole, c) cyclam

Popular macrocycles other than porphyrin are 1,4,8,11-tetraazatetradecane or commonly known as cyclam. Nickel(II) cyclam complexes are exceptional CO_2 reduction catalysts in terms of stability, high turnover frequency (TOF~ 10^2 cycles h^{-1}), low reduction potential and high selectivity in CO formation.[26,27] Nevertheless, these systems necessitate mercury metal electrode and cannot be considered as environmentally benign.

Bipyridine and other nonporphyrin ligands

An important and vastly surveyed field is CO_2 electrocatalysis by transition metal complexes bipyridine (bpy) and its derivatives. The first report was CO_2 electro reduction to CO by *fac*-Re(bpy)$(CO)_3$Cl following previous outcome of photochemical reduction by the same compound.[28] Noteworthy features of this system were simple catalyst preparation, remarkably high CO conversion (faradaic efficiency 98%) at a small applied potential, -1.5V vs. SCE and selectivity towards CO_2 reduction over proton reduction to hydrogen gas, even in presence of a large concentration of water (DMF: H_2O= 9:1, v/v). Eventually similar systems

with modification of the ligand, central metal ion and coordinating anion were studied. Some examples include $Ru(bpy)_2(CO)_2^{2+}$, $Ru(bpy)_2(CO)Cl^+$, $Rh(bpy)COD^+$, *cis*-$Ir(bpy)(CF_3SO_2)_2^+$, $Ru(terpy)(dppene)Cl^+$, $Ru(\eta^6\text{-}C_6H_6)(bpy)Cl^+$ etc. although having high current efficiency, a major drawback of most of these systems is low turnover frequency, 8-20 cycles h^{-1}.[15]

Phosphine and its derivatives have been successfully used as ancillary ligands in transition metal centered electrocatalysts designed for CO_2 reduction.[29] A rhodium complex with 1,2-bis(diphenylphosphino)ethane, $[Rh(dppe)_2Cl]$ was an early example that a catalyst can generate formate from CO_2, albeit with poor efficiency, 20-40%. Dubois explored the reduction chemistry of $[Pd(triphos)(PR_3)](BF_4)_2$, (R= Ethyl, phenyl, methoxy and acetonitrile) and proposed a mechanism[30] starting from Pd(II) converting to a coordinatively unsaturated solvato complex as shown in scheme 1.2. In terms of kinetics, Pd-complexes are favorable (reaction rate~10-300 $M^{-1}S^{-1}$) with high efficiency for CO production (> 90%) but exhibit low turnover~10-100 h^{-1}. Other than Pd, several binuclear nickel and copper complexes have been designed to achieve CO_2 reduction with moderate efficiency. Examples are- $[Ni_2(CNMe)_3(dppm)_2][PF_6]_2$, $[Cu_2(\mu\text{-}PPh_2bipy)_2(MeCN)_2][PF_6]_2$ (PPh_2bipy = 6-diphenylphosphino-2,2'-bipyridyl) and its pyridine analog.

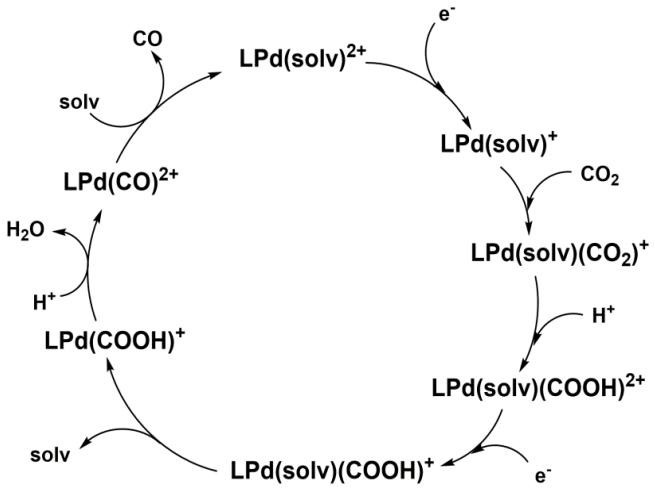

Scheme 1.2 Proposed mechanism for Pd-phosphine catalyst

As a substitute of inert transition metals cathodes or soluble metal complex, there exist surface depositions of molecular electrocatalysts on electrode. Examples are- palladium or platinum embedded in conducting polymers, transition metal (Ni, Co) phthalocyanine deposited on glassy carbon electrode.[15]

1.2.3 Rhenium and manganese complexes as modern electrocatalysts

Since the advent of CO_2 catalysis researchers have continuously searched for homogeneous electrocatalysts that may deliver selective product maintaining a faster kinetics in a scaled up condition. *fac*-Re(bpy)$(CO)_3$Cl complex and its analogs have served the purpose in many desired aspects. The earliest congener was *fac*-Re(phen)$(CO)_3$X, (phen= 1,10-phenanthroline, X= Cl, Br, I), synthesized from rhenium pentacarbonyl halides and phenanthroline in 1941 by Hieber. The facial geometry was observed via infrared spectroscopy by Abel and Wilkinson. Fifteen years later Wrighton and his coworkers came up with the photochemical properties of the complex. In 1983, photochemical reduction of CO_2 to CO by

the same complex was reported by Hawecker, Lehn and Ziessel.[31] To avoid the use of large amount of sacrificial electron donor in photocatalysis, the same catalyst was employed in electrochemical set up to obtain 98% (faradaic efficiency) CO production at -1.5v vs. SCE.[28] The underlying mechanism was discovered by Meyer in 1985. According to their proposal, *fac*-Re(bpy)$(CO)_3$Cl undergoes a quasireversible reduction at first indicating reduction of π^* orbital of the ligand. A second reduction takes place leading to the formation of Re(0) and halide loss. Instant attention to the underlying mechanism suggested possibility of two routes, slower $1e^-$ and rapid $2e^-$ pathway (Scheme 1.3). An oxide acceptor (A) was proposed for the two electron pathway. The monoreduced species $[Re(bpy^{\bullet -})(CO)_3X]^-$ have been also observed by Kaim via electron paramagnetic spectroscopy (EPR) and Re-X bond weakening was explained by σ/π^* mixing occurred by bpy ligand reduction.[32] Later, Wong and his coworkers discovered that the reduction is favored by the presence of Bronsted acid by adding water, methanol, trifluoroethanol and phenol.

In an effort to enhance the catalytic ability derivatives of bipyridine ligands were employed. A good number of such compounds *fac*-Re(bpy-R)$(CO)_3$Cl (R= Me, COOH, t-Bu, OMe) were studied by Kubiak's research group that showed presence of *tert*-butyl on bipyridine increases 10 times catalytic current compared to the Lehn's catalyst.[33]

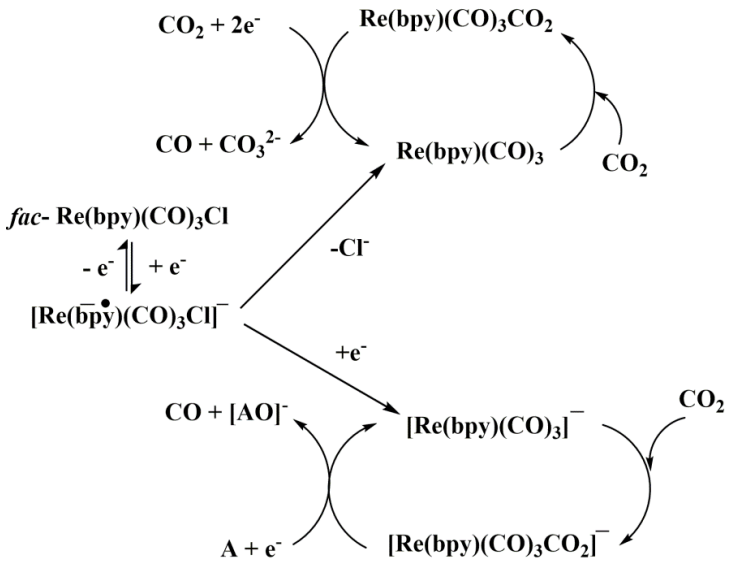

Scheme 1.3 $1e^-$ and $2e^-$ reduction pathways by *fac*-Re(bpy)$(CO)_3$Cl proposed by Meyer

Substitution at 5,5'-position of bpy also led to the effective catalytic output in the complex, *fac*-Re(5,5'-bisphenylethynyl-2,2'-bipyridine)$(CO)_3$Cl.[34] In order to identify the reason for the excellence in CO_2 reduction performed by Re-bpy type complexes, several strategies were employed. Previously postulated active catalyst $[Re(bpy\text{-}tBu)(CO)_3]^{-1}$ generated from the neutral complex was made to react with protons and CO_2 separately. Surprisingly the anion reacted about 35 times faster with CO_2 than with H_2O, consistent with the preferred selectivity observed during CO_2 reduction in the presence of water. DFT theory also suggested two types of interactions, σ and π, in Re-CO_2 adduct upon coordination that enhanced the stability over proton adduct.[35,36]

Recent studies have drawn attention to use of more earth abundant metal ions, specifically manganese to replace rhenium. In 2011, Deronzier and coworkers reported *fac*-Mn(bpy-R)$(CO)_3$Br, (R=H/Me) to reduce CO_2 at a lower overpotential in presence of a proton

source.[37] Two years later Kubiak reported activity enhancement of *fac*-Mn(bpy-*t*Bu)$(CO)_3$X comparable to its rhenium analogs[38] as shown in table 1.2.

Table 1.2 Activity comparisons between bpy complexes of Mn and Re

	Mn(bpy-*t*Bu)$(CO)_3$Br			Re(bpy-*t*Bu)$(CO)_3$(MeCN)(OTf)			
Acid	[Acid] (M)	i_{cat}/i_p	TOF (s^{-1})	[Acid] (M)	i_{cat}/i_p	TOF (s^{-1})	TOF_{Mn}/TOF_{Re}
None	0.0	1.0	0	0.0	3.3	2.1	-
H_2O	3.1	25	120	10	9.0	16	7.5
MeOH	5.8	26	130	9.9	42	340	0.38
TFE	1.4	42	340	1.6	54	570	0.60

Bocarsly and coworkers have designed a Mn-bpy complex with phenol substitution to obtain intramolecular hydrogen bonding that stabilized Re-CO_2 adduct hence improved catalysis.[39] Non aromatic α-diimine ligands are useful to catalyze CO_2 reduction. Examples are Re and Mn complexes bearing 1,4-diazabutadiene ligand.[40]

Despite the growth in the field of CO_2 reduction catalysis by *fac*-M(bpy-R)$(CO)_3$X (M= Mn, Re) type systems, several future opportunities remain to be inquired. The mechanism of proton assistance for different proton sources has not been confirmed yet. Variation in the ligand structure and geometry and its relation to catalytic efficiency needs to be defined precisely. Also, it is important to know if presence of any heteroatom other than nitrogen in the coordination sphere can alter the nature of the catalyst or not. In addition more research has to be focused on the methods to attach these metal complexes on heterogeneous surfaces in order to broaden the scope and applicability.

1.3 Overview of catalytic oxidation and coupling reactions

Synthesis of fine chemicals by catalyst mediated oxidation procedure occupies a large segment of modern chemical industries. Selective oxidation step is utilized in more than 60% organic product and intermediate synthesis technology in the whole world.[41] Traditionally, stoichiometric oxidants such as permanganate or chromium salts were used to achieve oxidation of desired substrates. Peroxides and ozone gas were also given preference in this regard. However large amount of toxic waste generation, tedious product separation process and non-reusable reagents reduced their impact from both industrial as well as environmental perspective.[42]

Aryl-aryl bond formation strategies have gained paramount importance regarding their presence in natural products, pharmaceutical and agrochemical commodities. For more than a century copper has been used either in stoichiometric or catalytic amounts to promote C-C, C-O, C-N and C-S bond construction starting from aryl halides and nucleophiles containing heteroatom. Copper salts (CuBr, CuI, $CuCl_2$, Cu_2O, $Cu(NO_3)_2$, $Cu(OAc)_2$) and copper complexes have been proved to be efficient to generate desired coupled molecules.[43] Pd also have found significant application in innumerable coupling reactions- Miyaura-Suzuki reaction, Negishi reaction, Stille reaction, Sonogashira reaction, Hiyama reaction, Heck reaction, Buchwald-Hartwig coupling and many more.[44]

From the viewpoint of green chemistry, designing novel methodologies that prefer aerobic atmospheric condition, null or minimum additive, less waste production and stable as well as reusable catalyst is highly desirable. Heterogeneous catalysts although a newer field of research, draw attention for being capable of solving the purpose with excellent catalyst turn over and stability.

1.3.1 Heterogeneous catalysis- manganese oxide

A vast majority of catalytically driven reactions fall under heterogeneous catalysis where the catalyst and the substrates are in two different phases. Generally the catalyst is solid while the substrates may be liquid or gas. Phase mismatch gives an instant relief from tiresome catalyst separation step, making the process advantageous over homogeneous systems.[45] The key to understand the mechanism of heterogeneous catalysis is to deduce the relationship between the reactants and the surface of the catalyst where the reaction happens at a definite pressure and temperature. Roughly, the reactants are adsorbed on active sites of the catalyst prior reaction; thereby reactivity increases with number of available active sites and surface area. A strategy to maintain cost effectiveness is to disperse the active sites (mostly valuable transition metals) on cheaper, readily abundant supports (like silica, alumina or carbon).

Three types of mechanisms have been proposed for heterogeneous catalysis[46]

Langmuir-Hinshelwood mechanism: All reactants get adsorbed on the surface of the catalyst followed by interaction and desorption. Example is Pt mediated reduction of nitric oxide by carbon monoxide.

Eley-Rideal mechanism: A reactant staying in gas phase reacts with the second reactant that is adsorbed on the surface of the catalyst. Desorption of the product occurs at the end. Hydrogenation of CO_2 to produce formate can be considered as an example, H_2 gas being the adsorbed reactant.

Mars-Van Krevelen mechanism: Surface plays an active role as one reagent forms a chemical bond with it; the other reagent staying in its phase reacts with the atoms of the bound substrate followed by desorption of the product. A common example is CO oxidation on Pt surface in oxygen environment.

Porous nanostructure materials have emerged as popular heterogeneous catalysts for their high surface area, ability to incorporate active metal center and porosity dependent shape selective catalysis.[47] Discovery of mesoporous silica and aluminosilicate (M 41S family) mediated catalysis in 1992 by Mobil Oil Corporation opened the avenue of research on mesoporous catalysts and its applications.[48] According to the IUPAC definition, materials with pore size 2-50 nm can be named mesoporous. High surface area and pore volume, tunable porous network, nanocrystalline wall structure and diverse morphology are few characteristics for which mesoporous materials may have distinct physicochemical and catalytic properties compared to their non-porous counterparts.

Mesoporous transition metal oxides (MTMO) have shown impressive catalytic performance in oxidation-reduction reactions due to variable valencies in transition metals acting as active sites.[49] Manganese oxide has secured a well-deserved position in catalysis ground for its exclusive properties- exhibition of several oxidation states (from 2^+ to 7^+) hence proficient electron mediator, possession of more than 30 thermally stable structural forms, high abundance, ability to tether promoter ions and accessibility to lattice oxygen favoring oxidation.[50] Depending on diverse synthetic procedures structures with varying porosity and crystallinity can be prepared. A few examples are- octahedral molecular sieve (OMS), octahedral layer (OL), amorphous manganese oxide (AMO), birnessite, mesoporous manganese oxide etc.[50,51] OMS-2 ($KMn_8O_{16}nH_2O$, 2×2 tunnel structure having edge and corner shared MnO_6 octahedra) and AMO both have been utilized in numerous oxidation reactions including oxidation of alcohol, amine, hydrocarbon, styrene, volatile organic compound, methane, carbon monoxide and water oxidation.[52-57]

Through our work we have expanded catalytic abilities of meso manganese oxide (UCT-MnOx, named after University of Connecticut)[58] in oxidative dehydrogenation and Ullmann coupling reaction.

1.3.2 Ullmann coupling by heterogeneous copper catalyst

Copper assisted (stoichiometric) synthesis of biaryl compounds starting from aryl halides is known as Ullmann reaction following its discoverer, Fritz Ullmann in 1901.[43] Within a few years the methodology was used for C-N (aryl-amine) and C-O (aryl ether) bond formation. In 1906, Irma Goldberg's copper catalyzed aryl-amide synthesis bolstered the effectiveness of copper as a catalyst. The remarkable work of Ullmann and Goldberg presented an easier and acceptable pathway for synthesizing organic molecules of medicinal, biological, agrochemical, polymeric and academic interest. To soften the harsh reaction condition originally employed by Ullmann (strong base, >200°C, narrow scope- electron withdrawing nucleophile) several copper centered homogeneous and heterogeneous catalysts have been introduced. Bidentate ligands such as aliphatic diamine, bipyridine, phenanthroline, hydroxyquinoline and phosphine served the purpose. Several heterogeneous catalysts have been engaged for the sake of avoiding ligand additives and improving stability, reusability and product isolation procedure.[59-61] Although the reaction is proposed to follow an organocopper intermediate, not much light has been shed onto the proper mechanistic details especially in case of heterogeneous surface oriented catalysis. In our group we have studied CuO supported on mesoporous manganese oxide to catalyze C-N, C-O and C-S bond formation and elucidate structure-activity relationship. We also took help of theoretical calculation to understand the behavior of the reagents towards surface promoted catalysis.

1.3.3 Aromatization of N-heterocycles by heterogeneous manganese catalyst

Organic family of compounds is known to have a sizable member which is heterocycles. Aromatic heterocycles is a versatile subclass that is found in biologically active natural and synthetic compounds, drug molecules and agrochemical products.[62] Nonetheless, aromatic heterocycles are also key ingredients for commercially valuable dye and polymer synthesis. A typical procedure for synthesis of heteroarenes is dehydrogenation of parent saturated cyclic compounds initially achieved by stoichiometric reaction of DDQ or sulfur.[63,64] It should be noted that dehydrogenation of N-heterocycles is thermodynamically uphill process but ring nitrogen reduces endothermicity and hydrogen release add positive entropy change. Transition metal centered molecular catalysts have outraced in modern time and can be divided in two categories based on the mechanism they follow- acceptorless dehydrogenation and oxidative dehydrogenation. Cp*Ir containing pyridine and pyridonate complex and Fe-pincer complexes are examples of the first category.[65,66] 1,10-phenanthroline-5,6-dione ligand combined with either Zn(II) or Ru(II) can aromatize N-heterocycles but only in presence of additives or co catalysts.[67] Substantial variety in heterogeneous catalysts is reported in literature. These are ruthenium supported on Al_2O_3, TiO_2 or Co_3O_4, CuAl-HT, Pd-HAP, Pd_3Pb, AuNPs/C, iron-nitrogen doped grapheme shell supported on carbon and cobalt oxide supported on N-doped carbon.[68,69] Despite high catalyst turnover and stability these systems require high oxygen pressure or cumbersome catalyst preparation strategy or basic/ligand additive for satisfactory results. Hence an inexpensive heterogeneous catalyst that can perform oxidative aromatic dehydrogenation in aerobic additive free condition is exquisitely desired.

We have designed mesoporous manganese oxide catalyst to achieve aromatization of tetrahydroquinoline, its derivatives and other N-heterocycles in air using no ligand or base or additive.

References

(1) Farnetti, E.; Di Monte, R.; Kašpar, J. *Inorganic and Bio-Inorganic Chemistry-Volume II* **2009**, *6*, 50.

(2) Astruc, D.; Lu, F.; Aranzaes, J. R. *Angew. Chem., Int. Ed.* **2005**, *44*, 7852-7872.

(3) Fadhel, A. Z.; Pollet, P.; Liotta, C. L.; Eckert, C. A. *Molecules* **2010**, *15*, 8400-8424.

(4) Copéret, C.; Chabanas, M.; Petroff Saint-Arroman, R.; Basset, J. M. *Angew. Chem., Int. Ed.* **2003**, *42*, 156-181.

(5) Corma, A.; Garcia, H. *Chem. Rev.* **2003**, *103*, 4307-4366.

(6) Monastersky, R. *Nature* **2013**, *497*, 13-14.

(7) Bowes, G. *Annual review of plant biology* **1993**, *44*, 309-332.

(8) Whipple, D. T.; Kenis, P. J. *The Journal of Physical Chemistry Letters* **2010**, *1*, 3451-3458.

(9) Mikkelsen, M.; Jørgensen, M.; Krebs, F. C. *Energy & Environmental Science* **2010**, *3*, 43-81.

(10) Sakakura, T.; Choi, J.-C.; Yasuda, H. *Chem. Rev.* **2007**, *107*, 2365-2387.

(11) Darensbourg, D. J. *Inorg. Chem.* **2010**, *49*, 10765-10780.

(12) Windle, C. D.; Perutz, R. N. *Coord. Chem. Rev.* **2012**, *256*, 2562-2570.

(13) Yin, X.; Moss, J. R. *Coord. Chem. Rev.* **1999**, *181*, 27-59.

(14) Leitner, W. *Coord. Chem. Rev.* **1996**, *153*, 257-284.

(15) Collin, J.; Sauvage, J. *Coord. Chem. Rev.* **1989**, *93*, 245-268.

(16) Benson, E. E.; Kubiak, C. P.; Sathrum, A. J.; Smieja, J. M. *Chem. Soc. Rev.* **2009**, *38*, 89-99.

(17) Hammouche, M.; Lexa, D.; Momenteau, M.; Saveant, J. M. *J. Am. Chem. Soc.* **1991**, *113*, 8455-8466.

(18) Bhugun, I.; Lexa, D.; Saveant, J.-M. *J. Am. Chem. Soc.* **1994**, *116*, 5015-5016.

(19) Bhugun, I.; Lexa, D.; Savéant, J.-M. *J. Am. Chem. Soc.* **1996**, *118*, 1769-1776.

(20) Behar, D.; Dhanasekaran, T.; Neta, P.; Hosten, C.; Ejeh, D.; Hambright, P.; Fujita, E. *The Journal of Physical Chemistry A* **1998**, *102*, 2870-2877.

(21) Kiyosawa, K.; Shiraishi, N.; Shimada, T.; Masui, D.; Tachibana, H.; Takagi, S.; Ishitani, O.; Tryk, D. A.; Inoue, H. *J. Phys. Chem. C* **2009**, *113*, 11667-11673.

(22) Leung, K.; Nielsen, I. M.; Sai, N.; Medforth, C.; Shelnutt, J. A. *The Journal of Physical Chemistry A* **2010**, *114*, 10174-10184.

(23) Grodkowski, J.; Neta, P.; Fujita, E.; Mahammed, A.; Simkhovich, L.; Gross, Z. *The Journal of Physical Chemistry A* **2002**, *106*, 4772-4778.

(24) Tripkovic, V.; Vanin, M.; Karamad, M.; Björketun, M. r. E.; Jacobsen, K. W.; Thygesen, K. S.; Rossmeisl, J. *J. Phys. Chem. C* **2013**, *117*, 9187-9195.

(25) Lin, S.; Diercks, C. S.; Zhang, Y.-B.; Kornienko, N.; Nichols, E. M.; Zhao, Y.; Paris, A. R.; Kim, D.; Yang, P.; Yaghi, O. M. *Science* **2015**, *349*, 1208-1213.

(26) Froehlich, J. D.; Kubiak, C. P. *Inorg. Chem.* **2012**, *51*, 3932-3934.

(27) Beley, M.; Collin, J.-P.; Ruppert, R.; Sauvage, J.-P. *Journal of the Chemical Society, Chemical Communications* **1984**, 1315-1316.

(28) Hawecker, J.; Lehn, J.-M.; Ziessel, R. *Journal of the Chemical Society, Chemical Communications* **1984**, 328-330.

(29) Slater, S.; Wagenknecht, J. H. *J. Am. Chem. Soc.* **1984**, *106*, 5367-5368.

(30) Rakowski Dubois, M.; Dubois, D. L. *Acc. Chem. Res.* **2009**, *42*, 1974-1982.

(31) Hawecker, J.; Lehn, J.-M.; Ziessel, R. *Journal of the Chemical Society, Chemical Communications* **1983**, 536-538.

(32) Kaim, W.; Kohlmann, S. *Inorg. Chem.* **1990**, *29*, 2909-2914.

(33) Smieja, J. M.; Kubiak, C. P. *Inorg. Chem.* **2010**, *49*, 9283-9289.

(34) Portenkirchner, E.; Oppelt, K.; Ulbricht, C.; Egbe, D. A.; Neugebauer, H.; Knör, G.; Sariciftci, N. S. *Journal of Organometallic Chemistry* **2012**, *716*, 19-25.

(35) Benson, E. E.; Grice, K. A.; Smieja, J. M.; Kubiak, C. P. *Polyhedron* **2013**, *58*, 229-234.

(36) Schneider, J.; Jia, H.; Muckerman, J. T.; Fujita, E. *Chem. Soc. Rev.* **2012**, *41*, 2036-2051.

(37) Bourrez, M.; Molton, F.; Chardon-Noblat, S.; Deronzier, A. *Angew. Chem.* **2011**, *123*, 10077-10080.

(38) Smieja, J. M.; Sampson, M. D.; Grice, K. A.; Benson, E. E.; Froehlich, J. D.; Kubiak, C. P. *Inorg. Chem.* **2013**, *52*, 2484-2491.

(39) Agarwal, J.; Shaw, T. W.; Schaefer III, H. F.; Bocarsly, A. B. *Inorg. Chem.* **2015**, *54*, 5285-5294.

(40) Vollmer, M. V.; Machan, C. W.; Clark, M. L.; Antholine, W. E.; Agarwal, J.; Schaefer III, H. F.; Kubiak, C. P.; Walensky, J. R. *Organometallics* **2014**, *34*, 3-12.

(41) Spivey, J. J. *Industrial & Engineering Chemistry Research* **1987**, *26*, 2165-2180.

(42) Muzart, J. *Chem. Rev.* **1992**, *92*, 113-140.

(43) Hassan, J.; Sevignon, M.; Gozzi, C.; Schulz, E.; Lemaire, M. *Chem. Rev.* **2002**, *102*, 1359-1470.

(44) Johansson Seechurn, C. C.; Kitching, M. O.; Colacot, T. J.; Snieckus, V. *Angew. Chem., Int. Ed.* **2012**, *51*, 5062-5085.

(45) Sheldon, R.; Downing, R. *Appl. Catal., A: Gen.* **1999**, *189*, 163-183.

(46) Mizuno, N.; Misono, M. *Chem. Rev.* **1998**, *98*, 199-218.

(47) Shiju, N. R.; Guliants, V. V. *Appl. Catal., A: Gen.* **2009**, *356*, 1-17.

(48) Kresge, C.; Leonowicz, M.; Roth, W.; Vartuli, J.; Beck, J. *nature* **1992**, *359*, 710-712.

(49) Rao, Y.; Antonelli, D. M. *Journal of Materials Chemistry* **2009**, *19*, 1937-1944.

(50) Suib, S. L. *Acc. Chem. Res.* **2008**, *41*, 479-487.

(51) Brock, S. L.; Duan, N.; Tian, Z. R.; Giraldo, O.; Zhou, H.; Suib, S. L. *Chem. Mat.* **1998**, *10*, 2619-2628.

(52) Cao, H.; Suib, S. L. *J. Am. Chem. Soc.* **1994**, *116*, 5334-5342.

(53) Ghosh, R.; Shen, X.; Villegas, J. C.; Ding, Y.; Malinger, K.; Suib, S. L. *J. Phys. Chem. B* **2006**, *110*, 7592-7599.

(54) Genuino, H. C.; Dharmarathna, S.; Njagi, E. C.; Mei, M. C.; Suib, S. L. *J. Phys. Chem. C* **2012**, *116*, 12066-12078.
(55) Sithambaram, S.; Ding, Y.; Li, W.; Shen, X.; Gaenzler, F.; Suib, S. L. *Green Chem.* **2008**, *10*, 1029-1032.
(56) Wasalathanthri, N. D.; Poyraz, A. S.; Biswas, S.; Meng, Y.; Kuo, C.-H.; Kriz, D. A.; Suib, S. L. *J. Phys. Chem. C* **2015**, *119*, 1473-1482.
(57) Makwana, V. D.; Son, Y.-C.; Howell, A. R.; Suib, S. L. *J. Catal.* **2002**, *210*, 46-52.
(58) Poyraz, A. S.; Kuo, C.-H.; Biswas, S.; King'ondu, C. K.; Suib, S. L. *Nat. Commun.* **2013**, *4*.
(59) Monnier, F.; Taillefer, M. *Angew. Chem., Int. Ed.* **2009**, *48*, 6954-6971.
(60) Zhang, J.; Zhang, Z.; Wang, Y.; Zheng, X.; Wang, Z. *Eur. J. Org. Chem.* **2008**, *2008*, 5112-5116.
(61) Benyahya, S.; Monnier, F.; Taillefer, M.; Man, M. W. C.; Bied, C.; Ouazzani, F. *Adv. Synth. Catal.* **2008**, *350*, 2205-2208.
(62) Deiters, A.; Martin, S. F. *Chem. Rev.* **2004**, *104*, 2199-2238.
(63) Evans, D. L.; Minster, D. K.; Jordis, U.; Hecht, S. M.; Mazzu Jr, A. L.; Meyers, A. *J. Org. Chem.* **1979**, *44*, 497-501.
(64) Wendlandt, A. E.; Stahl, S. S. *J. Am. Chem. Soc.* **2014**, *136*, 11910-11913.
(65) Chakraborty, S.; Brennessel, W. W.; Jones, W. D. *J. Am. Chem. Soc.* **2014**, *136*, 8564-8567.
(66) Yamaguchi, R.; Ikeda, C.; Takahashi, Y.; Fujita, K.-i. *J. Am. Chem. Soc.* **2009**, *131*, 8410-8412.
(67) Wendlandt, A. E.; Stahl, S. S. *J. Am. Chem. Soc.* **2013**, *136*, 506-512.
(68) Iosub, A. V.; Stahl, S. S. *Org. Lett.* **2015**, *17*, 4404-4407.
(69) Cui, X.; Li, Y.; Bachmann, S.; Scalone, M.; Surkus, A.-E.; Junge, K.; Topf, C.; Beller, M. *J. Am. Chem. Soc.* **2015**, *137*, 10652-10658.

CHAPTER 2. Ligand dependent activity enhancement in CO_2 electro reduction by Re(α-diimine) complexes: effect of π conjugation and thiazole/pyridine coordination

2.1 Abstract

We report synthesis and characterization of six rhenium complexes to catalyze homogeneous electrochemical reduction of CO_2: $Re(N\text{-}N)(CO)_3Cl$ (N-N= 2,2′-pyridylquinoline (pyq) (**1**), 2-(2-pyridyl)-1,8-naphthyridine (pynp) (**2**), and 2-(2-pyridyl)-benzo[1,8]naphthyridine (pybnp) (**3**), 2-(quinoline-2-yl)thiazole (thq) (**4**), 2-(1,8-naphthyridine-2-yl)thiazole (thnp) (**5**), 2-(benzo-1,8-naphthyridine-2-yl)thiazole (thbnp) (**6**)). All six complexes have been characterized extensively by NMR, CHN analysis, UV-Vis and IR spectroscopy. Electrocatalytic ability of these against carbon dioxide reduction is studied by cyclic voltammetry. Comparison of relative TOF values [which is proportional to $(i_{cat}/i_p)^2$] and rate constants for CO_2 reduction obtained from cyclic voltammetry experiment reveals polypyridyl Re compounds with pyridine or thiazole co-ordination (compounds **3** and **6**) to be most efficient. Reactivity with CO_2 was also inquired by rate constant measurement and Density Functional Theory (DFT) calculations.

2.2 Background and Significance

A major concern in todays scientific and political platform is climate change a.k.a. global warming. Continuous rise in anthropogenic carbon dioxide emission starting from early twentieth century resulted in much higher concentration of CO_2, the potent green house gas.[1,2] Research aiming at limiting atmospheric CO_2 is vastly

spread. Some of the important reactions include the reduction of CO_2 to CO or other useful organic compounds.[3-8] Transition metal mediated electrocatalytic CO_2 reduction has gained eminent success during last three decades starting from 1983 when Lehn, Ziessel and Hawecker published a paper describing *fac*-Re(bpy)$(CO)_3$Cl (bpy= 2,2'-bipyridine) catalyzed reduction of CO_2 to CO.[9,10] Rhenium complexes coordinated to α-diimine ligands have emerged as excellent catalysts for selective reduction of carbon dioxide over proton under both photochemical and electrochemical conditions.[4,11,12] It has been shown by Kubiak and his colleagues that substitution (R) on bipyridine ligand affects the reactivity in *fac*-Re(bpy-R)$(CO)_3$Cl compounds[13] (R= H, Me, COOH, t-butyl, OMe); *tert*-butyl group increased the activity 10 times while –OMe did not show catalysis (figure 2.1).

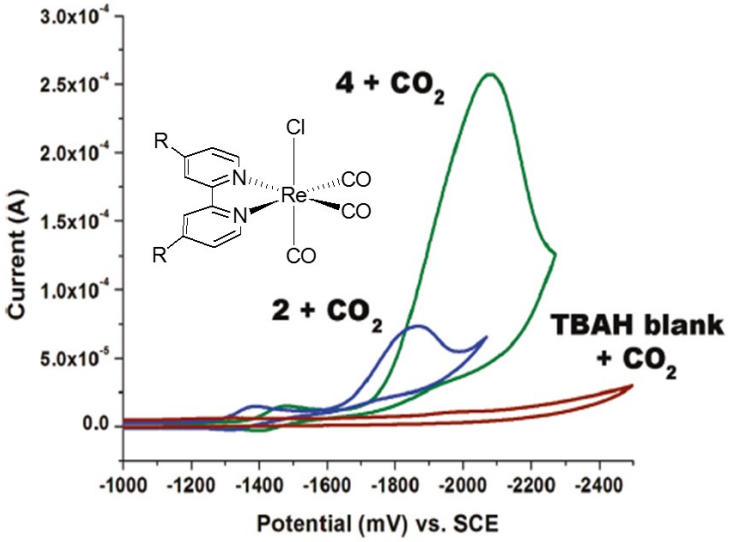

Figure 2.1 Catalytic comparison of *fac*-Re(bpy-R)$(CO)_3$Cl, R= H (complex 2, blue curve), R= t-butyl (complex 4, green curve) in CO_2 saturated acetonitrile solution of 0.5mM catalyst and TBAH electrolyte at $0.1Vs^{-1}$ scan rate. The red curve displays no catalysis in blank reaction which contains solvent and electrolyte only.

Based on the mechanistic studies, a catalytic cycle has been proposed that starts with formation of a doubly reduced $Re^0(bpy\text{-}R)^{-1}$ species (A in scheme 1 below) from *fac*-$Re(bpy\text{-}R)(CO)_3Cl$. Upon reaction with CO_2 formation of a carboxylate species that forms carboxylic acid (C) through protonation. The carboxylic acid species then reacts with a second proton to liberate water and generates the tetracaronyl cataionic intermediate (D) (scheme 1).[14]

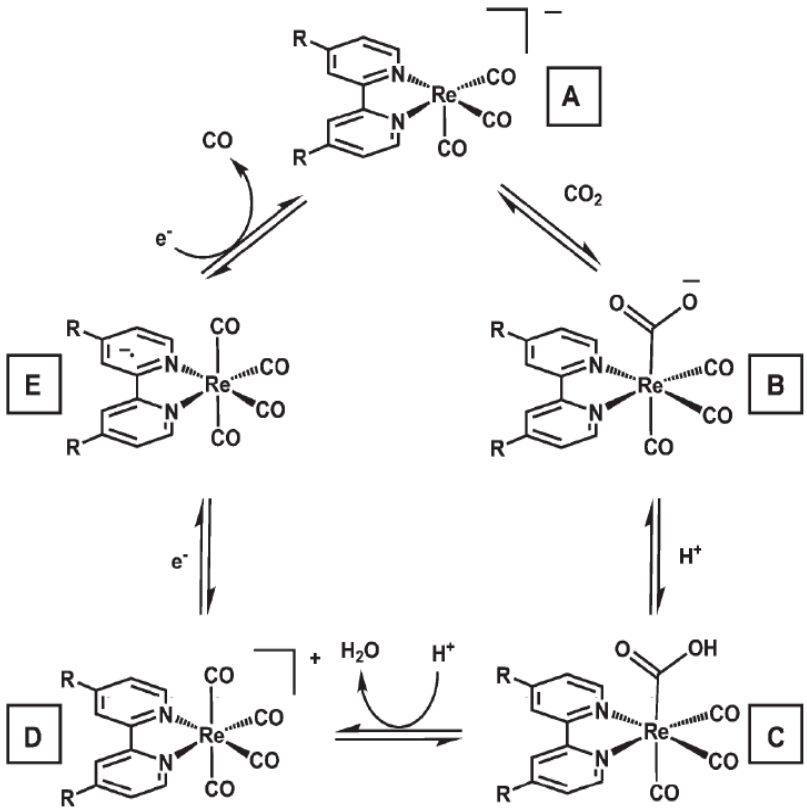

Scheme 2.1 Proposed catalytic cycle by $Re(bpy\text{-}R)(CO)_3Cl$ compounds

In our research group, we are interested in studying variations in the nature of *N*,*N*-diimine ligand coordinated to Re, that could potentially allow storage of multiple reducing equivalents and thus influence CO_2 catalysis. We have designed a new family of $Re(L\text{-}L)(CO)_3Cl$ compounds where L-L are pyridine or thiazole substituted quinoline, naphthyridine and benzonaphthyridine ligand (figure 2.2). Electrochemical studies on these complexes revealed that reduction potential decreases from quinoline

to naphthyridine to benzonaphthyridine moieties due to lowering energy in lowest unoccupied molecular orbital (LUMO) of the compound. A direct effect was observed in catalytic activity; compounds having a benzonaphthyridine ligand showed 12-130 times enhancement in relative TOF (which is proportional to $(i_{cat}/i_p)^2$). Also, compounds Re(pybnp)(CO_3)Cl **(3)** and Re(thbnp)(CO_3)Cl **(6)** exhibited highest rate constants for CO_2 catalysis, 4.2×10^3 and $1.8\times10^3 M^{-1}s^{-1}$, respectively, much higher than the classic Lehn's catalyst and its *tert*-butyl analog. In order to determine structure-activity relationships, theoretical calculations were performed. A gradual decrease in Re-Cl bond dissociation energy in complexes **1-3** and **4-6** was calculated from full-atom model structures that may account for the rise in relative turn over.

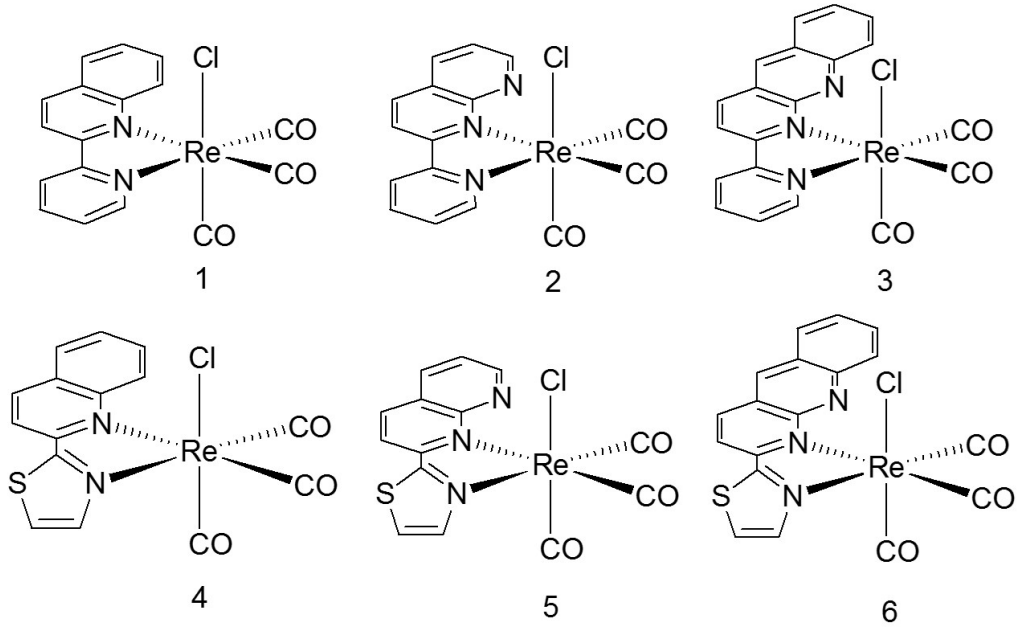

Figure 2.2 Six Re(N-N)(CO_3)Cl complexes studied- Re(pyq)(CO_3)Cl **(1),** Re(pynp)(CO_3)Cl **(2),** Re(pybnp)(CO_3)Cl **(3),** Re(thq)(CO_3)Cl **(4),** Re(thnp)(CO_3)Cl **(4),** Re(thbnp)(CO_3)Cl **(6)**.

2.3 Experimental details

2.3.1 Synthesis of ligands and complexes

Ligands 2-(pyridine-2-yl)quinoline (pyq), 2-(pyridine-2-yl)-1,8-naphthyridine (pynp) and 2-(pyridine-2-yl)benzo-1,8-naphthyridine (pybnp), 2-(quinoline-2-yl)thiazole (thq), 2-(1,8-naphthyridine-2-yl)thiazole (thnp), 2-(benzo-1,8-naphthyridine-2-yl)thiazole (thbnp) were prepared according to previously reported methods.[15,16]

Re(pyq)(CO)$_3$Cl (1). A mixture of $Re(CO)_5Cl$ (0.264 g, 0.0007 mol), pyq (0.150 g, 0.0007 mol) and toluene (10mL) was refluxed for 2 hours. The product, a yellow solid, was collected by filtration, washed with toluene and finally dried under reduced pressure (0.3 g, yield = 81%). ^{1}H NMR (δ, 400 MHz, DMSO-*d*$_6$): 9.20(dd,1H), 8.95(t,2H), 8.84(d,1H), 8.75(d,1H), 8.41(td,1H), 8.25(m,1H), 8.12(m,1H), 7.89(m,1H), 7.83(m,1H). ^{13}C NMR (δ, 101 MHz, Chloroform-*d*): 119.64, 124.61, 125.43, 127.42, 128.20, 128.70, 132.25, 136.65, 139.76, 140.90, 145.93, 152.44, 155.85, 157.77, 189.16, 196.45, 197.57. Anal. Found for $C_{17}H_{10}N_2O_3ClRe•0.5C_7H_8$: C, 44.08; H, 2.40; N, 5.01. Calcd C, 44.13; H, 2.53; N, 5.02.

Re(pynp)(CO)$_3$Cl (2). A mixture of $Re(CO)_5Cl$ (0.124g, 0.0003 mol), pynp (0.071 g, 0.0003 mol) and toluene (10mL) was refluxed for 2 hours. The product, an orange solid, was collected by filtration, washed with toluene and finally dried under reduced pressure (0.15 g, yield = 86%). Recrystallization from DMSO resulted in single crystals suitable for X-ray measurements. ^{1}H NMR (δ, 400 MHz,DMSO-*d*$_6$): 9.32(dd,1H), 9.21(m,1H), 9.03(t,2H), 8.95(d,1H), 8.75(dd,1H), 8.42(d,1H), 7,95(dd,1H), 7.86(m,1H). ^{13}C NMR (δ, 101 MHz, Chloroform-*d*): 120.94, 123.51, 124.92, 126.35, 128.49, 138.17, 139.86, 142.12, 152.62, 153.40, 155.05, 155.92, 159.24, 171.27, 189.91, 198.03, 198.66. Anal. Found for $C_{16}H_9N_3O_3ClRe$: C, 37.42; H, 2.02; N, 8.41. Calcd C, 37.25; H, 2.34; N, 8.14.

Re(pybnp)(CO)$_3$Cl (3). A mixture of Re(CO)$_5$Cl (0.140g, 0.0004 mol), pybnp (0.1 g, 0.0004 mol) and toluene (10mL) was refluxed for 2 hours. A red-brown solid was collected by filtration, washed with toluene and finally dried under reduced pressure (0.15g, yield = 66 %). ^{1}H NMR (δ, 400 MHz, DMSO-*d*$_6$): 9.49(s,1H), 9.28(dd,1H), 9.16(d,1H), 9.09(d,1H), 8.88(d,1H), 8.45(m,2H), 8.37(m,1H), 8.13(m,1H), 7.92(m,1H), 7.83(m,1H). ^{13}C NMR (δ, 101 MHz, Chloroform-*d*): 119.41, 120.82, 127.17, 127.42, 127.96, 128.65, 128.94, 133.59, 139.89, 142.57, 150.61, 153.60, 156.06, 161.60. Anal. Found for $C_{20}H_{11}N_3O_3ClRe$: C, 42.65; H, 2.14; N, 7.48. Calcd C, 42.44; H, 2.49; N, 7.42.

Re(thq)(CO)$_3$Cl (4). A mixture of Re(CO)$_5$Cl (0.264 g, 0.0007 mol), thq (0.155 g, 0.0007 mol) and toluene (10mL) was refluxed for 2 hours. The product, orange-yellow solid, was collected by filtration, washed with toluene and finally dried under reduced pressure (0.32 g, yield = 88%). ^{1}H NMR (400 MHz, DMSO-*d*6) δ 8.95 (d, *J* = 8.5 Hz, 1H), 8.67 (d, *J* = 8.7 Hz, 1H), 8.57 (d, *J* = 8.5 Hz, 1H), 8.45 (d, *J* = 3.3 Hz, 1H), 8.35 (d, *J* = 3.3 Hz, 1H), 8.28 (d, *J* = 1.2 Hz, 1H), 8.16 (ddd, *J* = 8.7, 6.9, 1.5 Hz, 1H), 7.96 – 7.86 (m, 1H). ^{13}C NMR (δ, 101 MHz, Chloroform-*d*): 121.46, 128.28, 129.27, 129.73, 130.05, 133.84, 142.45, 145.65, 146.67, 153.28, 170.78, 189.05, 198.60. Anal. Found for $C_{15}H_8N_2O_3ClReS$: C, 34.58; H, 2.13; N, 5.38. Calcd C, 34.49; H, 2.19; N, 5.35.

Re(thnp)(CO)$_3$Cl (5). A mixture of Re(CO)$_5$Cl (0.264 g, 0.0007 mol), thnp (0.150 g, 0.0007 mol) and toluene (10mL) was refluxed for 2 hours. The product, a maroon solid, was collected by filtration, washed with toluene and finally dried under reduced pressure (0.28 g, yield = 77%). ^{1}H NMR (δ, 400 MHz, DMSO-*d*$_6$): 9.33 (dd, *J* = 4.2, 1.9 Hz, 1H), 9.02 (d, *J* = 8.5 Hz, 1H), 8.77 (dd, *J* = 8.2, 1.9 Hz, 1H), 8.68 (d, *J* = 8.4

Hz, 1H), 8.45 (d, *J* = 3.3 Hz, 1H), 8.39 (d, *J* = 3.3 Hz, 1H), 7.96 (dd, *J* = 8.1, 4.2 Hz, 1H). ^{13}C NMR (δ, 101 MHz, Chloroform-*d*): 121.48, 123.48, 124.85, 128.38, 138.29, 142.62, 145.55, 152.36, 153.87, 155.56, 169.02, 188.57, 197.49, 197.86. Anal. Found for $C_{14}H_7N_3O_3ClReS$: C, 32.22; H, 1.93; N, 8.05. Calcd C, 32.13; H, 1.93; N, 8.02.

Re(thbnp)(CO)$_3$Cl (6). A mixture of $Re(CO)_5Cl$ (0.142 g, 0.0004 mol), thbnp (0.103 g, 0.0004 mol) and toluene (10mL) was refluxed for 2 hours. The product, a brown-black solid, was collected by filtration, washed with toluene and finally dried under reduced pressure (0.15 g, yield = 68%). ^{1}H NMR (δ, 400 MHz, DMSO-*d*$_6$): 9.20(dd,1H), 8.95(t,2H), 8.84(d,1H), 8.75(d,1H), 8.41(td,1H), 8.25(m,1H), 8.12(m,1H), 7.89(m,1H), 7.83(m,1H). ^{13}C NMR (δ, 101 MHz, Chloroform-*d*): 120.26, 121.12, 127.70, 128.05, 128.34, 129.02, 129.58, 134.09, 140.53, 143.47, 146.27, 151.17, 156.37. Anal. Found for $C_{18}H_9N_3O_3ClReS$: C, 37.79; H, 2.11; N, 7.35. Calcd C, 37.72; H, 2.09; N, 7.30.

2.3.2 Methods used for characterization

^{1}H and ^{13}C NMR spectra were recorded on a Bruker AVANCE (300 MHz) or Bruker AVANCE III (400 MHz) system at ambient temperature and were referenced to residual solvent peaks. UV-Vis spectra were recorded on a Cary 50 spectrophotometer. Solution IR spectra (CH_3CN) were carried on a Jasco FT/IR-6100 spectrometer. Elemental analyses were performed at Atlantic Microlab, Inc., in Norcross, GA. Electrochemical experiments were performed by using a Model 6012D Electrochemical analyzer from CH Instruments, Inc. or DY2311 Potentiostat from Digi-Ivy. Cyclic voltammetry experiments were performed under $N_{2(g)}$ or $CO_{2(g)}$ in a one-compartment cell with a glassy carbon working electrode (3mm diameter), a platinum wire counter electrode and a Ag/Ag^+ pseudo-reference electrode separated

from the main compartment by a Vycor tip. Ferrocene was used as an external reference and the potentials vs Fc/Fc^+ were converted to SCE ($E_{1/2}$ (Fc/Fc^+) = 0.380V vs. SCE).[17] All experiments were performed by using 0.1 M tetrabutylammonium hexafluorophosphate ($TBAPF_6$) as the supporting electrolyte, acetonitrile as the solvent, and with rhenium complexes concentration of 0.5 mM. EPR spectra in the X band were recorded with a Bruker System EMX. A two-electrode capillary served to generate intermediates for the EPR studies.

X-ray Crystallography. X-ray diffraction data were collected on a Bruker APEX DUO CCD platform diffractometer (Mo Kα (λ = 0.71073 Å)) at 125 K. Suitable crystals were mounted in a nylon loop with Paratone-N cryoprotectant oil. The structures were solved using direct methods and standard difference map techniques, and were refined by full-matrix least-squares procedures on F^2 with SHELXTL (Version 2008).[18] All non-hydrogen atoms were refined anisotropically. Hydrogen atoms on carbon were included in calculated positions and were refined using a riding model.

Computational Methods. Geometry optimization and frequency calculations of all complexes were performed (by Dino Villagrán, University of Texas at El Paso, El Paso) on a full–atom scale using Density Functional Theory (DFT)[19] with the Becke-3 parameter exchange functional[20,21] and the Lee-Yang-Parr nonlocal correlational functional[22] (B3LYP) implemented in the Gaussian 09 (Revision C.01) program suit.[23] For complexes **1–6**, the 6-31G(d,p)[24] basis set was used for non-metal atoms (C, H, N, and S). The double-zeta LANL2DZ basis set modified by Couty and Hall[25] and its correspondent effective core potential (ECP)[26] was used for Re atoms. The same combination of basis sets for metals and non-metal atoms were used to calculate a doubly reduced species as a template to model the CO_2 reduction process. As

reported, by Carter et al[12] the addition of a potassium atom in the CO_2 fragment is necessary for the convergence of the geometry optimizations. The LANL2DZ ECP and its associated basis set were used for K atoms. The self-consistent field convergence criterion used was 10^{-8} on all calculations. Bond dissociation energies (BDE) for the heterolytic Re–X (X = Cl, CO_2K) bond cleavage were calculated using the enthalpies of the different species at 298 K. Geometry optimized structures were confirmed to be local minima in the potential energy surface by performing frequency calculations and confirming the absence of imaginary vibrations. All calculations were performed in a 44-procesor PowerWolf PSSC supercomputer running Linux Red Hat 4.1.2-54 located at the University of Texas at El Paso.

2.3.3 Structural Characterization

The syntheses of complexes **1**-**6** were carried out by treating $Re(CO)_5Cl$ with the corresponding ligand in refluxing toluene under N_2 for 2-2.5 hours (Figure 1). The crude products were collected by filtration and purified by recrystallization to provide the metal complexes in good yields (60-80%). Complexes **1**-**6** were characterized by ^1H and ^{13}C NMR, mass spectrometry, and elemental analysis.

2.3.3.1 Single Crystal X-Ray

The molecular structure of **2** was determined by X-ray crystallography and the thermal ellipsoid plot is shown in Figure 2.3. The structure can be considered as distorted octahedral with three CO groups coordinated in a facial arrangement. The Re-$N_{diimine}$ distances range from 2.170(2) to 2.203(2) Å and the bite angle for the pyridine-naphthyridine rhenium complex **2** is 74.22(6)°. These resemble those of other rhenium-diimine complexes with similar chelating ligands.[27,28] In compound **2**, C-O bond length of the carbonyl *trans* to the diimine ligands are close in magnitude to

each other and vary in the range 1.146(3)- 1.157(3) Å. The small differences in bonding distances are likely due to effects arising from crystal packing, since the ν_{CO} values for these compounds do not differ significantly from each other (see below). In addition, C-Re-C angles for complex **2** range from 88.1° to 90.8° and are similar to the reported structure for $Re(bpy)(CO)_3Cl$ (**I**).[9] The structure of **2** optimized at the DFT level is in very good agreement with experimental data (Figure 2.11 B).

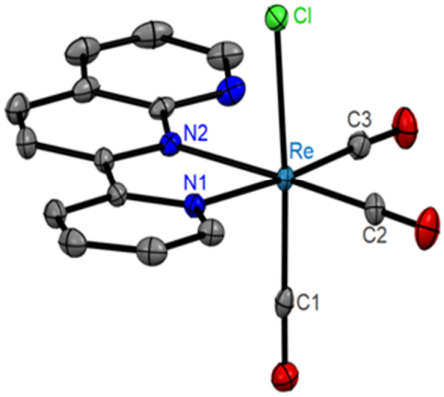

	X-ray	B3LYP
Re-N1	2.170(2)	2.193
Re-N2	2.203(2)	2.237
Re-Cl	2.487(5)	2.512
Re-C1	1.914(2)	1.922
Re-C2	1.911(2)	1.919
Re-C3	1.937(2)	1.944
N1-Re-N2	74.22	73.89

Figure 2.3 Left: Thermal ellipsoid plot of **2** at 50% probability. Hydrogen atoms are omitted for clarity. **Right:** Selected geometrical features for **2** obtained via X-ray crystallography and DFT calculations with bond lengths in units of angstrom (Å) and bite angle in units of degrees.

2.3.3.2 Carbonyl Vibrational Spectra

Three CO stretching bands are observed in the infrared spectra of the rhenium complexes **1-6** in *fac* configuration. Force constants (Table 2.1) were calculated according to the Cotton-Kraihanzel method.[29] The interaction constants, k_i, for **1-6** are very similar to those calculated for **I** (k_1 = 15.07, k_2 = 15.44, and k_i = 0.60), indicating similar weak σ bonding between the α-diimine ligands and the tricarbonylrhenium fragments,[30] in agreement with the similar Re-$N_{diimine}$ distances observed by X-ray.

Table2.1 CO Vibrational Stretching Frequencies ν_{CO} (cm^{-1}) in Acetonitrile and calculated Force Constants k (mdyn/Å) of Rhenium (I) complexes.[a]

Complex	ν_{CO}			k_1	k_2	k_i
	A′(1)	A′(2)	A"			
1	2023	1917	1900	15.60	15.17	0.59
2	2021	1919	1890	15.81	14.99	0.57
3	2021	1922	1882	15.42	15.51	0.59
4	2015	1925	1892	14.91	15.99	0.55
5	2019	1932	1880	15.64	15.22	0.49
6	2021	1928	1889	15.79	15.34	0.55

[a]Cotton-Kraihanzel method.

2.3.3.3 Absorption Spectra

The electronic absorption spectrum of complexes **1**-**6** in acetonitrile exhibit metal-to-ligand charge transfer (MLCT) transitions at 395-465 nm (Figure 2.4 (a-f), Table 2.2) for the lowest energy observed transition.[31] This assignment is supported by the significant bathochromic shift when going from polar to less polar solvents ($\Delta\nu_{max}$, Table 2.2). The extent of MLCT solvatochromism can be correlated with the metal/ligand orbital interaction. An increase of mixing of metal and ligand molecular orbitals results in a decrease of the solvatochromic effect due to the diminished polarity difference between ground and excited states.[32] The bands observed at 242 nm and 350 nm in acetonitrile solutions of complexes **1** and **2** can be assigned to the overlap of the pyridine and quinolone/naphthyridine ππ* LC transitions. These LC transitions have also been observed in other pynp transition complexes.[33] Due to extended π system of the benzonaphthyridine moiety in **3** and **6**, the ππ* LC transitions are observed red-shifted (381 and 390 nm) as compared to remaining

complexes. Similar assignment of the LC bands have been reported for ruthenium and rhenium complexes of pybnp and the isomeric ligand 2-(2-pyridyl)benzo[b]-1,5-naphthyridine.[15,34]

Table 2.2 UV/Vis data and charge-transfer absorption maxima ν_{max} (cm^{-1}) of **1** – **6**.

Complex	λ_{max} (ε, $M^{-1}cm^{-1}$)	MLCT ν_{max} (cm^{-1})		$\Delta\nu_{max}$ (cm^{-1})
		Acetonitrile	Toluene	
1	242 (36500), 350 (18900), 394 (3800)	25400	23146	2254
2	242 (24800), 349 (24400), 425 (3600)	23419	20747	2672
3	291 (43600), 381 (30200), 455 (3300)	21882	19342	2540
4	287 (21200), 356 (19700), 403 (4200)	24691	22381	2310
5	270 (10600), 360 (19400), 437 (2900)	22883	20332	2551
6	235 (39200), 390 (31480), 465 (4320)	21505	18897	2608

Conditions: Acetonitrile solvent, 20µM solution, quartz cuvette of path length 1.0cm.

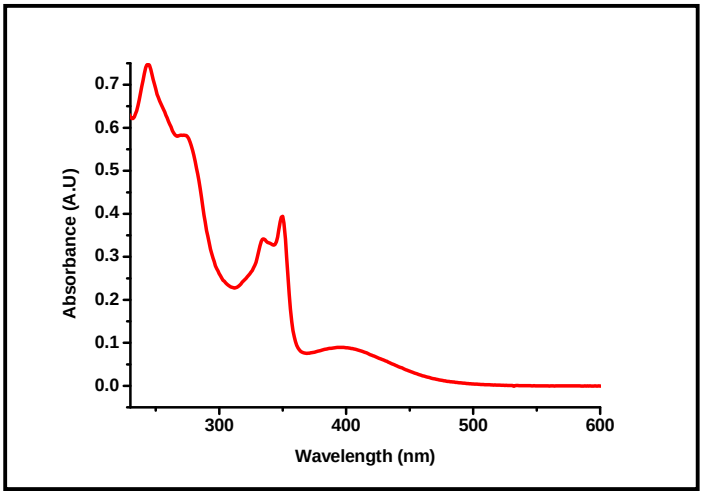

Figure 2.4 (a) UV-Vis spectra of compound 1

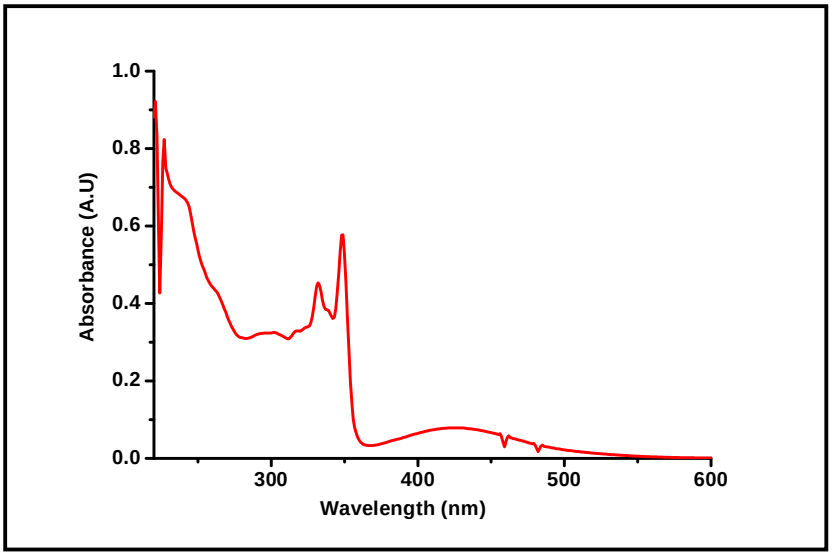

Figure 2.4 (b) UV-Vis spectra of compound 2

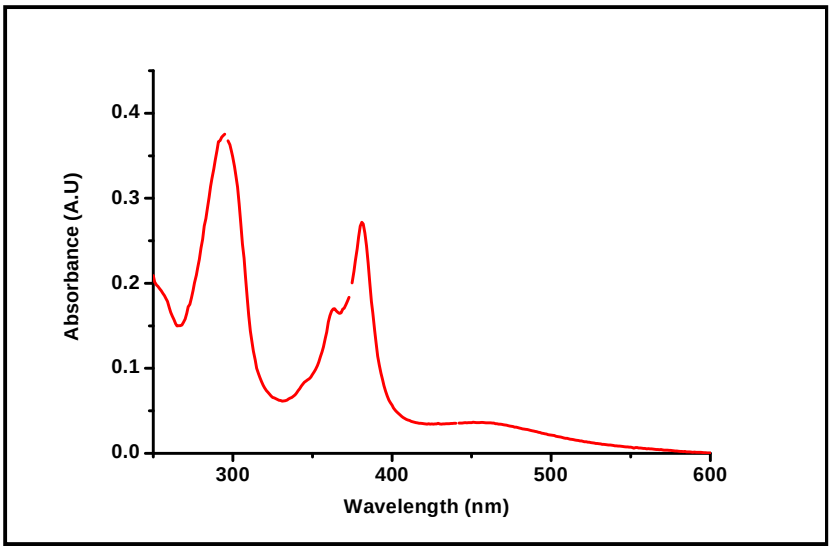

Figure 2.4 (c) UV-Vis spectra of compound 3

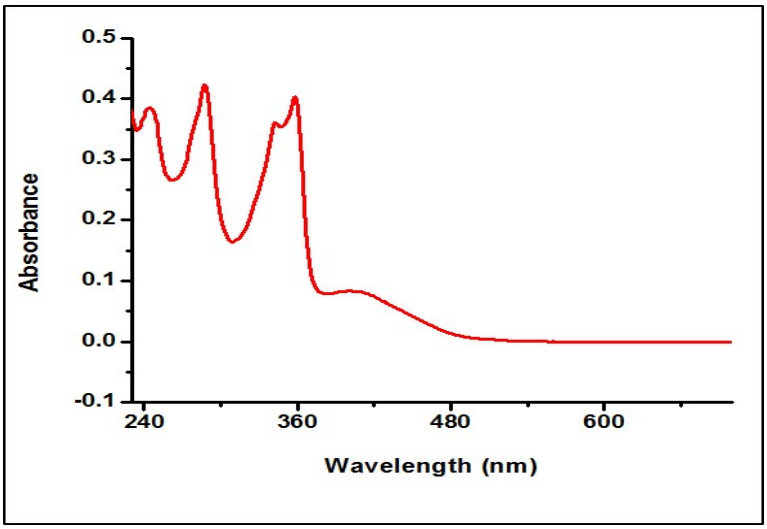

Figure 2.4 (d) UV-Vis spectra of compound 4

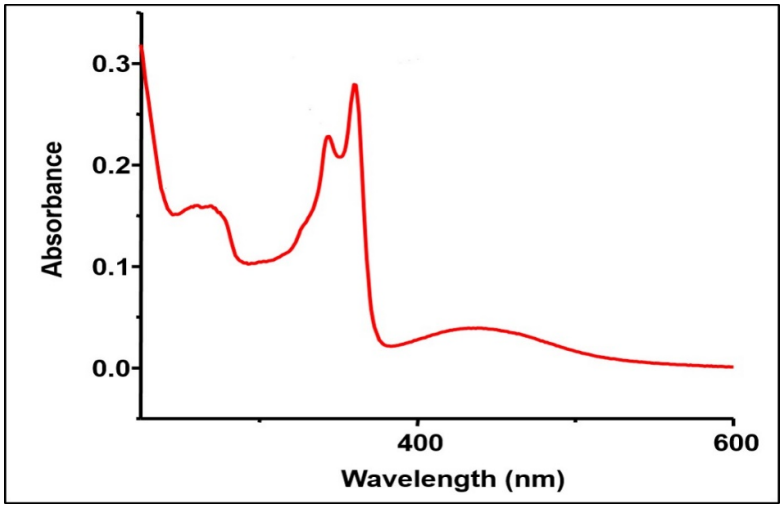

Figure 2.4 (e) UV-Vis spectra of compound 5

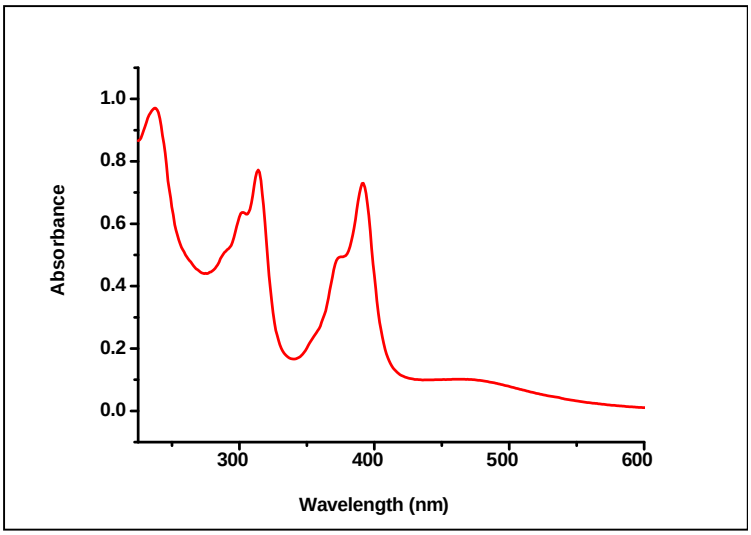

Figure 2.4 (f) UV-Vis spectra of compound 6

2.3.3.4 Electrochemical properties

All six complexes in our study behave similarly when reduced electrochemically at 0.1V/s scan rate under nitrogen atmosphere in presence of acetonitrile solvent, 0.1M $TBAPF_6$ supporting electrolyte, glassy carbon working electrode, Pt-wire counter electrode and Ag/Ag^+ pseudo-reference electrode. Cyclic voltammetry of compound **1** in dry acetonitrile under nitrogen atmosphere displays a first reversible one-electron reduction at a lower potential ($E_{1/2}$ = -1.1 V vs. SCE) than that observed for **I**, as expected for a ligand with a LUMO at lower energy due to the extended pi-conjugation (Figure 2.5(a-f), Table 2.3). The second cathodic signal is observed at -1.6 V vs. SCE and has a corresponding anodic counter peak at an anodically shifted potential (-1.3 V vs. SCE) likely due to an ECE process (E: electron transfer step; C: chemical step, e.g. chloride dissociation). The anodic peak at -1.0 V vs. SCE corresponds to the $[Re(diimine)(CO)_3(solvent)]^{0/+}$ couple formed after the

dissociation of chloride. Cyclic voltammetry of compounds 2 and 3 resemble that of compound 1, although all of the processes appear at more positive values. The complexes 4, 5 and 6 were reduced even at lower potential (Table 2.3). In summary, appearance of a first reversible cathodic peak ranging from -1.1V to -0.65V vs. SCE (Figure 2.6) followed by an irreversible peak in between -1.5V to -1.2V, both being at more positive potential than I, can be explained by extended π conjugation in quinoline/naphthyridine/benzonaphthyridine ligand moiety combined with either pyridine or thiazole ring. Similar to **I**, the first reduction wave is likely to represent pyridine-based reduction of the starting complex to form a radical complex $[Re^{I}(\alpha\text{-diimine}^{-})(CO)_3(Cl)]$.[9] Since the complexes undergo facile halide loss on reduction, an anodic peak appears in between -1.2V to -0.8V vs. SCE corresponding to the $[Re(\alpha\text{-diimine})(CO)_3(solvent)]^{0/+}$ couple. Kubiak mentioned that reduction potential gains more negative value with increasing pk_a of *para* substituents present on bpy ring of the complexes $Re(bpy\text{-}R)(CO)_3Cl$.[13] Acid dissociation constant, pk_a of pyridine is 5.2 while that of thiazole is found to be 2.5. We observe similar increament in negative reduction potential (both first and second cathode peaks) in our complexes- **3**>**6**, **2**>**5** and **1**>**4**, while complexes 3, 2, 1 have pyridine substituent and complexes 6, 5 and 4 have thiazole substituent (Table 2.3). Similar relation of reduction potentials can be established between complexes **1** and **2** and between **3** and **4**. To illustrate, complexes 1 and 3, bearing quinoline moiety (pk_a= 4.9) have more negative reduction potentials than complexes 2 and 4 with naphthyridine (pk_a= 3.4) ligands. Again, considering nature of the polypyridine ligands, π-acidity order, **benzonaphthyridine**> **naphthyridine**>**quinoline** (with respect to lowering of π*LUMO energy), tendency of electron accepatance or reduction potential reaches towards more negative values.

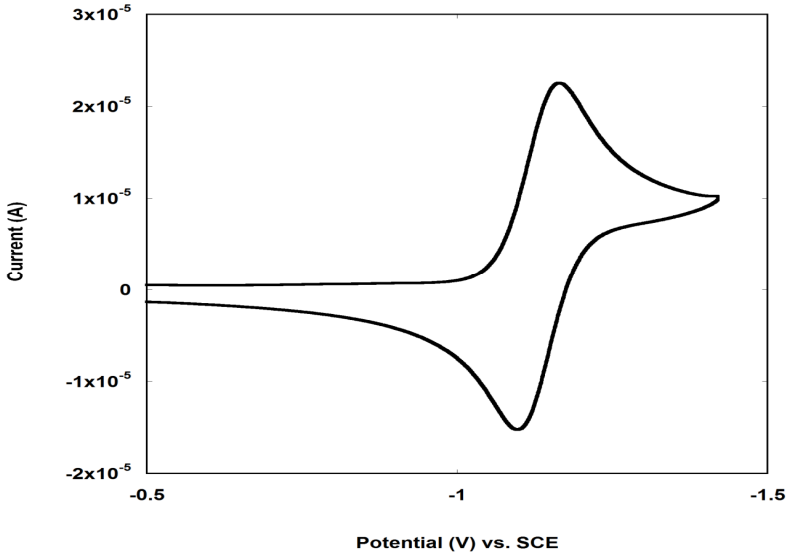

Figure 2.5 (a) cyclic voltammogram for compound 1

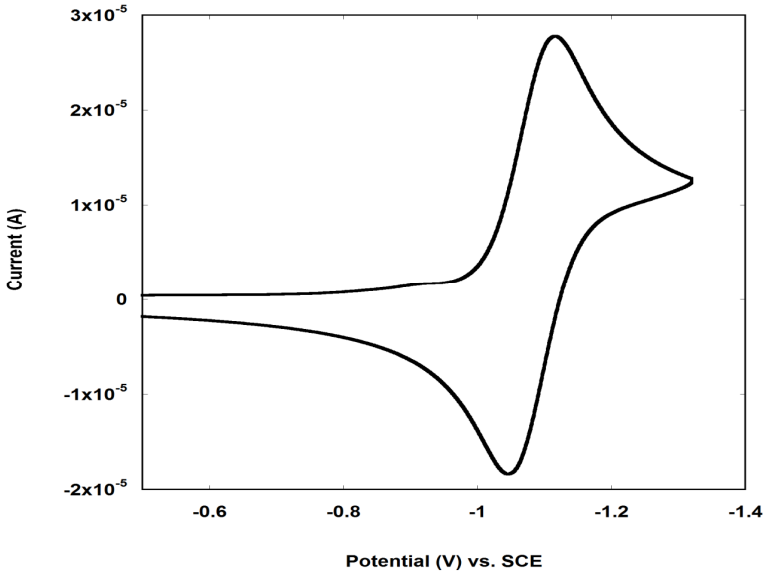

Figure 2.5 (b) cyclic voltammogram for compound 2

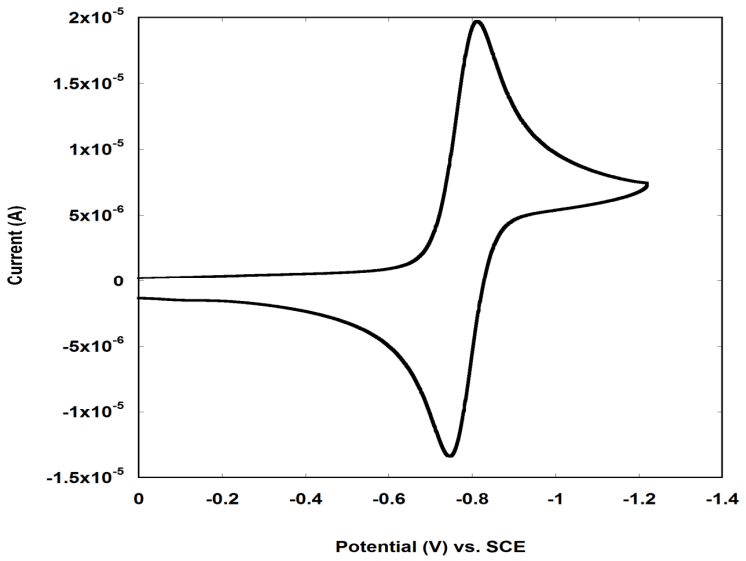

Figure 2.5 (c) cyclic voltammogram for compound 3

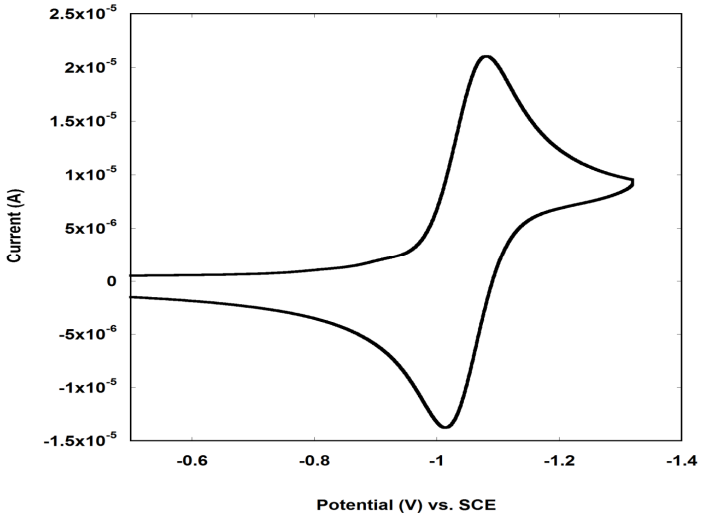

Figure 2.5 (d) cyclic voltammogram for compound 4

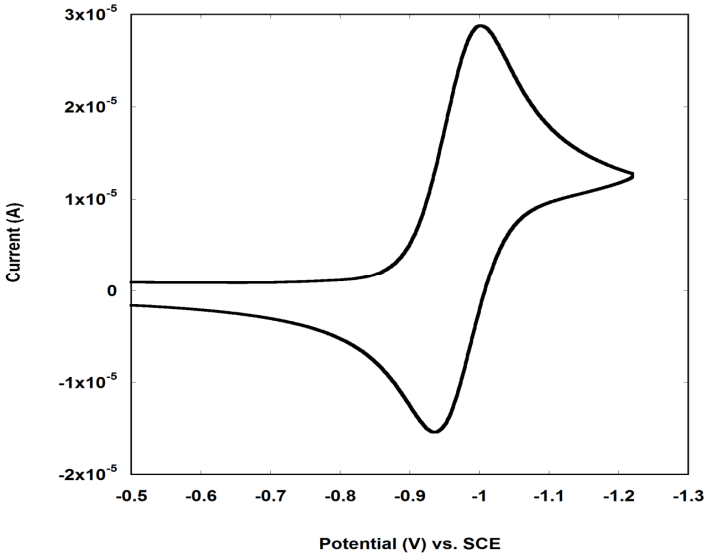

Figure 2.5 (e) cyclic voltammogram for compound 5

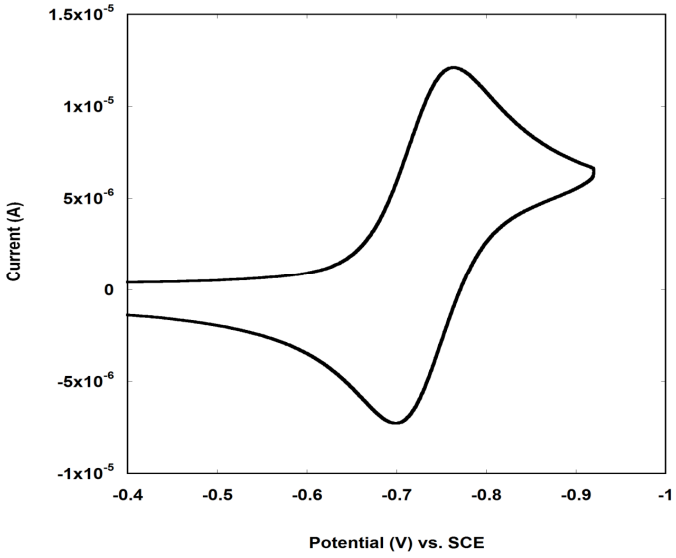

Figure 2.5 (f) cyclic voltammogram for compound 6

Table 2.3 Cathode peaks of six complexes under $N_{2(g)}$

Complex	First reduction potential V vs. SCE	Second reduction potential V vs. SCE
1	-1.13	-1.57
2	-1.08	-1.49
3	-0.78	-1.30
4	-1.13	-1.51
5	-0.97	-1.42
6	-0.77	-0.97
$Re(bpy)(CO)_3Cl$	-1.34	-1.73

[a] First reduction potential is the $E_{1/2}$ for the reversible wave, and the second reduction is the peak maximum for the cathode wave. All scans were performed at 0.1V/s in acetonitrile at 0.5mM rhenium complex with 0.1 M $[^nBu_4N]PF_6$ supporting electrolyte and a glassy carbon working electrode, Pt wire counter electrode, and Ag/Ag^+ reference (later adjusted to SCE).

2.4 Results and discussion

2.4.1 Electrocatalytic activity measurement

Acetonitrile solution of complex 1 upon saturation by 'bone dry' CO_2 for 10 minutes resulted in appearance of a new cathodic peak with an apparent catalytic current at c.a. -2.2 V vs. SCE. As seen in figure 5 the first cathodic peak is similar to that observed under N_2; however, the second reduction peak shifts in a positive direction without increase in height. The shift indicates a chemical process, most likely CO_2 binding to the reduced complex.

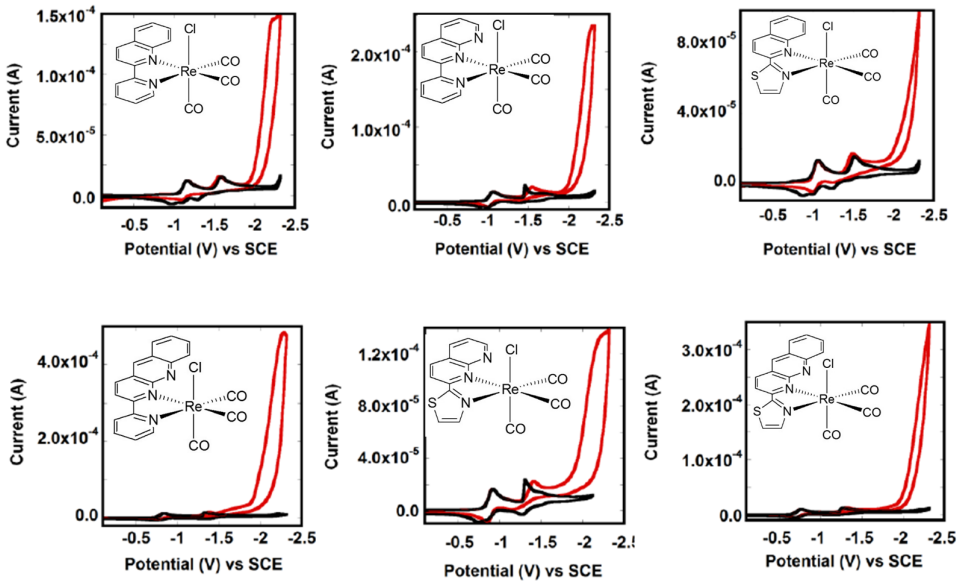

Figure 2.6 Representative cyclic voltammograms of compounds 1-6. Conditions: 3 mm diameter glassy carbon working electrode, Pt-wire counter electrode, Ag/Ag^+ reference (corrected to SCE), 0.5 mM solution in acetonitrile, 0.1 M $TBAPF_6$, r.t.

In order to compare the activities of these complexes with previously reported Re catalysts, we determined the overpotential and relative TOF (turnover frequency) values which are reported in Table 3. Here the parameter $(i_{cat}/i_p)^2$, obtained from cyclic voltammetry, is proportional to TOF, i_{cat} is catalytic current, i_p is peak current in absence of substrate. The overpotential, η, is calculated based on Appel and Helm's approach[35] and considering the difference between standard potential of CO_2/CO couple (-0.90V vs. SCE, Saveant's method[36]) and operating electrode potential, $E_{cat/2}$, the voltage at half of the catalytic current maximum in Acetonitrile. Rise in the TOF value (from 375 to 1674, Table 4) is observed from catalyst **1** to **3** along with increase in overpotential and current density (j). In comparison, complexes **4**, **5** and **6** which have thiazole-N coordination to metal center, exhibit lesser overpotential and smaller TOF values than analogous complexes having pyridine-N coordination. All six

catalysts are found to be more active than the classic Lehn's catalyst, $ReCl(bpy)(CO)_3$, regarding relative TOF but at the expense of overpotential as well as current density.

Table 2.4 Overpotentials (η), current densities (j), relative TOF $(i_{cat}/i_p)^2$ and peak potentials in the absence of substrate (E_p) for selected catalysts.

Complex	η (V)	j (mA/cm^2)	$(i_{cat}/i_p)^2$	E_p (V vs. SCE)
1	1.20	1.0	375	-2.10
2	1.24	1.8	492	-2.14
3	1.29	3.4	1674	-2.19
4	1.18	0.99	245	-2.07
5	1.22	1.1	316	-2.11
6	1.25	2.2	978	-2.14
$ReCl(bpy)(CO)_3$	0.81	0.5	12	-1.73

Cyclic voltammograms were recorded in acetonitrile solution (0.5 mM in compound) with 0.1 M $[^nBu_4N]PF_6$ supporting electrolyte, 3 mm glassy carbon working electrode, Pt wire counter electrode, Ag/Ag^+ reference electrode, and scan rate 0.1 V/s.

When the Re compounds are reduced in the presence of CO_2, they behave in a distinct but different fashion compared to **I**. For complexes **1**-**6** in presence of CO_2 no increase in the current of the second reduction is observed, indicating that the species formed does not have sufficient reductive power to react with CO_2, although it can bind CO_2 as suggested by the displacement of the peak. A third reductive wave appears that show catalytic current enhancement by 16-41 times (i_{cat}/i_p). Regarding relative TOF which is proportional to $(i_{cat}/i_p)^2$, order of activity of complex 1-6 varies as **3>6>2>1>5>4**. It is evident that among all six catalysts, **3** and **6** which have benzo-naphthyridine ligand coordination are most active in electroreduction of CO_2. Again, complexes with naphthyridine moiety (**2** and **5**) are more efficient than analogous

quinoline complexes (**1** and **4**). Although all six compounds exhibit higher TOF than I, each complex having pyridine-N coordination to Re are found to be more active than its thiazole-N ligated counterpart (TOF, **3**>**6**, **2**>**5** and **1**>**4**). Similar trend in current density values are observed i.e. pyridine moieties achieve higher current density than analogous thiazole moieties. Considering overpotential values from min. 46% (1.18V, complex **4** vs. 0.81V, **I**) to max. 54% (1.25V, complex **3** vs. 0.81V, **I**), these complexes are less advantageous than **I**. In general, thiazole ligated catalysts exhibit lesser overpotential than respective pyridine coordinated compounds to reach comparable current density. The observed trend of activity can be correlated to the basicity and π-acceptor nature of the coordinating ligands. As mentioned before π-acidicity of the ligands control the reduction potential of the complexes. Benzonaphthyridine moiety being the heighest π- acceptor ligand coordinates most strongly to Re centre (complex **3** and **6**) and causes greatest labilization of Re-Cl bond comparing quinoline and naphthyridine containing complexes. Again, pyridine being more basic than thiazole substituent, forms stronger σ-bond with Re centre and hence weakens Re-Cl bond more than thiazole analogs; Hence the TOF order is observed as complex **3**>**6**, **2**>**5** and **1**>**4**.

2.4.2 Diffusion coefficient and rate constant

In order to determine the diffusion coefficients of the six compounds followed by rate constants of CO_2 catalysis, rotating disk elctrode experiments were carried out. The data obtained display Levich-Kotuckey behaviour as shown in figure 2.10A-F. The Levich-Kotuckey equation and related parameters[13,36] can be expressed as-

$i_L = (0.620)nFAD^{2/3}\omega^{1/2}\upsilon^{-1/6}C$

i_L = Levich current from the rotating disc experiment

n= number of electrons (1 in our case)

F= Faraday's constant (96500 C)

A= area of electrode (0.13cm^2, graphite electrode)

D= diffusion coefficient (cm^2s^{-1}); ω = speed of rotation ($rads^{-1}$)

υ= kinematic viscosity (5.22×10^{-3} cm^2S^{-1} for acetonitrile at 293K)

C= concentration of analyte in solution

Diffusion coefficients for single and doubly reduced species were obtained for all six complexes and are expressed in tabloid form below (Table 2.5). The values of diffusion coefficient for the single reduced species lie in the range 1.2×10^{-5}- 1.7×10^{-5} cm^2s^{-1}, similar to that observed for $Re(bpy)(CO)_3Cl$. Diffusion coefficient of the active catalyst which is actually generated at second reduction, falls in the range 0.4×10^{-5}- 0.7×10^{-5} cm^2s^{-1}, slightly lesser than that observed for Lehn's catalyst.

Table 2.5 Diffusion coefficients and rate constants for complexes under study

Complex	$D_{1st\ redn.}$ (cm^2s^{-1})	$D_{2nd\ redn.}$ (cm^2s^{-1})	k ($M^{-1}s^{-1}$)
1	1.6×10^{-5}	0.6×10^{-5}	263
2	1.2×10^{-5}	0.7×10^{-5}	700
3	1.5×10^{-5}	0.4×10^{-5}	4250
4	1.7×10^{-5}	0.6×10^{-5}	227
5	1.6×10^{-5}	0.6×10^{-5}	295
6	1.5×10^{-5}	0.4×10^{-5}	1850
$Re(bpy)(CO)_3Cl$	1.1×10^{-5}	0.8×10^{-5}	50

Rate constant for CO_2 reduction reaction were also calculated by the equation,

$i_c = nFA[cat](Dk(Q)^y)^{1/2}$

i_c= catalytic current observed in CV

n= number of electrons (2 regarding reduction of CO_2 to CO)

F= Faraday's constant (96500C)

A= area of the electrode surface (7×10^{-4} m^2)

[cat]= concentration of catalyst

D= diifusion coefficient of active catalyst species

k= rate constant

Q= concentration of substrate, CO_2

y= order of the substrate in the reaction

Following the above equation the second order rate constants are calculated for all six rhenium complexes (Table 5). We see a gradual increase in rate constant from quinoline to naphthyridine to benzonaphthyridine ligand in complexes **1**-**3** and in **4**-**6**. Complex **3** and complex **6** having benzonaphthyridine ligands are faster than the rest. Overall, complexes having pyridine coordination (complexes **1, 2** and **3**) exhibit higher rate of CO_2 reduction than those with thiazole ligation (complexes **4, 5** and **6**). All members of this new rhenium family are found to be kinetically more effective than the classic Lehn's complex while complex **3** exhibited highest rate constant ($k=4250$ $M^{-1}s^{-1}$), even greater than Re(bpy-*t*Bu)$(CO)_3$Cl, $k= 650$ $M^{-1}s^{-1}$.

2.4.3 Theoretical calculation

Density functional theory (DFT) calculations on full-atom models were used to study the electronic structure (figure S25-S30) of the series of Re(L)$(CO)_3$Cl complexes (**1**-**6**). We also studied the double reduction products of **1**-**6** that yield the anionic

$[Re(L)(CO)_3Cl]^{2-}$ (**1a-6a**) and the doubly reduced neutral $[Re(L)(CO)_3(CO_2)]K$ (**1b-6b**) complexes. We also explored computationally some putative intermediates in the electrocatalytic reduction of CO_2 to CO by substituting Cl by CO_2 in the doubly reduced models **1a-6a.** The anionic $[Re(L)(CO)_3(CO_2)]^-$ complexes show no stable conformations after gas phase geometry optimization calculations, thus a potassium ion was added to provide charge stabilization.[12]

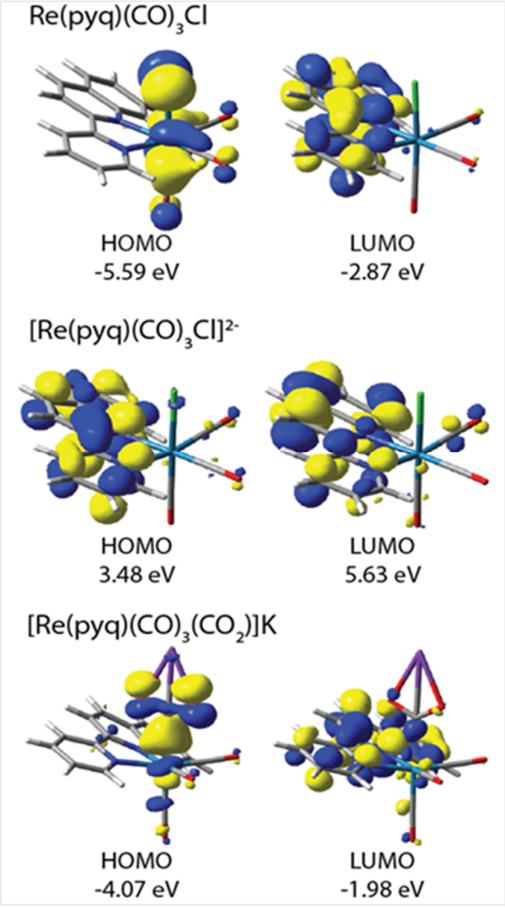

Figure 2.7 HOMO and LUMO diagrams with an isovalue of 0.04 for $Re(pyq)(CO)_3Cl$ (**1**), $[Re(pyq)(CO)_3Cl]^{2-}$ (**1a**), and $[Re(pyq)(CO)_3(CO_2)]K$ (**1b**) complexes.

The highest occupied molecular orbitals (HOMOs) and lowest unoccupied molecular orbitals (LUMOs) of models **1**, **1a**, and **1b** are shown in Figure 5. The MO

diagrams for each set of compounds, **2-6**, **2a-6a**, and **2b-6b** show similar electron density distribution to **1**, **1a**, and **1b** (Tables 8, 9 and 10). Analyses of the HOMO and LUMO wave functions of **1-6** show that the HOMOs have considerable metal contribution ranging from 39 to 41% corresponding to the Re d_{xz} orbital while the LUMO is primarily localized on the diimine ligands, ranging from 91 to 93%. The two-electron reduced models **1a-6a** have similar electronic structures to those of the parent models **1-6**. In **1a-6a**, the HOMOs and LUMOs are bpy ligand based (88 to 93%, and 88 to 98%, respectively). The electronic structure of these models shows that upon reduction the electrons should occupy bpy based orbitals. Substituting CO_2 for the Cl atom in the models of **1a-6a** yields the models **1b-6b**. The electronic structure of these models shows a significant decrease of ligand diimine character in their respective HOMOs and an increase in the metal and CO_2 contributions ranging 23 to 25%, and 49 to 58%, respectively (Tables 11, 12 and 13).

Table 2.6 Heterolytic bond dissociation energies (BDE) for complexes $Re(L)(CO)_3Cl$ (**1-6**), $[Re(L)(CO)_3Cl]^{2-}$ (**1a-6a)**, and $[Re(L)(CO)_3(CO_2)]K$ (**1b-6b)**. Calculated bond lengths of the Re–X (X = Cl or C) bonds in study are also shown.

Comp.	$Re(L)(CO)_3Cl$		$[Re(L)(CO)_3Cl]^{2-}$		$[Re(L)(CO)_3(CO_2)]K$	
	Bond Length (Å)	Heterolytic $BDE_{Re–Cl}$ (kcal mol^{-1})	Bond Length (Å)	Heterolytic $BDE_{Re–Cl}$ (kcal mol^{-1})	Bond Length (Å)	Heterolytic $BDE_{Re–C}$ (kcal mol^{-1})
1	2.51	128.17	2.65	–56.46	2.30	158.12
2	2.51	126.77	2.63	–36.51	2.31	151.24
3	2.51	123.70	2.60	–27.20	2.32	143.71
4	2.50	130.87	2.64	–39.38	2.31	154.06
5	2.51	127.43	2.63	–20.16	2.32	167.22
6	2.51	125.28	2.60	–26.96	2.33	138.54

The heterolytic bond dissociation energies (BDE) for the Re-Cl bond in **1**-**6** and **1a**-**6a** and the Re-CO_2 bond in **1b**-**6b** were calculated to obtain mechanistic information of the electrocatalytic reduction of CO_2 to CO. These energies were obtained from single-point calculations with singlet multiplicities at the optimized geometries of the respective fragments of each complex. In the case of the Re–Cl BDE of **1**-**6**, the metal fraction was treated as a cation (Re^+), while the chlorine atom was treated as an anion (Cl^-). Models **1**-**6** have BDEs ranging from 124 to 130 kcal mol^{-1} (Table 5). The BDE of the Re–Cl bond in models **1a**-**6a** range from –56 to –20 kcal mol^{-1}. Complexes **1a**-**6a** show Re–Cl bond distances ranging from 2.60 to 2.65 Å, which are larger than those bond distances in **1**-**6** (2.50 to 2.51 Å). The BDEs of the Re-CO_2 bonds in models (**1b**-**6b**) range from 144 to 167 kcal mol^{-1}. These bond energies are more stable than the Re-Cl bond energies in the **1**-**6** and **1a**-**6a** models. In the same way, the Re–C bonds in **1b**-**6b** are shorter than the Re–Cl bonds in **1**-**6** by 0.3 Å (Table 6).

We see a continuous decrease in Re-Cl heterolytic bond dissociation energy (128 to 123 kcal mol^{-1}) in compounds 1-2-3 and the same trend is followed (130 to 125 kcal mol^{-1}) in compound 4-5-6. Easier the Re-Cl bond breaking, more facile becomes the interaction between CO_2 to Re center, hence more frequent becomes the turn over. In deeper sense, greater π-conjugation in polypyridyl rings for compounds 3 and 6 upon one electron reduction increases Re-ligand bond strength resulting in weakening of Re-Cl bond. The calculated Re-Cl BDE in the two electron reduced species (1a-6a) generates an opposite trend that does not corroborate with the experimental order of TOF values in Compounds 1-6 probably because of non-existing chloride ion in the structure any more. However, upon replacing Cl by CO_2 again displays decrease in Re-C BDE for compounds 1-3 and 4-6 that means CO_2 if

assumed acting as a ligand, binds strongly to Re centers bearing NAD^+ type ligands. Moreover bond breaking energy for Re-CO_2 is about 20-30 kcal mol^{-1} greater than that of Re-Cl indicating all six compounds gain competent stability upon CO_2 binding.

Addition of a proton to an oxygen in the CO_2 group in **1b** yields model **1c**. The geometry optimized model of **1c** (Figure 6) was used to determine the relative strength of the Re–CO_2H and C–OH bonds in the -CO_2H group. The BDE of the Re–C bond was obtained by considering the $[Re(pyq)(CO)_3]^-$ and $[(CO_2H)K]^{2+}$ fragments, and has a calculated energy of 414 kcal mol^{-1}. This is significantly higher than that in **1b**. Considering the $[Re(pyq)(CO)_3(CO)K]^{2+}$ and $[OH]^-$ fragments, the BDE of the C–OH bond is calculated to be 284 kcal mol^{-1}, this is lower compared to the C-O bond energy in **1b** (755 kcal mol^{-1}) The protonation of CO_2 in **1c** shortens the Re–C bond by by 0.1 Å and it is strengthened by 256 kcal mol^{-1} when compared to model **1b**. This suggests that the reduction of CO_2 to CO is more favorable than the reduction of the Re in the complex.

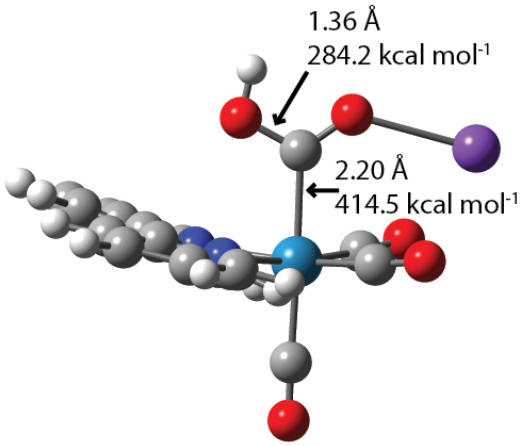

Figure 2.8 Optimized geometry for the $[Re(pyq)(CO)_3(CO_2H)K]^+$ complex (**1c**). Bond lengths and BDEs of the Re–C and C–O bonds are shown

Table 2.8 Electron density percentage of the highest occupied molecular orbitals (HOMOs) of atoms and ligands in their correspondent complex. (a) bipyridine–based ligand, (b) equatorial carbonyl ligand coming into the plane, (c) equatorial carbonyl ligand coming out of the plane.

HOMO Electron Density (%)						
Complex	Re	Cl	L[a]	$CO_{(eq)}$[b]	$CO_{(eq)}$[c]	$CO_{(ax)}$
1	39.53	38.60	2.51	3.35	5.50	10.51
2	40.92	36.50	3.08	4.62	3.94	10.94
3	40.13	37.14	3.32	4.22	4.43	10.76
4	38.54	39.55	2.86	3.08	5.83	10.15
5	40.08	37.20	3.43	4.36	4.22	10.71
6	39.40	37.85	3.51	4.01	4.68	10.55

Table 2.9 Electron density percentage of the lowest unoccupied molecular orbitals (LUMOs) of atoms and ligands in their correspondent complex. (**a**) bipyridine–based ligand, (**b**) equatorial carbonyl ligand coming into the plane, (**c**) equatorial carbonyl ligand coming out of the plane.

	LUMO Electron Density (%)					
Complex	Re	Cl	L[a]	$CO_{(eq)}$[b]	$CO_{(eq)}$[c]	$CO_{(ax)}$
1	3.18	1.66	91.42	1.15	0.89	1.69
2	3.49	1.45	91.81	0.69	0.86	1.70
3	3.10	1.22	92.99	0.57	0.73	1.39
4	3.35	1.55	91.44	1.14	0.67	1.86
5	4.11	1.59	90.62	0.86	0.76	2.06
6	3.86	1.42	91.46	0.76	0.69	1.80

Table 2.10 Molecular orbital (MO) diagrams for each metal complex. Highest occupied molecular orbital (HOMO) and lowest unoccupied molecular orbital (LUMO) showing contour surface diagrams with an isovalue of 0.04 are shown.

Complex	HOMO	LUMO
1	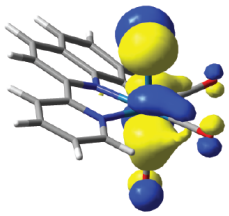	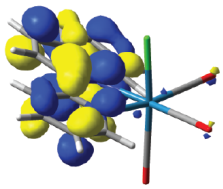
2	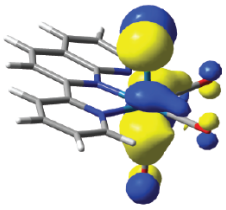	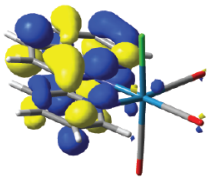
3	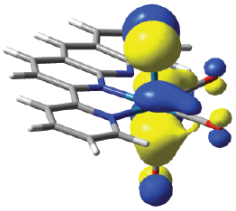	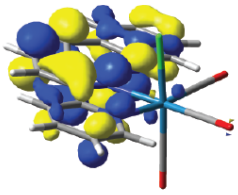
4	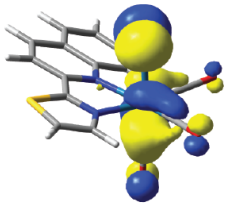	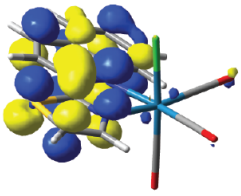
5	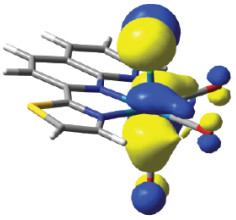	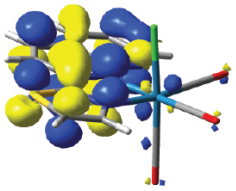
6	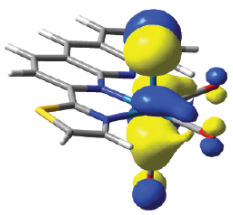	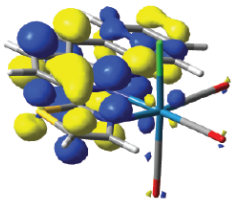

Table 2.11 Electron density percentage of the highest occupied molecular orbitals (HOMOs) for the $Re(L)(CO)_3(CO_2K)$ complexes. (**a**) bipyridine–based ligand, (**b**) equatorial carbonyl ligand coming into the plane, (**c**) equatorial carbonyl ligand coming out of the plane.

	HOMO Electron Density (%)					
Complex	Re	CO_2K	L[a]	$CO_{(eq)}$[b]	$CO_{(eq)}$[c]	$CO_{(ax)}$
1a	25.33	57.53	8.56	1.51	1.64	5.43
2a	24.40	55.07	12.08	1.30	1.65	5.50
3a	23.89	52.98	14.80	1.21	1.47	5.65
4a	25.06	55.43	11.25	1.47	1.64	5.16
5a	23.95	52.01	16.02	1.18	1.56	5.28
6a	23.28	49.22	19.68	1.07	1.33	5.42

Table 2.12 Electron density percentage of the lowest unoccupied molecular orbitals (LUMOs) for the $Re(L)(CO)_3(CO_2K)$ complexes: (**a**) bipyridine–based ligand, (**b**) equatorial carbonyl ligand coming into the plane, (**c**) equatorial carbonyl ligand coming out of the plane.

	LUMO Electron Density (%)					
Complex	Re	CO_2K	L[a]	$CO_{(axial)}$[b]	$CO_{(axial)}$[c]	$CO_{(equatorial)}$
1a	3.67	12.35	79.16	0.79	0.64	3.40
2a	4.82	11.51	78.64	0.51	0.59	3.92
3a	5.11	10.33	80.01	0.41	0.43	3.71
4a	4.08	11.89	78.73	0.80	0.56	3.94
5a	5.71	12.80	75.57	0.59	0.56	4.78
6a	6.31	12.20	75.83	0.48	0.42	4.76

Table 2.13 Molecular orbital (MO) diagrams of the $Re(L)(CO)_3(CO_2K)$ complexes. Highest occupied molecular orbital (HOMO) and lowest unoccupied molecular orbital (LUMO) showing contour surface diagrams with an isovalue of 0.04 are shown.

Complex	HOMO	LUMO
1a	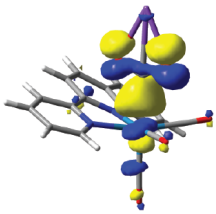	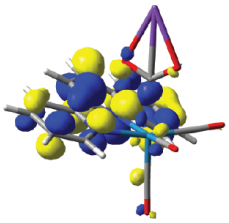
2a	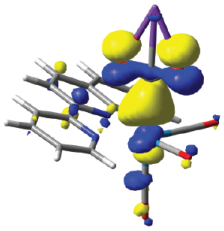	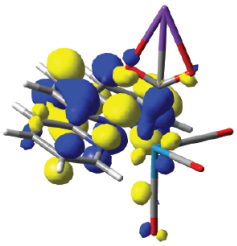
3a	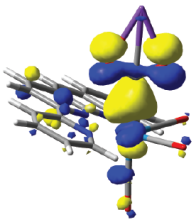	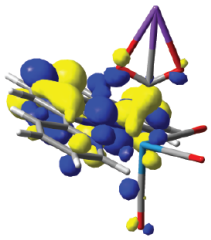
4a	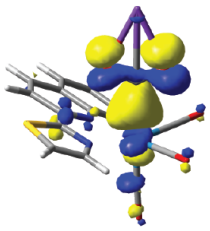	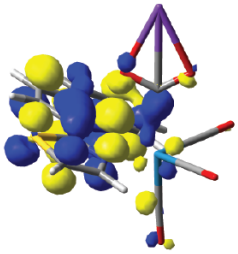
5a	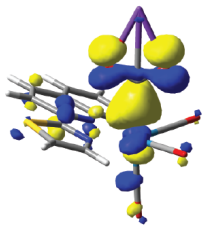	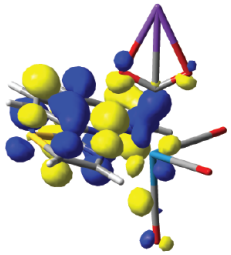
6a	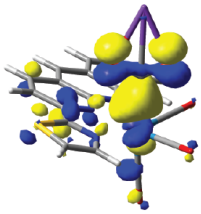	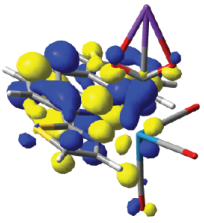

2.5 Conclusion

We have prepared and characterized mononuclear complexes of the general formula Re(diimine)$(CO)_3Cl$ and tested their activity with regard to the reduction of CO_2. The diimine ligands have been systematically modified so as to alter the electronic properties and improve their electrochemical behavior in favor of catalysis. It is notable that the relative turnover is much faster for the rhenium complexes with larger pi system, recognized as NAD^+ model ligands. The catalytic activity of the synthesized complexes can be explained by the basicity and π-acidic nature of the coordinating ligands. Greater the π-acceptance ability (benzonaphthyridine> naphthyridine> quinoline), stronger is the Re-N bond and hence easier is the Re-Cl bond breaking. Again, more basic pyridine substituent coordinates stronger to metal centre than analogous thiazole containing ligands and participates in faster Re-Cl bond dissociation. Overall, our study provides important insight into the design and study of rhenium-based CO_2 reduction catalysts.

2.6. NMR and Levich-Kotuckey plot and geometry optimized structures for compounds 1-6

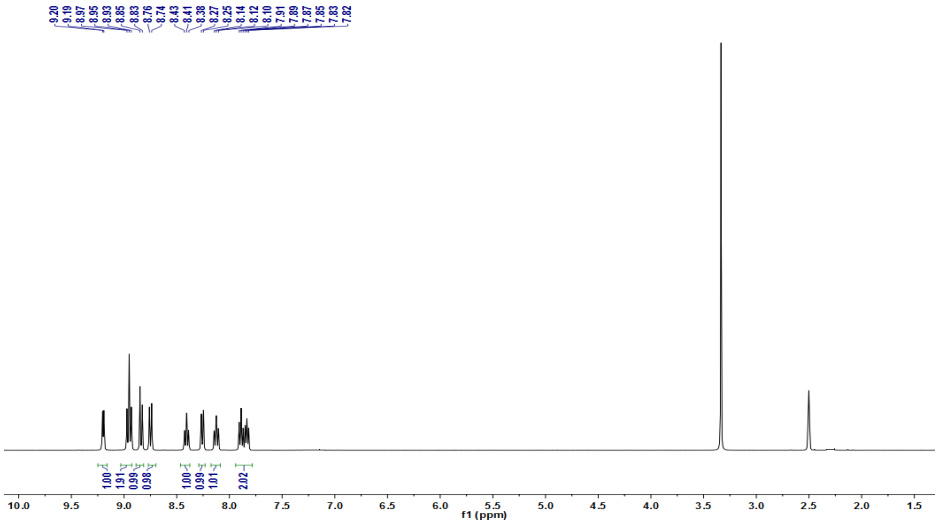

Figure 2.9A Full ^{1}H-NMR spectrum of Re(pyq)$(CO)_3Cl$ **(1)** in DMSO–d_6.

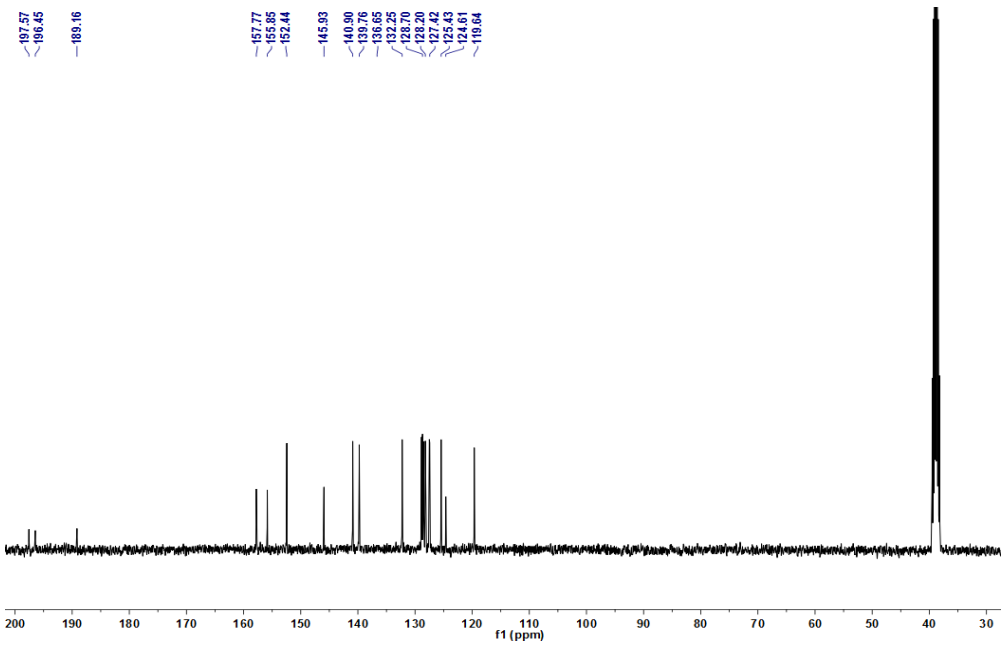

Figure 2.9B Full ^{13}C-NMR spectrum of Re(pyq)(CO)$_3$Cl **(1)** in DMSO–d_6.

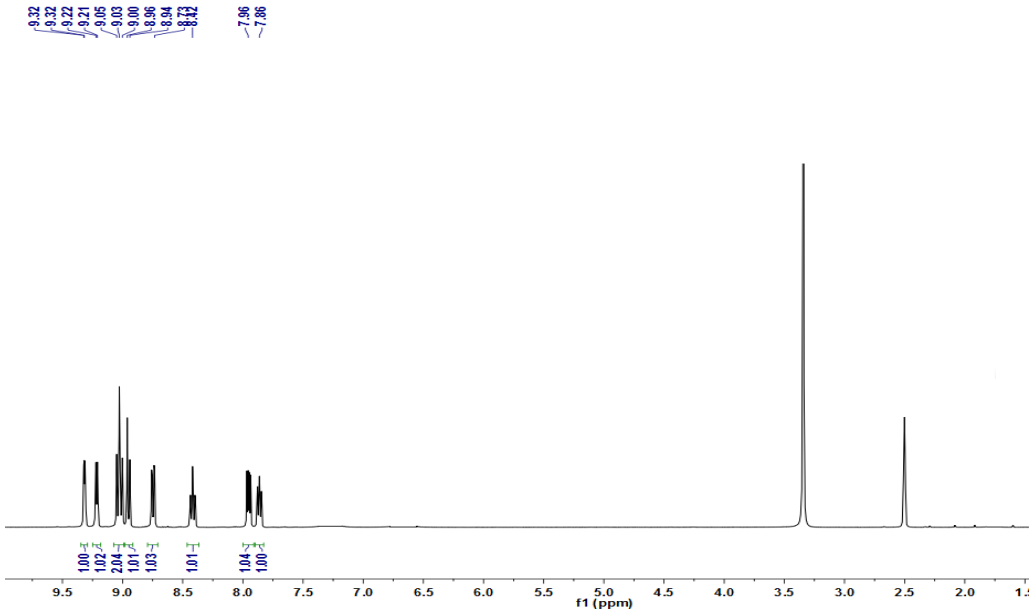

Figure 2.9C Full ^{1}H-NMR spectrum of Re(pynp)(CO)$_3$Cl **(2)** in DMSO-d_6

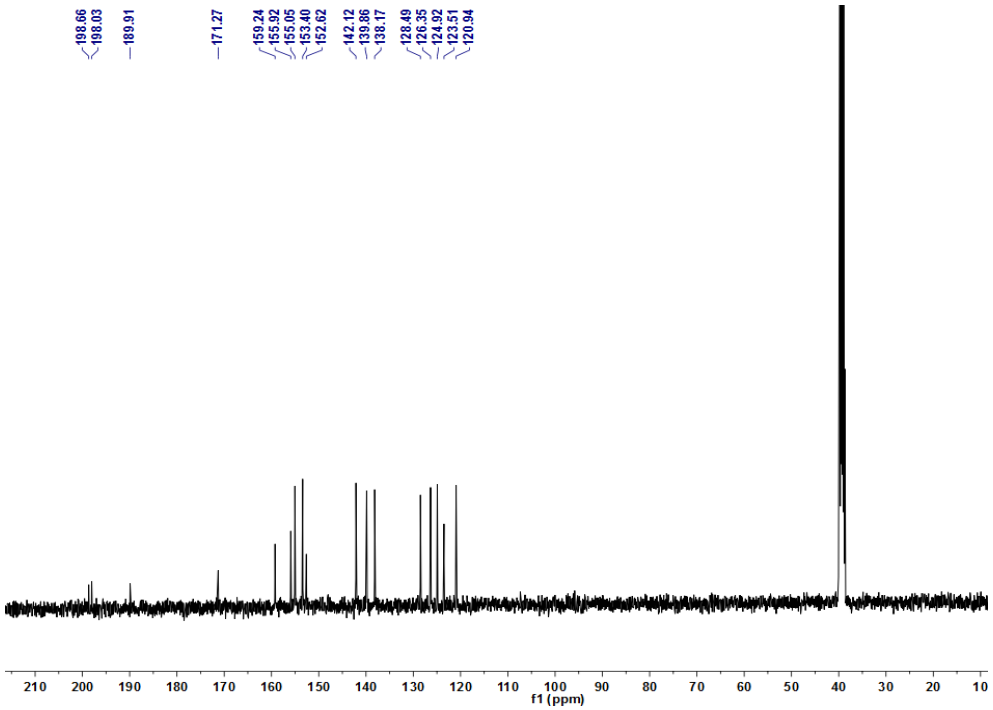

Figure 2.9D Full ^{13}C-NMR spectrum of Re(pynp)(CO)$_3$Cl **(2)** in DMSO–d_6.

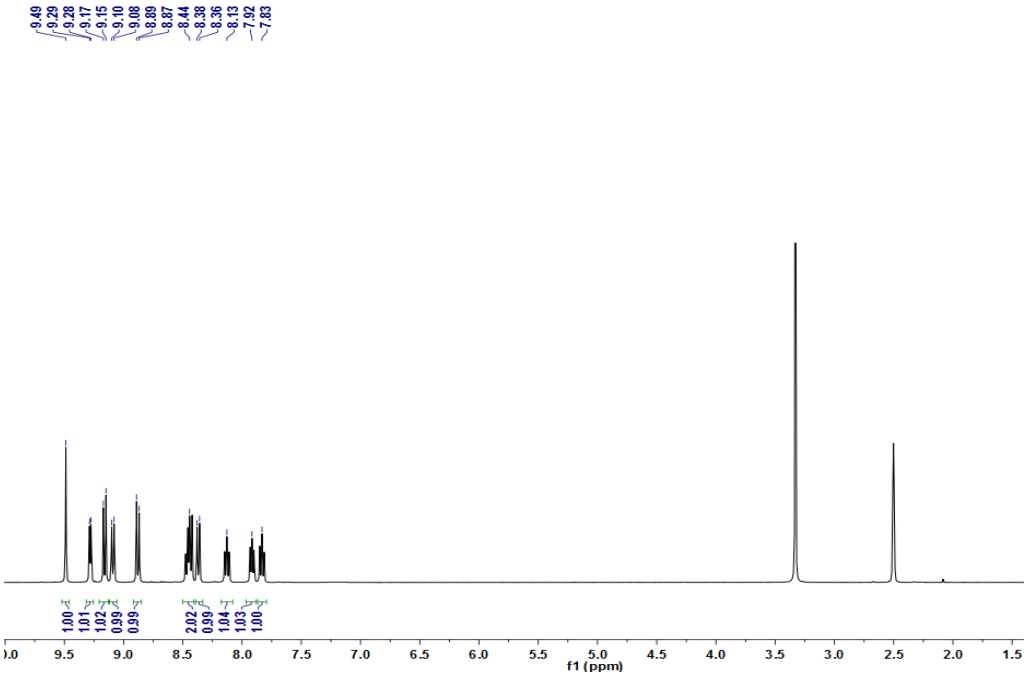

Figure 2.9E Full ^{1}H-NMR spectrum of Re(pybnp)(CO)$_3$Cl **(3)** in DMSO-d_6

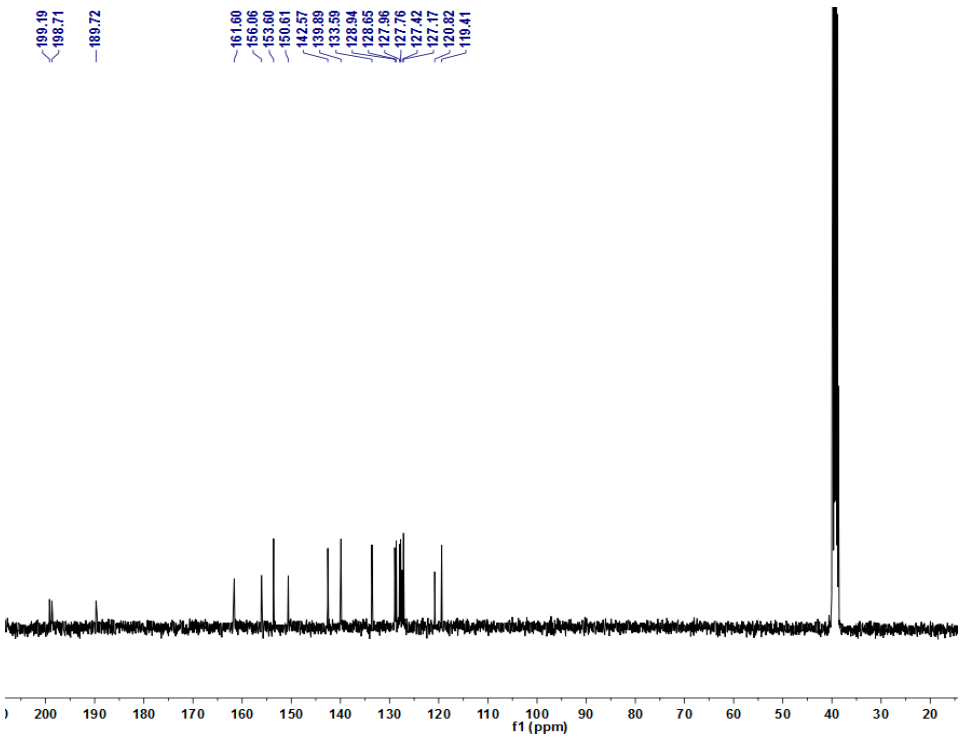

Figure 2.9F Full ^{13}C-NMR spectrum of Re(pybnp)(CO)$_3$Cl **(3)** in DMSO–d_6.

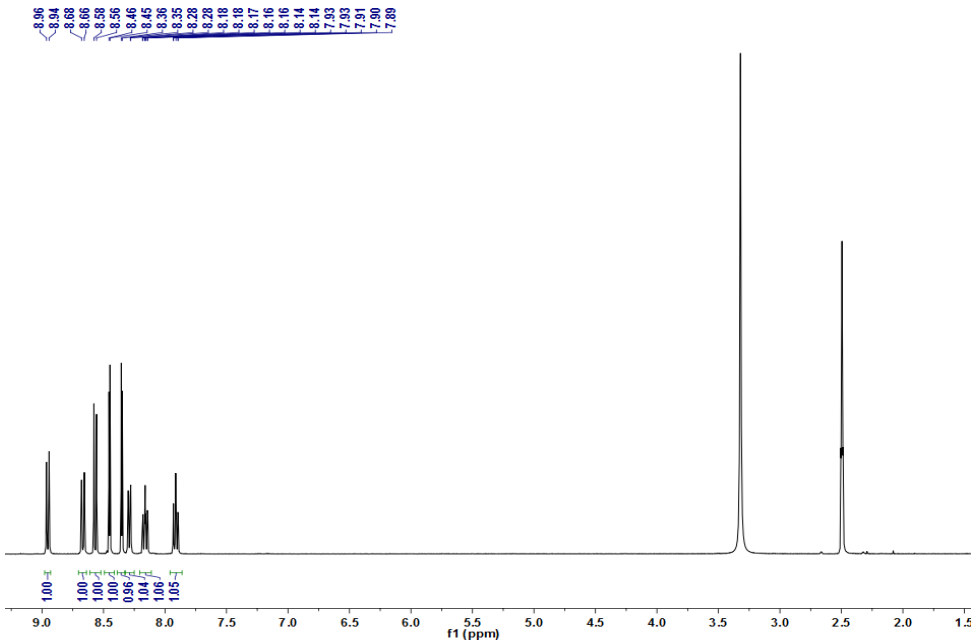

Figure 2.9G Full ^{1}H-NMR spectrum of Re(thq)(CO)$_3$Cl **(4)** in DMSO-d_6.

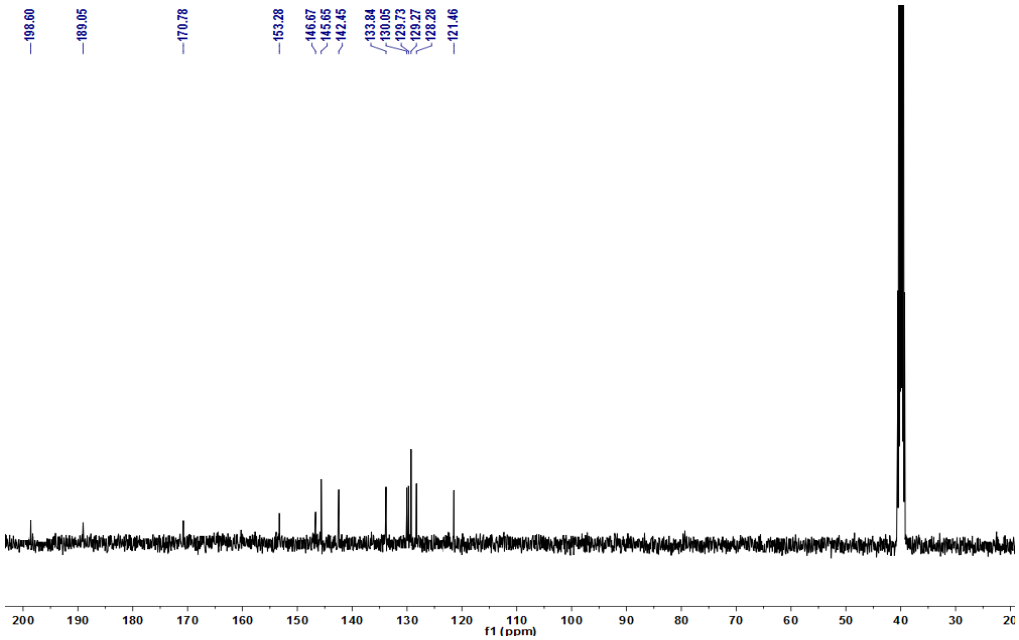

Figure 2.9H Full ^{13}C-NMR spectrum of Re(thq)(CO)$_3$Cl **(4)** in DMSO–d_6.

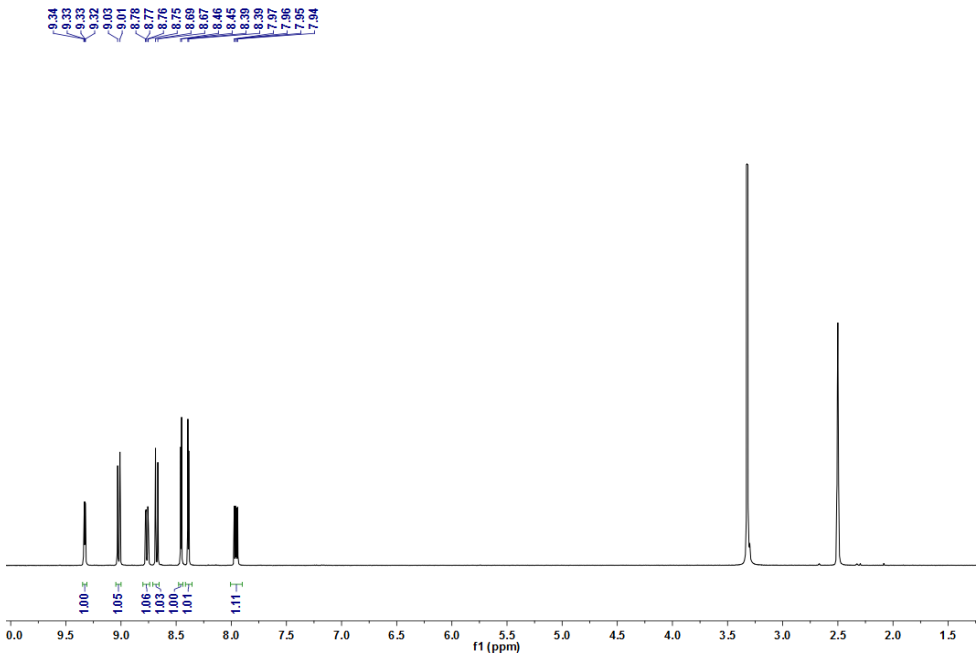

Figure 2.9I Full ^{1}H-NMR spectrum of Re(thnp)(CO)$_3$Cl **(5)** in DMSO-d_6.

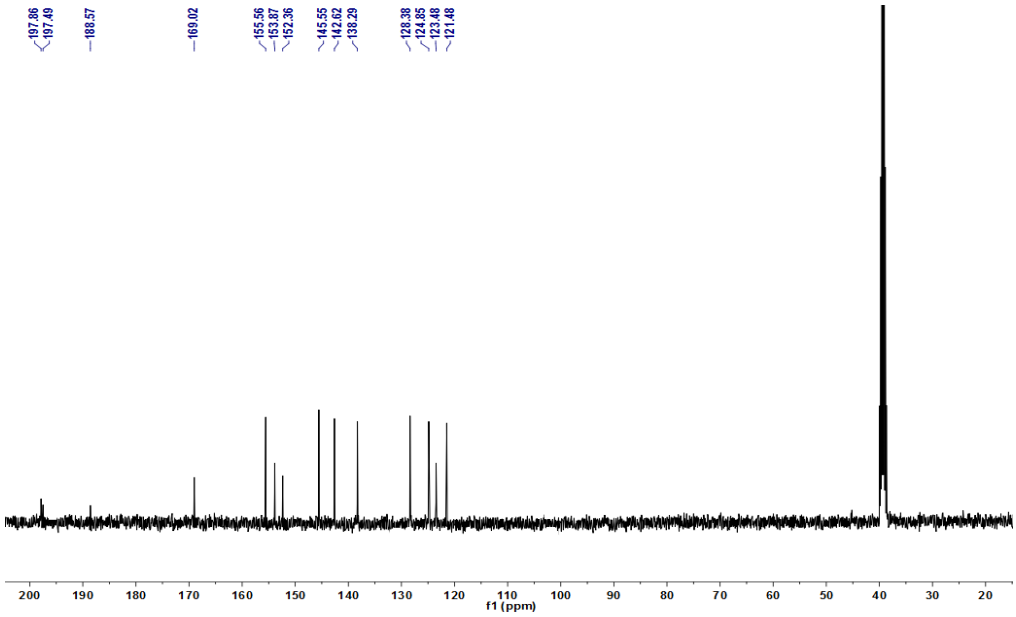

Figure 2.9J Full ^{13}C-NMR spectrum of Re(thnp)$(CO)_3$Cl **(5)** in DMSO–d_6.

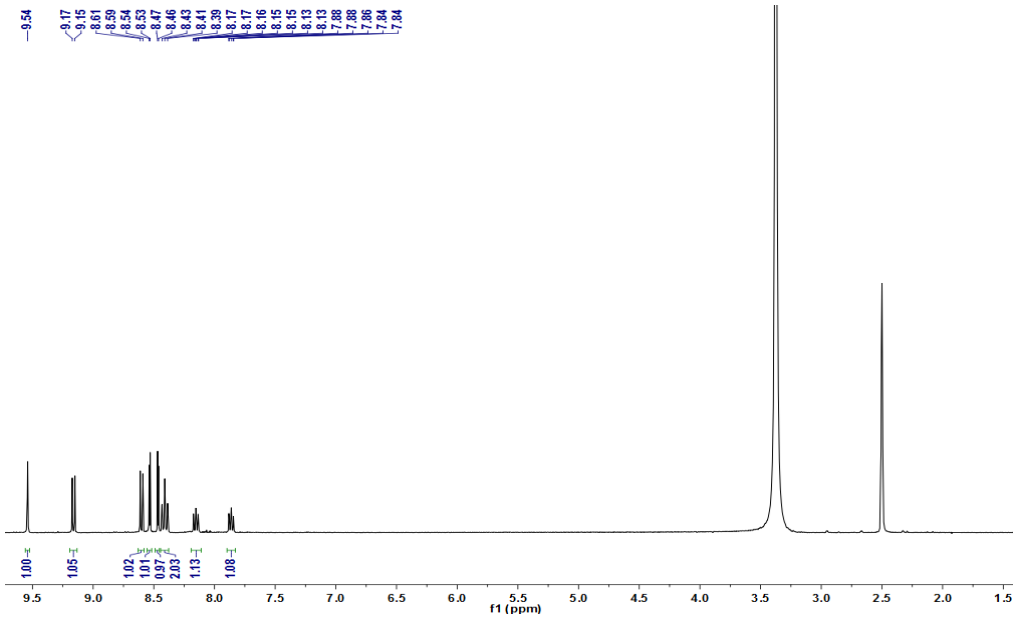

Figure 2.9K Full ^{1}H-NMR spectrum of Re(thbnp)$(CO)_3$Cl **(6)** in DMSO-d_6.

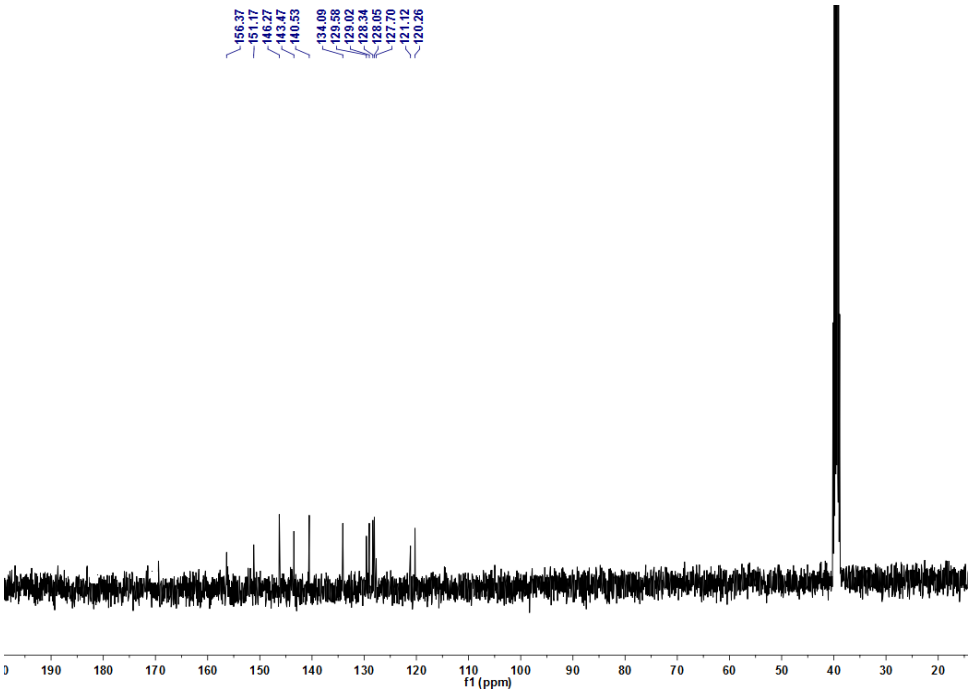

Figure 2.9L: Full ^{13}C-NMR spectrum of Re(thbnp)$(CO)_3$Cl **(6)** in DMSO–d_6.

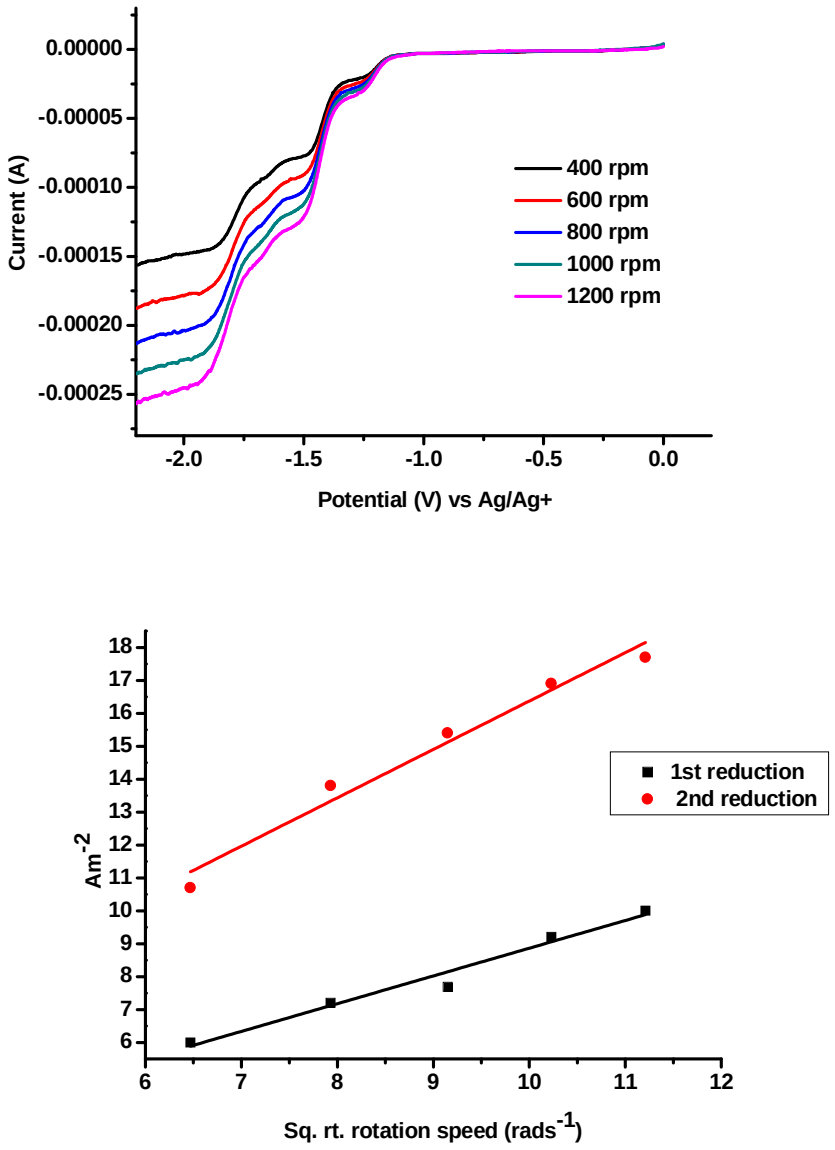

Figure 2.10A Rotating disk electrode data (top) and Levich-Koutecky plot (bottom) for 1mM $Re(pyq)(CO)_3Cl$ **(1)** with 0.1M $TBAPF_6$ as supporting electrolyte under N_2

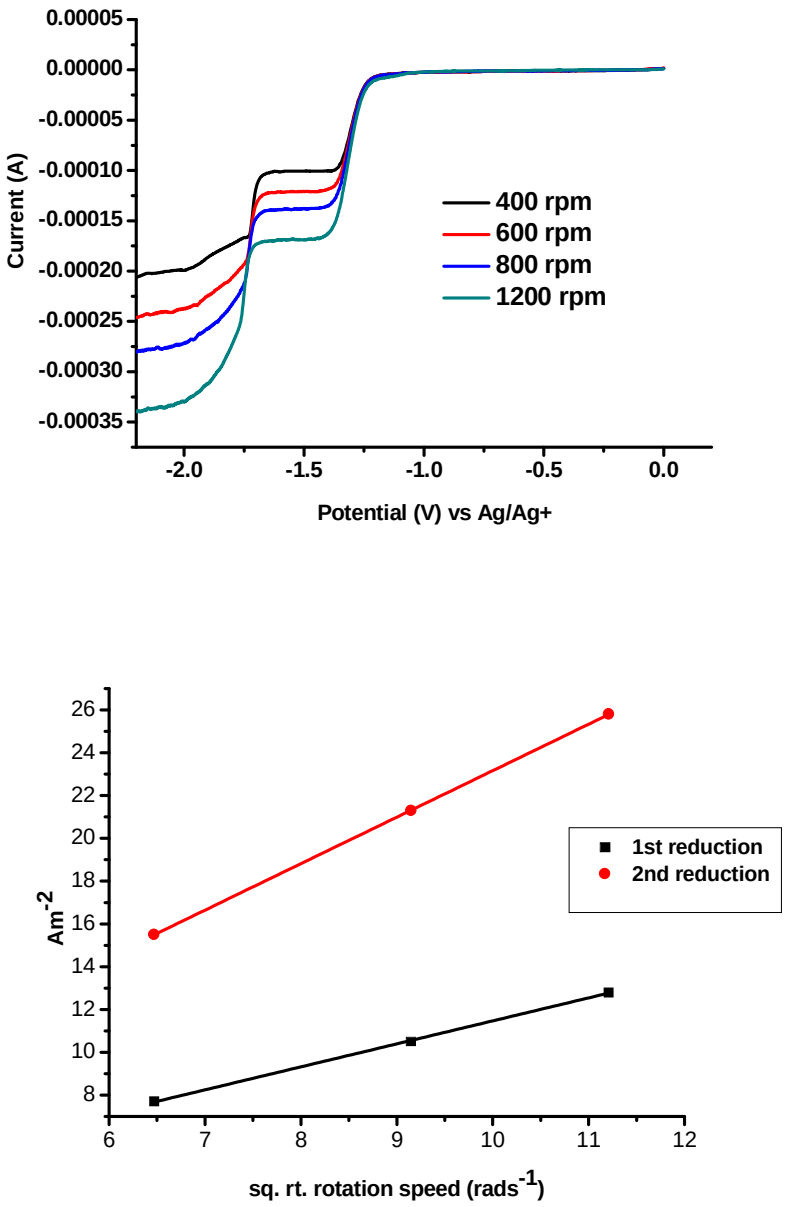

Figure 2.10B Rotating disk electrode data (top) and Levich-Koutecky plot (bottom) for 1mM Re(pynp)$(CO)_3Cl$ **(2)** with 0.1M $TBAPF_6$ as supporting electrolyte under N_2

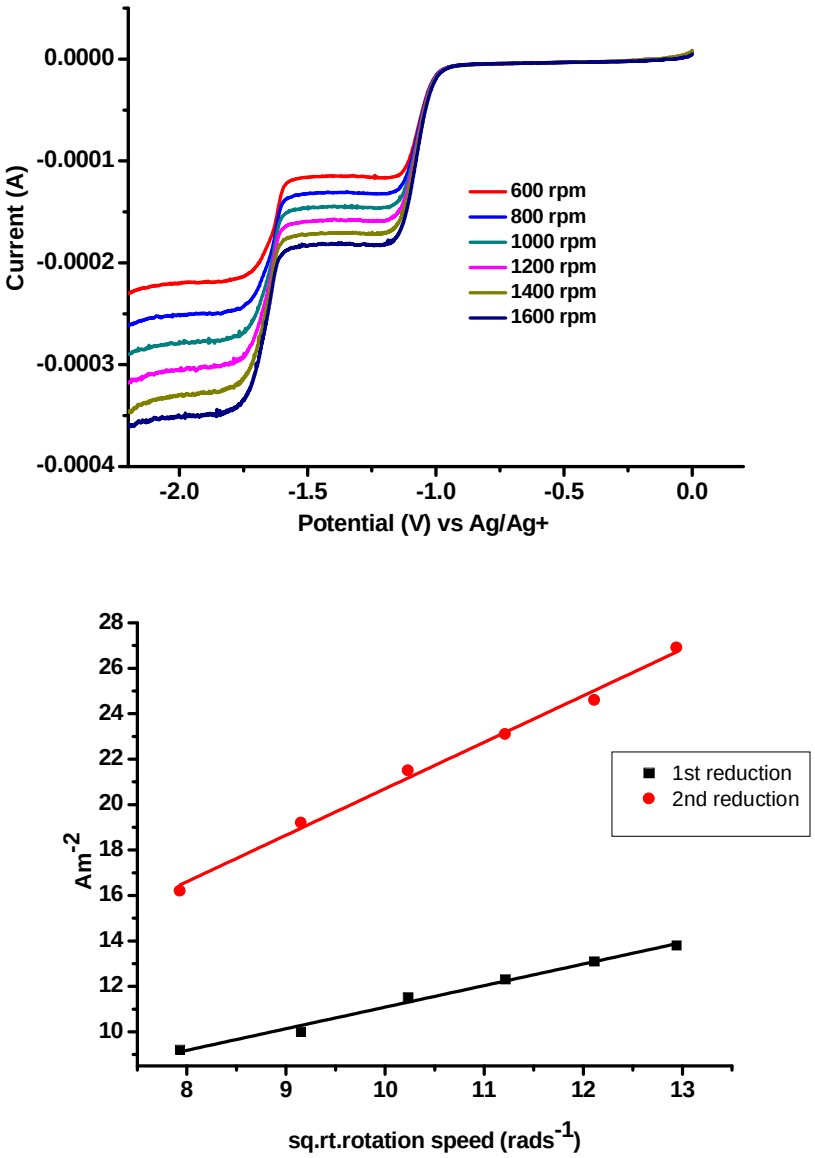

Figure 2.10C Rotating disk electrode data (top) and Levich-Koutecky plot (bottom) for 1mM Re(pybnp)$(CO)_3Cl$ **(3)** with 0.1M $TBAPF_6$ as the supporting electrolyte under nitrogen

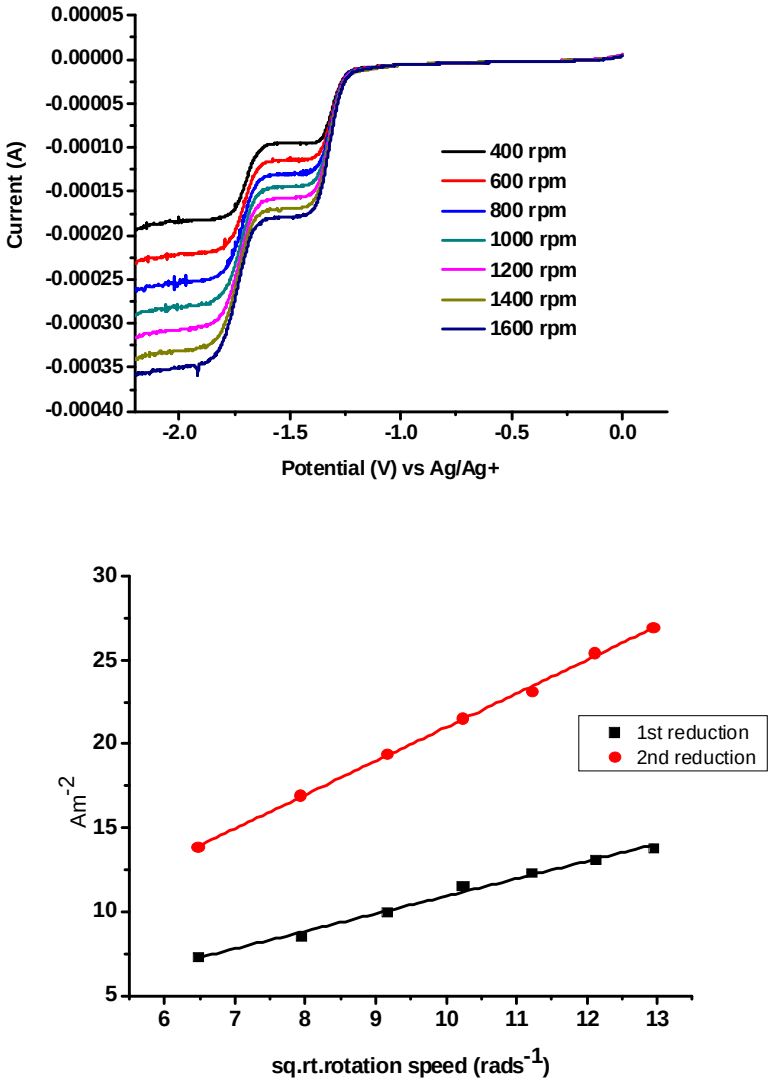

Figure 2.10D Rotating disk electrode data (top) and Levich-Koutecky plot (bottom) for 1mM $Re(thq)(CO)_3Cl$ **(4)** with 0.1M $TBAPF_6$ as supporting electrolyte under N_2

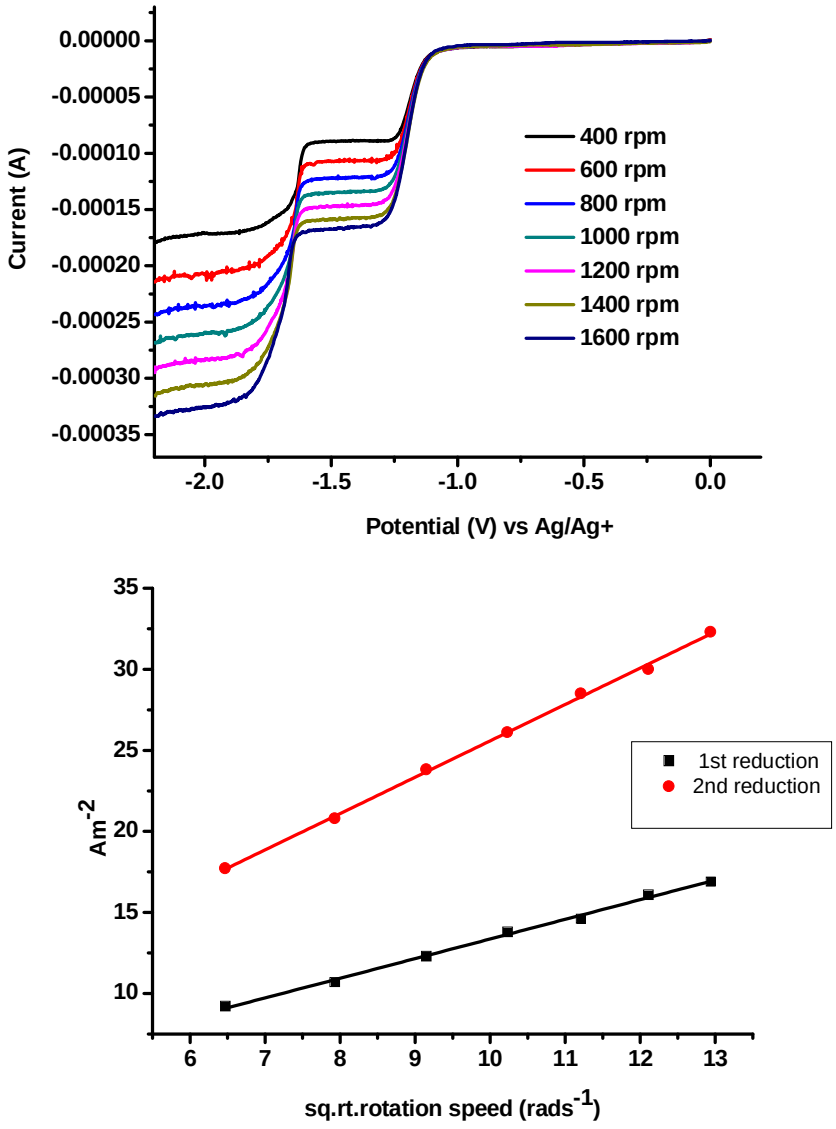

Figure 2.10E Rotating disk electrode data (top) and Levich-Koutecky plot (bottom) for 1mM $Re(thnp)(CO)_3Cl$ **(5)** with 0.1M $TBAPF_6$ as supporting electrolyte under N_2

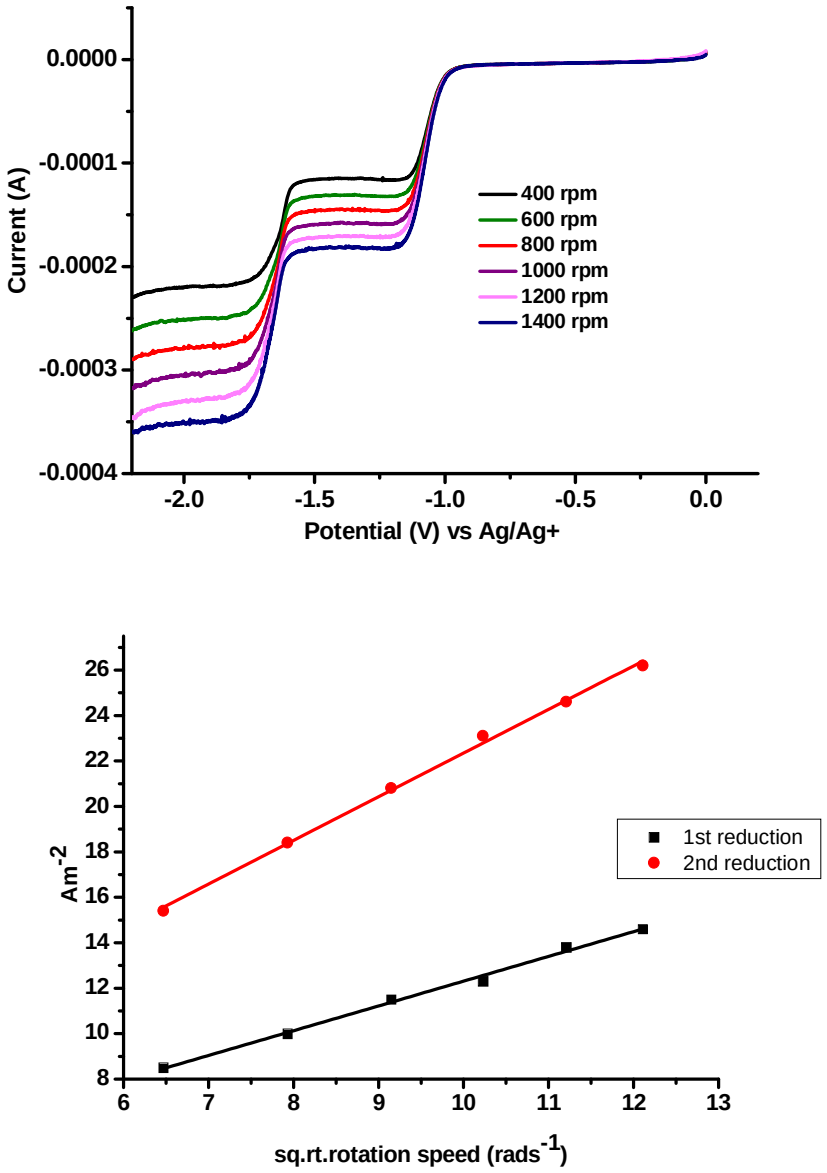

Figure 2.10F Rotating disk electrode data (top) and Levich-Koutecky plot (bottom) for 1mM Re(thbnp)$(CO)_3Cl$ **(6)** with 0.1M $TBAPF_6$ as supporting electrolyte under N_2

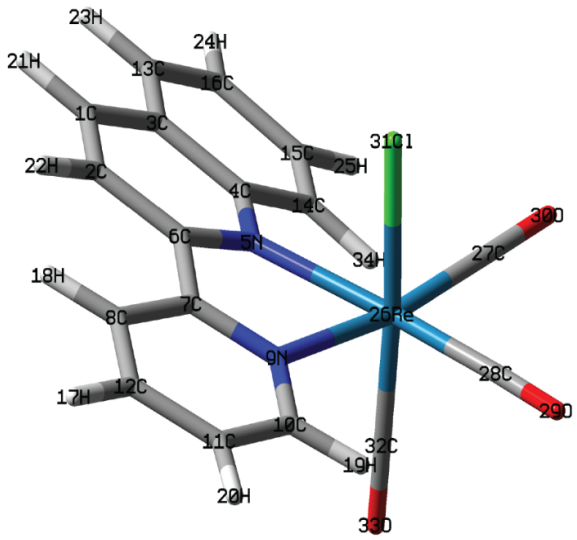

Figure 2.11A Geometry optimized structure for complex **1** with labeled atoms.

Table 2.14 Selected bond lengths for atoms of complex **1**.

Atoms (Labels)	Distance (Å)
Re(26)–Cl(31)	2.50916
Re(26)–C(27)	1.93751
Re(26)–C(28)	1.92152
Re(26)–C(32)	1.92268
Re(26)–N(5)	2.26652
Re(26)–N(9)	2.19133
C(27)–O(30)	1.15908
C(28)–O(29)	1.16138
C(32)–O(33)	1.16532

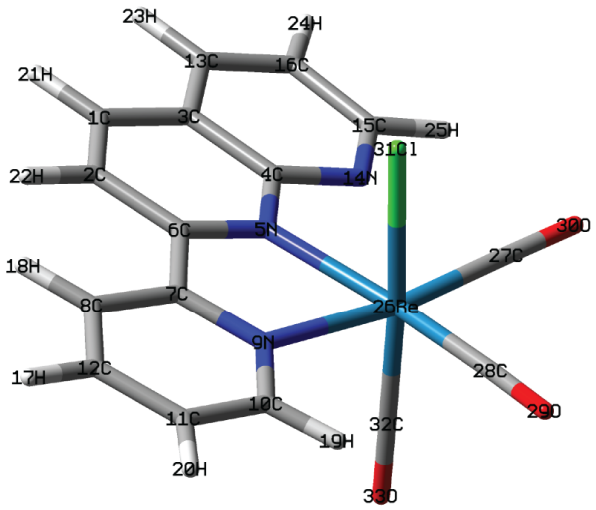

Figure 2.11B Geometry optimized structure for complex 2 with labeled atoms.

Table 2.15 Selected bond lengths for atoms of complex **2**.

Atoms (Labels)	Distance (Å)
Re(26)–Cl(31)	2.51276
Re(26)–C(27)	1.94494
Re(26)–C(28)	1.91939
Re(26)–C(32)	1.92259
Re(26)–N(5)	2.23762
Re(26)–N(9)	2.19398
Re(26)–N(14)	3.32251
C(27)–O(30)	1.15656
C(28)–O(29)	1.16283
C(32)–O(33)	1.16543

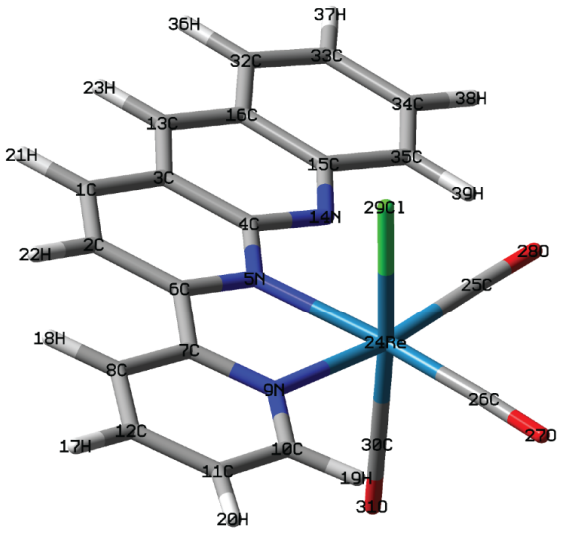

Figure 2.11C Geometry optimized structure for complex **3** with labeled atoms.

Table 2.16 Selected bond lengths for atoms of complex **3**.

Atoms (Labels)	Distance (Å)
Re(24)–Cl(29)	2.51178
Re(24)–C(25)	1.94187
Re(24)–C(26)	1.92015
Re(24)–C(30)	1.92323
Re(24)–N(5)	2.23524
Re(24)–N(9)	2.19369
Re(24)–N(14)	3.32342
C(25)–O(28)	1.15805
C(26)–O(27)	1.16282
C(30)–O(31)	1.16531

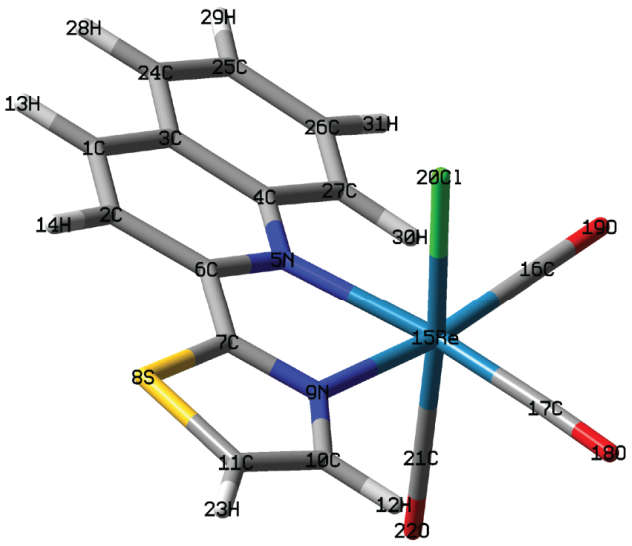

Figure 2.11D Geometry optimized structure for complex **4** with labeled atoms.

Table 2.17 Selected bond lengths for atoms of complex **4**.

Atoms (Labels)	Distance (Å)
Re(15)–Cl(20)	2.50403
Re(15)–C(16)	1.93539
Re(15)–C(17)	1.91778
Re(15)–C(21)	1.92468
Re(15)–N(5)	2.30807
Re(15)–N(9)	2.18298
C(16)–O(19)	1.15922
C(17)–O(18)	1.16113
C(21)–O(22)	1.16456

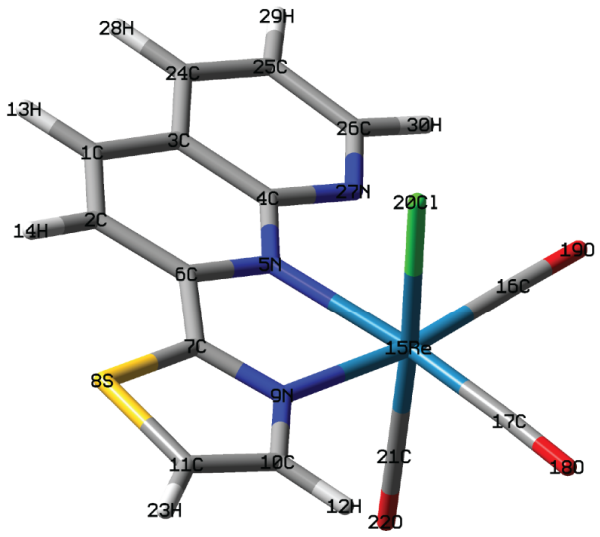

Figure 2.11E Geometry optimized structure for complex **5** with labeled atoms.

Table 2.18 Selected bond lengths for atoms of complex **5.**

Atoms (Labels)	Distance (Å)
Re(15)–Cl(20)	2.50963
Re(15)–C(16)	1.94478
Re(15)–C(17)	1.91865
Re(15)–C(21)	1.92403
Re(15)–N(5)	2.26032
Re(15)–N(9)	2.18347
Re(15)–N(27)	3.36560
C(16)–O(19)	1.15599
C(17)–O(18)	1.16194
C(21)–O(22)	1.16493

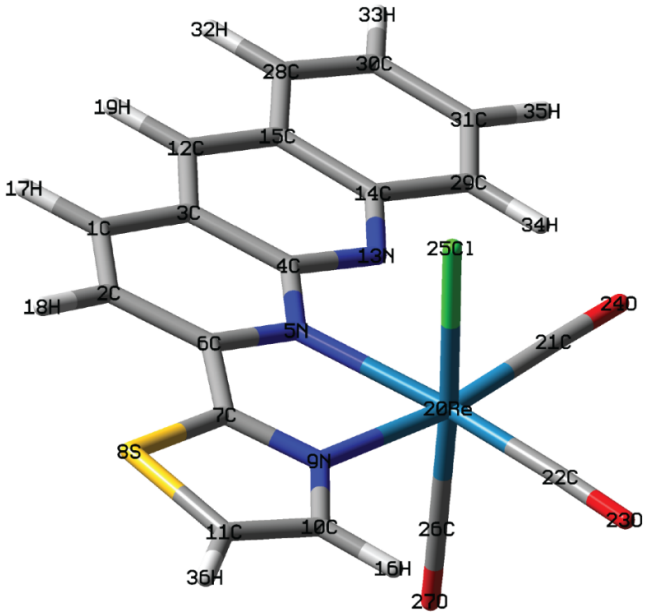

Figure 2.11F Geometry optimized structure for complex **6** with labeled atoms.

Table 2.19 Selected bond lengths for atoms of complex **6**.

Atoms (Labels)	Distance (Å)
Re(20)–Cl(25)	2.50867
Re(20)–C(21)	1.94216
Re(20)–C(22)	1.91993
Re(20)–C(26)	1.92469
Re(20)–N(5)	2.25675
Re(20)–N(9)	2.18272
Re(20)–N(13)	3.36433
C(21)–O(24)	1.15748
C(22)–O(23)	1.16185
C(26)–O(27)	1.16481

References

(1) Monastersky, R. *Nature* **2013**, *497*, 13-14.
(2) Bala, G. *Current science* **2013**, *104*, 1471-1471.
(3) Züttel, A.; Mauron, P.; Kato, S.; Callini, E.; Holzer, M.; Huang, J. *CHIMIA International Journal for Chemistry* **2015**, *69*, 264-268.
(4) Benson, E. E.; Kubiak, C. P.; Sathrum, A. J.; Smieja, J. M. *Chem. Soc. Rev.* **2009**, *38*, 89-99.
(5) Yin, X.; Moss, J. R. *Coord. Chem. Rev.* **1999**, *181*, 27-59.
(6) Takeda, H.; Koike, K.; Inoue, H.; Ishitani, O. *J. Am. Chem. Soc.* **2008**, *130*, 2023-2031.
(7) Morris, A. J.; Meyer, G. J.; Fujita, E. *Acc. Chem. Res.* **2009**, *42*, 1983-1994.
(8) Bourrez, M.; Molton, F.; Chardon-Noblat, S.; Deronzier, A. *Angew. Chem.* **2011**, *123*, 10077-10080.
(9) Hawecker, J.; Lehn, J.-M.; Ziessel, R. *Journal of the Chemical Society, Chemical Communications* **1984**, 328-330.
(10) Maher, J. M.; Cooper, N. J. *J. Am. Chem. Soc.* **1980**, *102*, 7604-7606.
(11) Doherty, M. D.; Grills, D. C.; Muckerman, J. T.; Polyansky, D. E.; Fujita, E. *Coord. Chem. Rev.* **2010**, *254*, 2472-2482.
(12) Keith, J. A.; Grice, K. A.; Kubiak, C. P.; Carter, E. A. *J. Am. Chem. Soc.* **2013**, *135*, 15823-15829.
(13) Smieja, J. M.; Kubiak, C. P. *Inorg. Chem.* **2010**, *49*, 9283-9289.
(14) Grice, K. A.; Gu, N. X.; Sampson, M. D.; Kubiak, C. P. *Dalton Transactions* **2013**, *42*, 8498-8503.
(15) Cohen, B. W.; Polyansky, D. E.; Zong, R.; Zhou, H.; Ouk, T.; Cabelli, D. E.; Thummel, R. P.; Fujita, E. *Inorg. Chem.* **2010**, *49*, 8034-8044.
(16) Patra, S. K.; Sadhukhan, N.; Bera, J. K. *Inorg. Chem.* **2006**, *45*, 4007-4015.
(17) Pavlishchuk, V. V.; Addison, A. W. *Inorganica Chimica Acta* **2000**, *298*, 97-102.
(18) Sheldrick, G. M. *Acta Crystallographica Section A: Foundations of Crystallography* **2008**, *64*, 112-122.
(19) Parr, R. G. In *Horizons of Quantum Chemistry*; Springer: 1980, p 5-15.
(20) Becke, A. D. *Physical review A* **1988**, *38*, 3098.
(21) Becke, A. D. *J. Chem. Phys.* **1993**, *98*, 1372-1377.
(22) Lee, C.; Yang, W.; Parr, R. G. *Physical review B* **1988**, *37*, 785.
(23) Gaussian, F. *Wallingford, CT* **2009**.
(24) Petersson, a.; Bennett, A.; Tensfeldt, T. G.; Al-Laham, M. A.; Shirley, W. A.; Mantzaris, J. *J. Chem. Phys.* **1988**, *89*, 2193-2218.
(25) Couty, M.; Hall, M. B. *J. Comput. Chem* **1996**, *17*, 1359-1370.
(26) Petersson, G.; Tensfeldt, T. G.; Montgomery Jr, J. *J. Chem. Phys.* **1991**, *94*, 6091-6101.
(27) Hevia, E.; Pérez, J.; Riera, V.; Miguel, D.; Kassel, S.; Rheingold, A. *Inorg. Chem.* **2002**, *41*, 4673-4679.
(28) Czerwieniec, R.; Kapturkiewicz, A.; Lipkowski, J.; Nowacki, J. *Inorganica chimica acta* **2005**, *358*, 2701-2710.
(29) Kraihanzel, C.; Cotton, F. *Inorg. Chem.* **1963**, *2*, 533-540.
(30) Cotton, F.-A. *Inorg. Chem.* **1964**, *3*, 702-711.
(31) Caspar, J. V.; Meyer, T. J. *The Journal of Physical Chemistry* **1983**, *87*, 952-957.

(32) Grupp, A.; Bubrin, M.; Ehret, F.; Kvapilová, H.; Záliš, S.; Kaim, W. *Journal of Organometallic Chemistry* **2014**, *751*, 678-685.
(33) Aguirre, J. D.; Lutterman, D. A.; Angeles-Boza, A. M.; Dunbar, K. R.; Turro, C. *Inorg. Chem.* **2007**, *46*, 7494-7502.
(34) Matsubara, Y.; Hightower, S. E.; Chen, J.; Grills, D. C.; Polyansky, D. E.; Muckerman, J. T.; Tanaka, K.; Fujita, E. *Chem. Commun.* **2014**, *50*, 728-730.
(35) Appel, A. M.; Helm, M. L. *ACS Catal.* **2014**, *4*, 630-633.
(36) Smieja, J. M.; Sampson, M. D.; Grice, K. A.; Benson, E. E.; Froehlich, J. D.; Kubiak, C. P. *Inorg. Chem.* **2013**, *52*, 2484-2491.

CHAPTER 3. Ullmann Reaction Catalyzed by Heterogeneous Mesoporous Copper/Manganese Oxide: A Kinetic and Mechanistic Analysis

3.1 Abstract

In this chapter, a heterogeneous copper oxide supported on mesoporous manganese oxide (meso Cu/MnO_x) was explored for Ullmann-type cross coupling reactions. An inverse micelle templated evaporation induced self-assembly method with *in situ* addition of copper was adopted to synthesize the mesoporous catalyst. Broad substrate scope and excellent functional group tolerability in C-O, C-N, and C-S bond formation reactions were observed using the optimized reaction conditions. The catalytic protocol was ligand free and the catalyst was reusable without any significant loss of activity. The kinetic and Hammett analyses provided evidence for oxidative addition followed by nucleophilic addition and reductive elimination at the active copper oxide surface. Rate acceleration was observed for aryl halides with electron withdrawing groups. The Hammett analysis determined ρ = +1.0 indicative of an oxidative addition, whereas the electronic effect in the phenol ring (ρ = -2.893) was indicative of coordination to a metal ion. Theoretically, the oxidative addition of the aryl halides is assisted by the ligand environment of the copper center. Relevant mechanistic implications are discussed based on the experimental and computational results.

3.2 Introduction

Construction of C-heteroatom (O, N and S) bonds is considered a popular and powerful technique by synthetic chemists due to their potential applications in the synthesis of pharmaceuticals, polymers and natural products.[1-7] Copper catalyzed Ullmann-type condensation reaction is an attractive methodology due to the lower cost and decreased toxicity of copper over classic palladium catalysts used for coupling of C-O bonds.[8,9] The traditional method developed by Fritz Ullmann and Irma Goldberg a century ago relied upon stoichiometric copper and very high reaction temperatures.[10] This reaction is nowadays known as the "classical Ullmann reaction. Over the last decade, catalytic protocols for copper mediated Ullmann ether coupling has been explored and improved, although most catalysts that accelerate this reaction are typically used under homogeneous reaction conditions.[1-3,11-14] Heterogeneous copper-based catalysts for Ullmann-type condensation reactions, however, may evolve as a more suitable system because of crucial advantages such as easy separation of products, recyclability, and high stability of catalysts.[15] In 2007, Lipshutz *et al*. reported microwave-assisted Cu/C (copper-in-charcoal) promoted diaryl ether synthesis in the presence of 1,10-phenanthroline.[16] In subsequent years several heterogeneous copper catalysts have been explored and some of the systems include CuO nanoparticles,[7] copper powder,[17] copper fluorapatite,[18] CuO supported on N-doped carbon (Meso-N-C-1),[19] Cu/ligand catalyst immobilized on silica,[8] Cu-Fe-hydrotalcite,[20] magnetite-supported copper (nanocat-Fe-CuO) nanoparticles,[21] alumina-supported CuO[22] and CuI immobilized on MOF.[23] Unfortunately, many of these systems displayed limited or narrow substrate scope.

Moreover, none of the reports described mechanistic studies that may lead to a rational catalyst design for future Ullmann condensation catalysts.

Since the original work of Ullmann and Goldberg, several mechanistic investigations have been performed on homogeneous systems in order to identify the actual catalytic copper species and reaction pathway.[14] On the basis of systematic investigations, up to four different pathways have been proposed to be involved in copper-catalzyed Ullman-type condensation reactions. Interestingly, the three stable oxidation states of copper, namely Cu(I), Cu(II), and Cu(III) have been proposed.[12,24-26] In some proposed mechanisms, the oxidation state of the copper ion changes throughout the catalytic cycle; whereas in other proposals, the oxidation state remains the same.[14] It is very likely, that akin to many other catalytic systems, the reaction mechanism, including the presence or absence of changes in oxidation states, depends on the reaction conditions as well as the catalyst.

Due to their intrinsic structural features, mesoporous nanostructured materials have been recognized as popular heterogeneous catalytic systems[27,28]. They are ideal for providing a high surface area scaffold to which active metals can be tethered. Further, tunable pore size offers good flexibility for the transportation of organic moieties. Mesoporous manganese oxide materials prepared by inverse-micelle templated self-assembly method showed excellent performance in aerobic oxidation of alcohols to aldehydes, amines to imines, anilines to azo compounds, tandem oxidative reactions from alcohols and oxidative coupling of alkynes to diyne derivatives.[29-32] Herein, we describe the application of our recently disclosed mesoporous copper supported manganese oxide material (meso Cu/MnO_x) as a catalyst for Ullmann-type cross-coupling reactions. High

turnover numbers, excellent reusability, avoidance of ligand additives and diversity of the coupling reactions are the notable features of our catalytic protocol. The mechanistic pathways, electronic and steric effects and kinetic analysis were studied in detail. In addition, we provided the energy profile of the reaction by drawing intermediates on the copper oxide surface by DFT calculations and a qualitative description of the mechanism, which supports the experimental findings.

3.3 Experimental Section

3.3.1 Synthesis of mesoporous copper manganese oxide (meso Cu/MnO_x)

The synthesis was performed following the synthesis procedure of inverse micelle templated University of Connecticut (UCT) mesoporous materials.[31] Copper nitrate ($Cu(NO_3)_2.3H_2O$) was selected as the dopant source in the synthesis. In a 120 mL beaker, 0.02 mol of $Mn(NO_3)_2.6H_2O$, 0.002 mol of $Cu(NO_3)_2.3H_2O$ and (0.134 mol) 1-butanol were added. To this solution (0.0034 mol) P123 ($PEO_{20}PPO_{70}PEO_{20}$, molar mass 5750 g mol^{-1}) and (0.032 mol) conc. HNO_3 were added and stirred at room temperature until the solution became clear. The resulting clear blue solution was then kept in an oven at 120°C for 3 h under air. The black material was washed with excess ethanol, centrifuged, and dried in a vacuum oven overnight. The dried black powder was then subjected to a heat treatment of 150°C for 12 h, cooled to room temperature and followed by 250°C for 3 h under air.

3.3.2 Catalyst Characterization

The powder X-Ray diffraction (PXRD) data was collected by a Rigaku Ultima IV diffractometer (Cu Kα radiation, λ=1.5406 Å) with an operating voltage of 40 kV and a

current of 44 mA. The low-angle PXRD patterns were collected over a 2 *theta* range of 0.5–10° with a continuous scan rate of 0.5° min^{-1}, where the wide-angle PXRD patterns were collected over a 2 *theta* range of 5–75° with a continuous scan rate of 1.0° min^{-1}. The nitrogen adsorption desorption experiments were performed by a Quantachrome Autosorb-1-1C automated adsorption system. The samples were treated at 150°C for 6 h under helium prior to measurement. The surface areas and pore sizes (from the desorption branch of isotherm) were measured by the Brunauer–Emmett–Teller (BET) and the Barrett–Joyner–Halenda (BJH) methods. The samples were prepared by casting the suspension of material on a carbon coated copper grid. The surface morphology was determined by a Zeiss DSM 982 Gemini field emission scanning electron microscope (SEM) with a Schottky emitter at an accelerating voltage of 2.0 kV having a beam current of 1.0 mA. The X-ray photoelectron spectroscopy (XPS) were performed by a PHI model 590 spectrometer with multiprobes (ΦPhysical Electronics Industries Inc.), using Al-K radiation (λ= 1486.6 eV) as the radiation source. The curves were fitted using CasaXPS software (version 2.3.12). The powder samples were pressed on carbon tape mounted on adhesive copper tape stuck to a sample stage placed in the analysis chamber. For correction of surface charging, the C 1s photoelectron line at 284.6 eV was taken as a reference. A mixture of Gaussian (70%) and Lorentzian (30%) functions was used for the least-squares curve fitting procedure.

3.3.3 Catalytic Activity Measurements

In a typical reaction, phenol (1.0 mmol), iodobenzene (0.8 mmol), meso Cu/MnO_x (3 mol %), K_2CO_3 (1.5 mmol) and DMF (5 mL) were put in a 25 mL round bottom flask

(two necked flask for time dependent study, where the second neck was used as sample port). The flask with the reaction mixture and a reflux condenser was immersed in a silicon oil bath preheated to 140°C. The reaction mixture was refluxed under vigorous stirring (700 rpm) for the required time under air. After reaction, the mixture was cooled, the catalyst was removed by filtration, and GC-MS (gas chromatography-mass spectrometry) was used to analyze the filtrate. The conversions were determined based on concentration of phenol. The analyses were performed by a 7820A GC system connected with a thermal conductivity detector of 5975 series MSD from Agilent Technologies and a nonpolar cross-linked methyl siloxane column with dimensions of 12 in × 0.200 mm × 0.33 μm.

3.3.4 Computational Methods

Density functional theory (DFT) as implemented in the Vienna *Ab initio* Simulation Package (VASP).[33] The projector augmented-wave (PAW)[34] formalism with Perdew-Burke-Ernzerhof (PBE) exchange-correlation.[35] The basis set includes all the plane waves with kinetic energies up to 450 eV. Monkhorst-Pack grid of 2x2x1 is used for **k**-points sampling.[36] The model system is constructed with a C_6H_5-O and a C_6H_5-I molecules near the CuO surface. The reaction pathway is assumed as follows: First, Both the C_6H_5-O and C_6H_5-I molecules are freestanding with the distance from the CuO surface which is far enough to avoid the interaction between surface and molecules. In step 2, the C_6H_5-I approaches to the surface at first, followed by C_6H_5-O becoming closer (Step 3). Then oxidative addition and nucleophilic addition steps occur (Step 4), and finally the product C_6H_5-O-C_6H_5 forms by reductive elimination.

3.4 Structural characterization of Meso Cu/MnO_x

Figure 3.1 displays the low angle (0.5° - 8°) region of PXRD pattern of meso Cu/MnO_x, which is a typical characterization of UCT materials indicating the size of building blocks (nanoparticles). The wide angle (5° - 75°) diffraction patterns reveal peaks corresponding to copper(II) oxide. However no diffraction peaks corresponding to manganese oxide were observed, which signifies the poorly crystalline nature of manganese oxide at this calcination temperature (250°C).[31] The mesoporous structure was confirmed by nitrogen adsorption–desorption experiments, where a Type-IV adsorption isotherm followed by a Type–I hysteresis loop was observed (**Figure 3.1C**). The material possessed a high surface area of 270 m^2g^{-1} (calculated by BET method). The BJH desorption pore size distribution (**Figure 3.1D**) indicated a narrow monomodal pore size distribution. The pore diameter (3.4 nm) is within the mesoporous range. An aggregation of nanoparticles with spherical morphology was observed by SEM images (**Figure 3.2**). The TEM-EDX map analysis indicated a homogenous distribution of Cu, Mn and oxygen throughout the material, as mentioned in our previous study.[31] The oxidation states of Cu and Mn and chemical nature of oxygen species of the material were verified by XPS. A Cu $2p_{3/2}$ binding energy of 933.3 eV and presence of shake up satellite peaks confirmed the oxidation state of Cu as 2+.The Mn 2p XPS spectra consist of two peaks, which were assigned as Mn $2p_{3/2}$ and Mn $2p_{1/2}$ core levels. The binding energy of 641.5 eV and 653.2 eV can be attributed to Mn^{3+} oxidation state.[37]

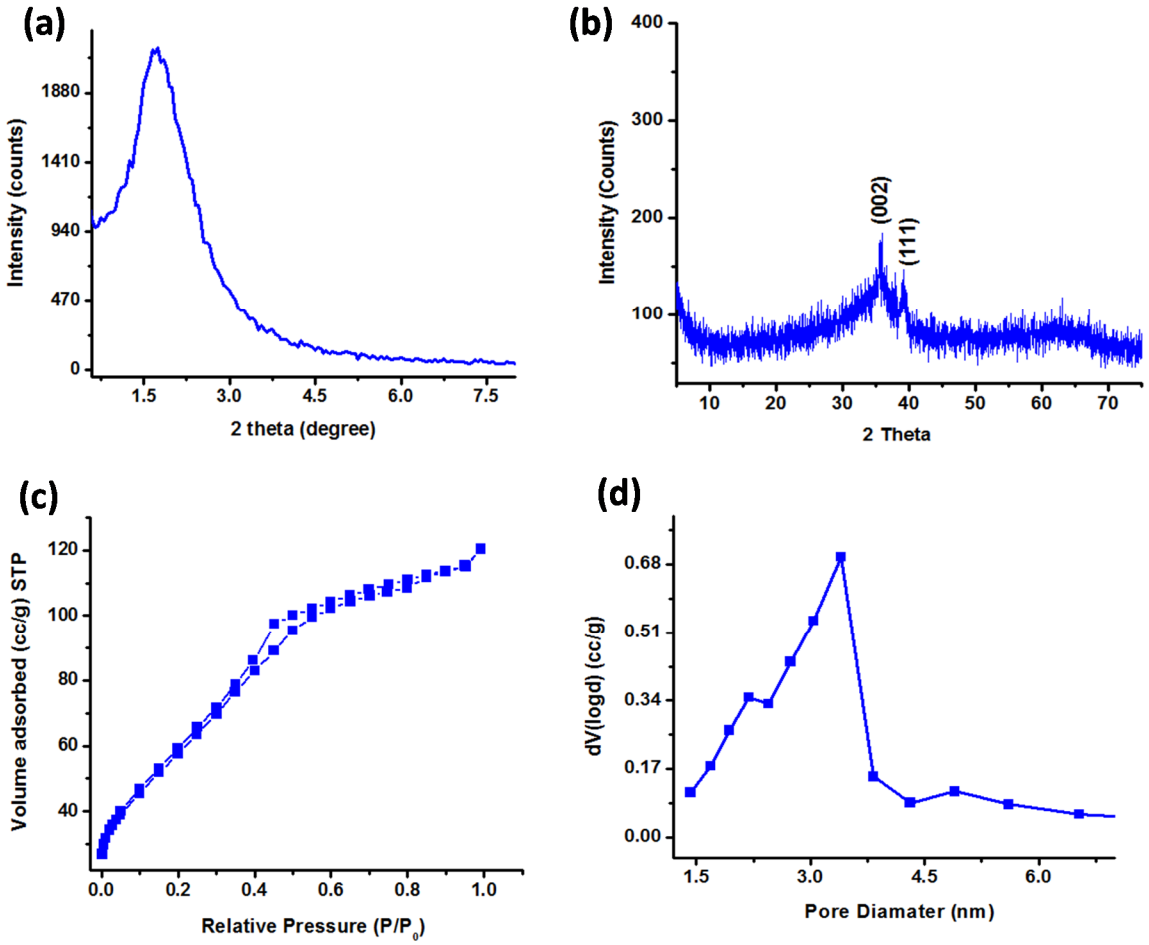

Figure 3.1 Structural characterization of meso Cu/MnO_x. PXRD patterns (A) Low angle (0.5° - 8°), (B) Wide angle (5°-75°), (C) N_2 sorption isotherm and (D) BJH desorption pore size distribution. The pore diameter was calculated as 3.4 nm.

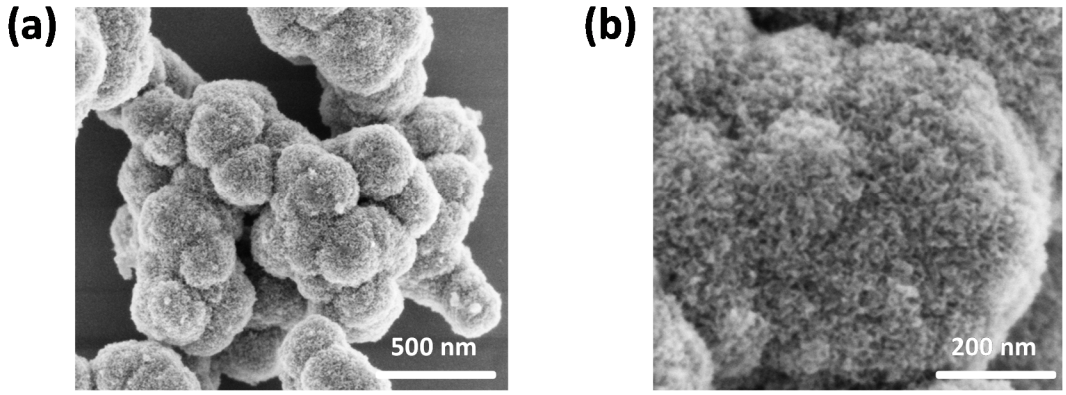

Figure 3.2 SEM images of meso Cu/MnO_x at (a) low and (b) high magnifications.

3.5 Catalytic reaction

3.5.1 Optimization of reaction condition

Table 3.1 Optimization of cross-coupling of phenol and iodobenzene[a]

Entry	Solvent	Temp. (°C)	Base	Molar Ratio	Conv.[b] (%)	Sel.[b] (%)	TON[c]
1	Acetonitrile	80	K_2CO_3	1/0.8	0	0	0
2	1,4-Dioxane	100	K_2CO_3	1/0.8	0	0	0
3	Toluene	110	K_2CO_3	1/0.8	0	0	0
4	DMF	140	K_2CO_3	1/0.8	52	100	17
5[d]	DMF	140	K_2CO_3	1/0.8	3	100	2
6[e]	DMF	140	K_2CO_3	1/0.8	37	100	6
7	DMF	140	K_2CO_3	1/1	30	100	10
8	DMF	140	K_2CO_3	1/1.2	20	100	6.7
9	DMF	140	no	1/0.8	0	0	0
10	DMF	140	KOH	1/0.8	0	0	0

[a] Reaction conditions: Phenol (1.0 mmol), iodobenzene (0.8 mmol), meso Cu/MnO_x (50 mg), solvent (5 mL), base (1.5 mmol), 6 h. [b] Conversions and selectivity were determined by GC-MS based on concentration of phenol. [c] TON = moles of amine converted per mole of catalyst. [d] 25 mg catalyst. [e] 100 mg catalyst.

In order to investigate optimum reaction condition, aryl ether formation from phenol and iodobenzene was selected as a model reaction. First, the reaction was carried out in solvents having various polarities and boiling points (**Entry 1-4, table 3.1**). N,N-dimethyl formamide (DMF), which has substantial polarity and highest boiling point (153°C) emerged as the most suitable one (**Entry 4, table 3.1**). Variation of conversion of phenol with catalyst loading was established for meso Cu/MnO_x (**Entry 4-6, table 3.1**). It is worth to mention here that no ether formation was observed without any

catalyst or using bare meso MnO_x, which signified that copper, is the active site for the present cross-coupling reaction. A much lower conversion (3 %) was achieved at very low copper loading (1.5 mol% Cu), whereas conversion decreased (37 %) significantly at higher copper loading (6 mol% Cu). The higher adsorption of reactant or product may be the reason behind lower activity at higher catalyst amount (**Entry 6, table 3.1**). The copper loading of 3 mol% was found to be the optimum in terms of conversion (52%) and turnover numbers (**Entry 4, table 3.1**). Furthermore, relative molar ratios of phenol to iodobenzene were tuned (**Entry 4, 7 and 8, table 3.1**) to conclude that best percent conversion was achieved with a molar ratio of 1/0.8 among phenol and iodobenzene. Presence of base was necessary (**Entry 9, table 3.1**) for activation of phenol and K_2CO_3 solved the purpose. KOH (**Entry 10, table 3.1**) did not work probably because of poor solubility in the solvent.

3.5.2 Synthetic scope

Having determined the correct combination of solvent, base and temperature to obtain high TON for aryl ether synthesis, we aimed to explore the behavior of meso Cu/MnO_x system to diverse C-O, C-N, C-S substrates. First, derivatives of phenol were reacted (**Entries 1-8**, **table 3.2**) with iodobenzene to evaluate the synthetic scope of diaryl-ether formation. Phenols bearing electron donating (**Entries 2-5**, **table 3.2**) and electron withdrawing group (**Entries 6**, **table 3.2**) reacted with iodobenzene to form the corresponding diaryl-ether with excellent conversion (90 - >99%) and selectivity (mostly >99%). Phenols having electron donating groups (**Entry 2 and 4**, **table 3.2**) reacted much faster compared to phenols having electron withdrawing groups (**Entry 6, table 3.2**). In case of 4-methyl phenol, a small amount of oxidative products of the methyl

group were observed (**Entry 2**, **table 3.2**). Position of substituent displayed significant difference in activity (**Entry 4 and 5**, **table 3.2**), which signifies the effect of electronic nature of the substituent in the reaction rate. No dehalogenated product was detected in case of phenols with chloro substitution (**Entry 6, Table 3.2**). The catalyst was also useful for reaction with relatively bulky phenolic (1-napthol) system (**Entry 7, Table 3.2**). A heterocyclic compounds can also be effectively coupled with the iodobenzene with the present protocol (**Entry 8, Table 3.2**).

The catalyst also exhibited high conversions and selectivity when structurally different iodobenzenes were selected as substrates (**Entry 9-11, Table 3.2**). In contrast to phenols, in presence of iodobenzenes bearing electron donating groups (**Entry 9 and 10, Table 3.2**), much less conversion were achieved even after longer reaction time (20 h). Whereas, a nitro substituted (electron withdrawing) iodobenzene gave quantitative conversion in an hour of reaction (**Entry 11, Table 3.2**). Bromobenzene as substrate also produced the corresponding diaryl ether with excellent conversion (90%) and selectivity (>99%) (**Entry 12, Table 3.2**). However, the reaction was totally inactive in case of chlorobenzene as the halogen substituted benzenes (**Entry 13, Table 3.2**).

To expand the scope of our methodology, we also performed cross-coupling between aniline, imidazole, amide and thiophenol with iodobenzene for the respective N and S coupled products. A very low conversion (5%) was achieved for aniline (**Entry 14, Table 3.2**), whereas imidazole and amide gave moderate conversion (45 – 60 %) but excellent selectivity (>99%) (**Entry 15 and 16, Table 3.2**). On the other hand, reaction between thiophenol and iodobenzene resulted in very high conversion (>99%) but much

lower selectivity (70%). The other product was disulfide, which was formed by oxidation of thiophenol (**Entry 17, Table 3.2**).

Table 3.2 Ullmann cross-coupling reactions by meso Cu/MnOx[a]

Entry	Nucleophiles	Aryl-halides	Time (h)	Conv.[b] (%)	Selec.[c] (%)	TON
1	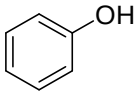	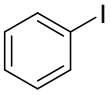	20	92	>99	30.7
2[d]	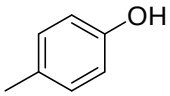	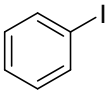	6	97	90[e]	32.3
3	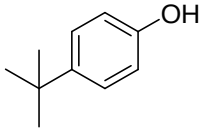	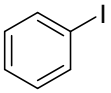	20	90	>99	30.0
4	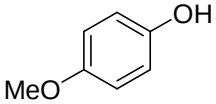	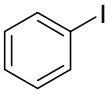	3	>99	>99	33.3
5	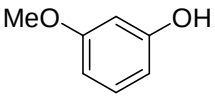	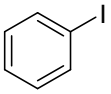	20	97	>99	32.3
6	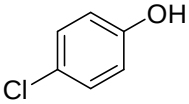	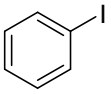	20	93	>99	31.0
7	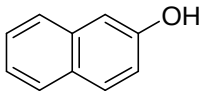	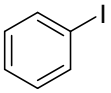	20	92	>99	30.7
8	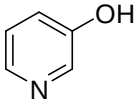	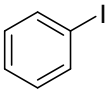	20	93	>99	31.0
9	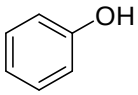	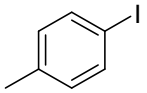	20	80	>99	26.7
10	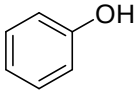	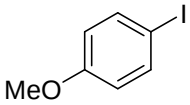	20	75	>99	25.0
11	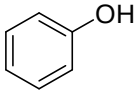	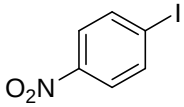	1	>99	>99	33.3
12	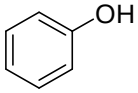	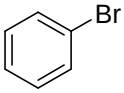	20	90	>99	30.0
13	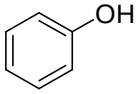	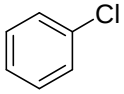	20	0	nd	0

14	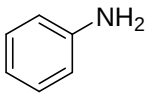	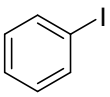	20	5	90	1.67
15	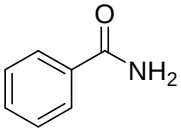	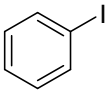	20	45	>99	15.0
16	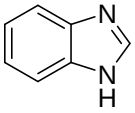	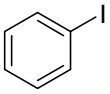	20	65	>99	21.7
17[d]	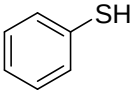	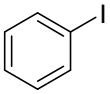	20	>99	70[f]	33.3

Reaction Conditions: phenol (1.0 mmol), iodobenzenes (0.8 mmol), DMF (5 mL), catalyst (50 mg), 130°C. [b] Conversion was determined based on phenol. [c] Determined by GC-MS. [d] Under nitrogen atmosphere. [e] Other products due to oxidation of methyl group. [f] Disulfide is also formed in this reaction.

3.5.3 Heterogeneity and Reusability

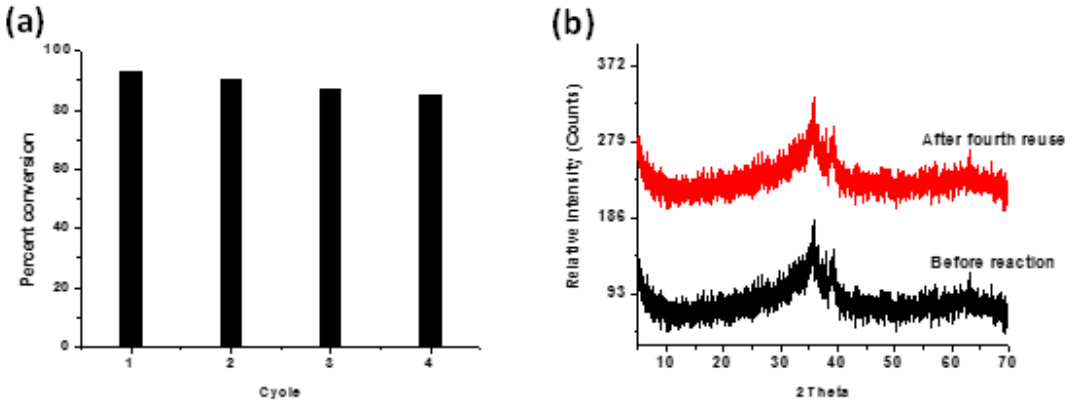

Figure 3.3 (a) The reusability experiment. Reaction Conditions: 4-methoxyphenol (1.0 mmol), 4-nitroiodine (0.8 mmol), catalyst (6 mol% Cu), DMF (5 mL), 140°C, 45 min. (b) PXRD before and after fourth reuse. The diffraction patterns without noticeable change were observed after fourth reuse.

Steady reusability and negligible leaching of active species are two important factors for an efficient heterogeneous catalytic system. We selected cross-condensation of 4-methoxyphenol and 4-nitroiodobenzene as the model reaction for a reusability study. After the reaction, the catalyst was retrieved by filtration and was washed with excess solvent, water and ethanol (>90% recovery). Prior to reuse the catalyst was reactivated at

250°C for 30 min to remove any adsorbed organic species. **Figure 3.3a** shows that the catalyst can retain activity and selectivity even after fourth reuse. Moreover, no change in the PXRD pattern after the fourth cycle was observed (**Figure 3.3b**), which confirms that the catalyst can retain the crystal structure even after multiple reuse cycles. The hot filtration test was also carried out to verify any possible leaching of active species from the catalyst surface. No further formation of diaryl ether took place after filtering off the catalyst at 35% conversion (**Figure 3.4**). These results indicate that the active catalyst truly has a heterogeneous nature, and highlight the sustainability of the system as meso Cu/MnO_x can be recycled.

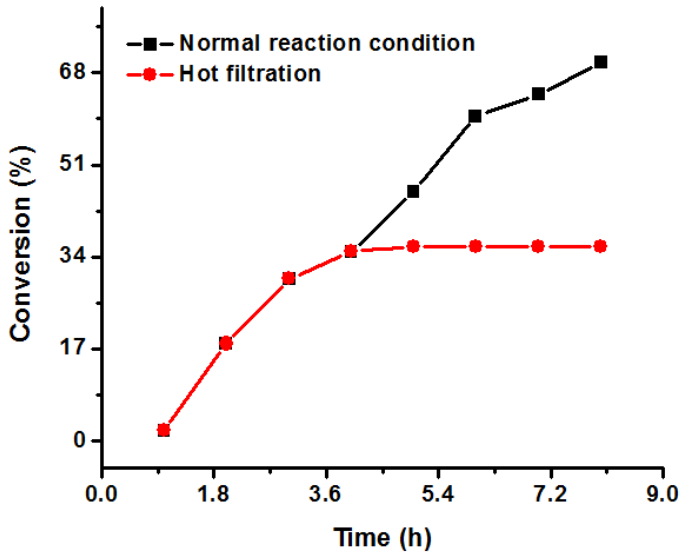

Figure 3.4 Test of heterogeneity. Catalyst was removed after 35% conversion, no change of conversion was observed thereafter. Reaction Conditions: Phenol (1.0 mmol), Iodobenzene (0.8 mmol), catalyst (3 mol% Cu), DMF (5 mL), 140°C.

3.5.4 Kinetic and mechanistic study

At least four different mechanisms have been described for Ullmann-type condensation reactions.[13,38] One of the proposals includes the formation of aryl radical intermediates.[39,40] To test whether radical intermediates formed during the reaction catalyzed by meso Cu/MnO_x, we performed the coupling reaction in the presence of a radical scavenger. Addition of the radical scavenger phenothiazine was found to have no effect on the reaction rate of cross-condensation of phenol and iodobenzene, ruling out the formation of radical intermediates produced by homolytic cleavage of carbon–halogen bond. As observed in table 3.2, a significant difference in the reaction rate was observed due to the nature of the substituents present in iodobenzene. Linear free energy studies are a powerful tool that offers chemists useful mechanistic insight.

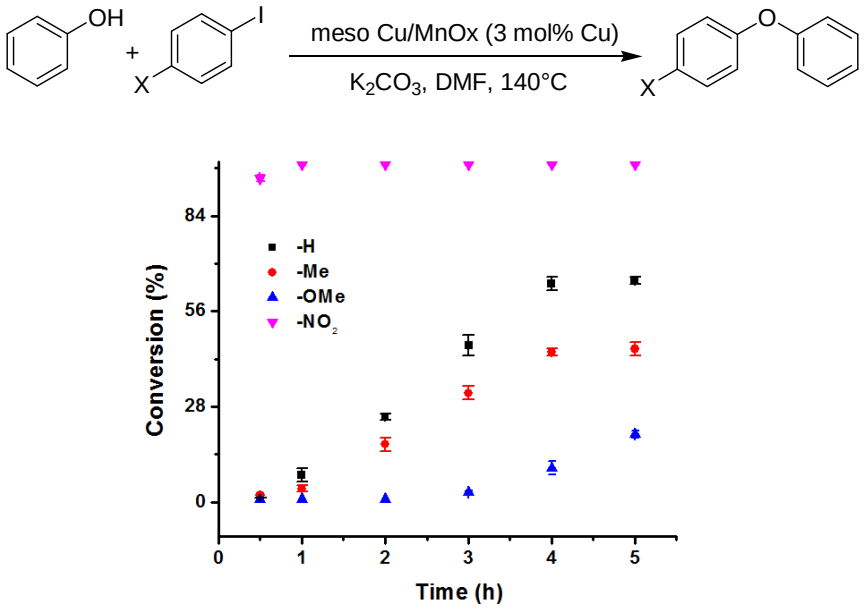

Figure 3.5 Time dependent studies of coupling of *para* substituted phenols and iodobenzene by meso Cu/MnO_x: Reaction condition: Phenol (1.0 mmol), iodobenzene derivatives (0.8 mmol), catalyst (50 mg), base (1.5 mmol), solvent (5 mL), 140°C. Conversions were measured with respect to iodobenzene concentration.

In order to test the effect of electronic changes in the rate of oxidative addition of iodobenzene, we initially performed a series of kinetic experiments with four different *para* substituted (p-NO_2, p-H, p-Me, p-OMe) iodobenzene derivatives (**Figure 3.5**). Continuous sampling was undertaken in the course of few hours and conversion and selectivity were determined by GC-MS. Kinetic experiments depicted a first order rate equation with respect to iodobenzene derivatives. A Hammett-type analysis was used to establish the role of electronic effect of the substituents in the reaction rate.[41] In a Hammett-type analysis, a plot of logarithmic values of relative rate constants against a set of standard σ values is drawn.[41] We plotted logarithmic values of relative rate constants against σ_p^+, the Brown–Okamoto constant (**Figure 3.6**), and against σ^- values (**Figure 3.7**). Better correlation was found with the latter, although both resulted in similar ρ values, 0.92 and 1.0 for σ_p^+ and σ^-, respectively. The positive slope values suggest development of negative charge at the reaction center.

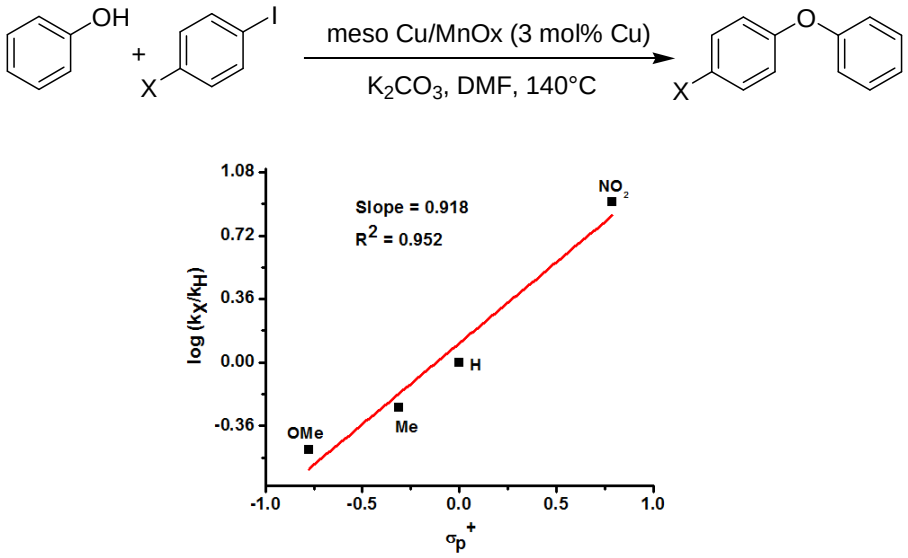

Figure 3.6. Hammett plot of competitive oxidation of para substituted iodobenzenes at 6 h of reaction time.

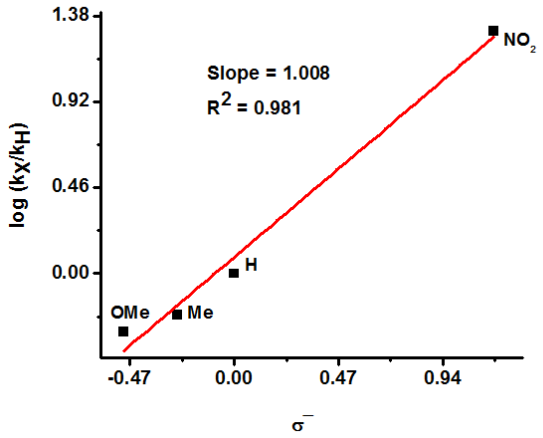

Figure 3.7 Hammett plot for Ullman cross-coupling reactions of para substituted iodobenzenes. Based on σ^-, ρ = 1.0.

Similarly, we performed Hammett analysis to verify the electronic influence of the substituents in the phenol derivatives. The relative rates of coupling of *para* substituted phenols (p-Cl, p-H, p-Me, p-OMe) were investigated. A linear relationship was found between log (k_X/k_H) and σ_p^+ (**Figure 3.8**). The slope of the plot shows a reaction constant ρ value of -2.9 for the phenol derivatives studied, which suggests development of a positive charge at the reaction center in the transition state involving phenol.

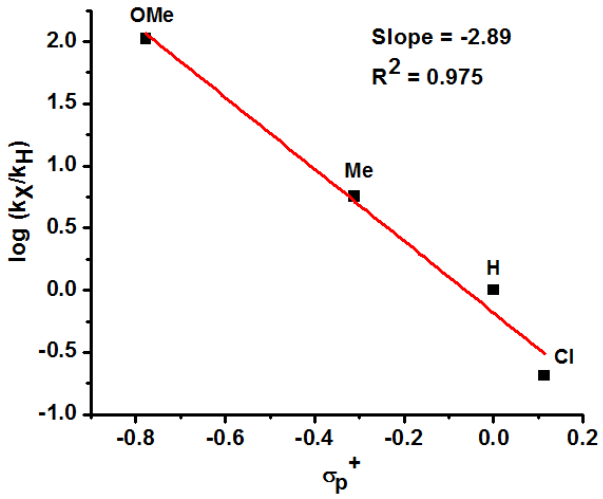

Figure 3.8 Hammett plot for Ullman cross-coupling reactions of para substituted phenols. Based on σ_p^+, ρ = -2.9.

3.5.5 Theoretical investigation

To further validate the energetics during the reaction we performed quantum mechanical computations using density functional theory (DFT). The model system was constructed with a C_6H_5-O and a C_6H_5-I molecules near the CuO surface. Based on our mechanistic studies and the literature the following reaction pathway was assumed: First, Both the C_6H_5-O and C_6H_5-I molecules are freestanding with the distance from the CuO surface which is far enough to avoid the interaction between surface and molecules. In step 2, the C_6H_5-I approaches to the surface at first, followed by C_6H_5-O becoming closer (Step 3). Then oxidative addition and nucleophilic addition steps occur (Step 4), and finally the product C_6H_5-O-C_6H_5 forms by reductive elimination. The energy profile for the reaction is shown in **Figure 3.9** with labeling the relative energy compared to the starting configuration, and visualized structures. As observed, the system gets stabilized as the molecules get closer to the surface. A significant decrease in the system energy

was calculated for step 4 further confirming the oxidative addition to the catalyst. Interestingly, the metal ion is assisted during the oxidative addition by an oxide, with the aryl group on the latter and the iodide in the copper coordination sphere. The higher energy (3.96 kcal mol^{-1} higher) of the final product formation is due to the formation of the final product and release from the surface. Bader analysis based charge,[42] which is associated to the atoms through the reaction, is shown in figure 3.9 with schematic representation of each reaction coordinate. No distinct change of charge on the copper atoms was observed throughout the reaction, highlighting the ability of the surrounding molecules on the surface to assist in the activation of the substrates.

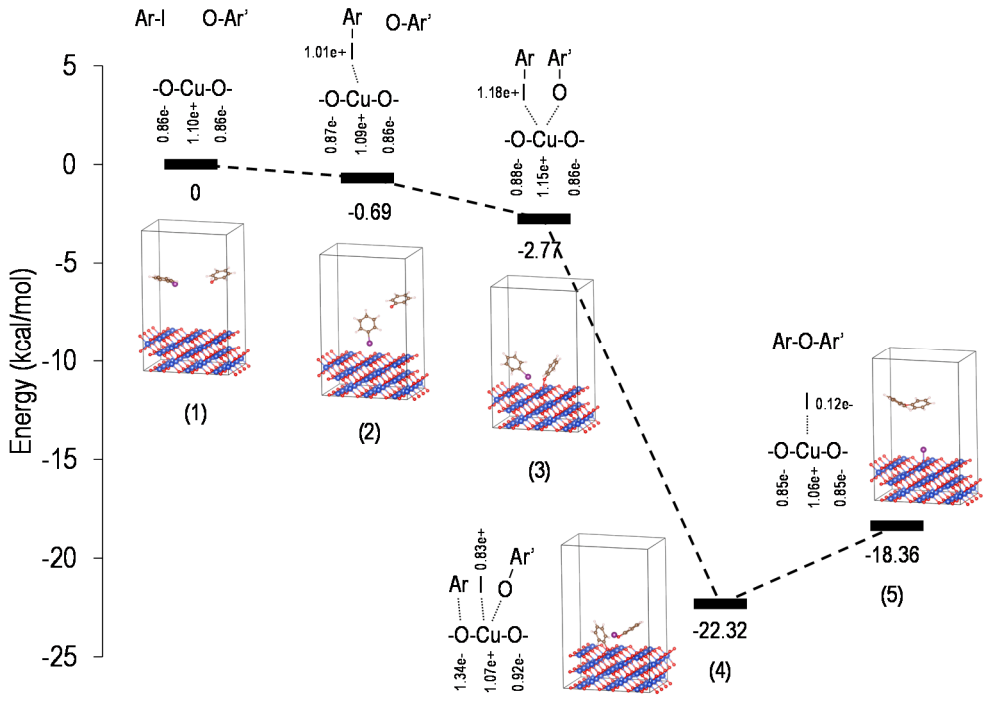

Figure 3.9 Change of the DFT computed energy for the reaction pathway of Ullmann coupling over CuO surface and corresponding change of the charge associated to the atoms directly involved in the reaction.

3.6 Discussion

This study illustrates the use of a mesoporous copper oxide supported on manganese oxide as an efficient heterogeneous catalyst for Ullmann-type condensation reaction. An inverse micelle templated self-assembly procedure has been used to synthesize the material. A nonpolar pluronic surfactant (P123) acts as the scaffold to build the mesostructure. Copper was introduced in the system by addition of a copper salt *in situ* during the sol-gel process. In our previous study, we showed that different amounts of copper can be incorporated in the mesoporous manganese oxide material.[31] We also found that 10 mol% Cu had the maximum activity for the catalyzed coupling of alkynes. Therefore, in this study we focused on the 10 mol% Cu incorporated MnO_x material. PXRD was used to confirm the presence of copper oxide over the manganese oxide. In meso Cu/MnO_x, manganese oxide acts as a support for tethering the active copper oxide nanoparticle while preserving the mesoporous structure as well. Synthesis of bare mesoporous copper oxide was unsuccessful using this procedure.

Our system indicates excellent substrate scope and functional group tolerability for Ullmann ether coupling reactions. Although iodo and bromo substituted phenols reacted very efficiently to furnish the corresponding diaryl ether, the chlorinated counterpart was inert using the same reaction conditions. Steric effects in the reaction were evaluated by using the sterically hindered phenol (2,4,6-tri-*tert*-butylphenol) as one of the coupling reagents. No ether formation occurred indicating that sterics play a role in the Ullman cross-coupling catalyzed by meso Cu/MnO_x. Meso Cu/MnO_x can also be applied to cross-coupling of aniline, imidazole, amide and thiophenol derivatives for construction of C-N and C-S bonds. Substrates bearing hetero atoms like S or N are

known to poison transition metal oxide based catalysts due to strong coordination of the heteroatom to the transition metal centers.[43] We observed decrease activity with N-containing substrates as compared to phenol, e.g. aniline, imidazole and amide reactions. However, 3-pyridinemethanol was coupled efficiently to the corresponding aryl ether with no significant drop of TON and selectivity compared to the phenol indicating that meso Cu/MnO_x is less susceptible to poisoning than other metal oxide based catalysts. Interestingly, thiophenol displayed much higher activity (>99% conversion). In the case of thiophenol, the selectivity to the diaryl ether was lower due to formation of the disulfide as manganese oxide is known to oxidize thiol to disulfide.[44]

Despite the progress towards designing proper heterogeneous copper based catalysts for Ullmann type cross-coupling reactions under ligand free condition, many features of the mechanistic insights still remain poorly understood. Generally, the most accepted reaction mechanism involves oxidative addition of the haloarene to the Cu(I) center to generate an aryl-Cu(III)-X intermediate followed by nucleophilic reaction and reductive elimination to yield the desired product. Very few studies have shown isolation of the intermediates in copper catalyzed Ullmann coupling reactions.[25,45] The works of Buchwald and Hartwig provided evidence of formation of Cu(I) complex with nitrogen donor ligands.[25,26] However, no evidence of Cu(III)-aryl complex formation was observed, since the reductive elimination from Cu(III) intermediate is much more rapid than oxidative addition of Cu(I) center. In studies by Stahl and coworkers, Cu(I)/Cu(III) redox steps have been observed, where a macrocyclic ligand has been used to stabilize the Cu(III) species.[46] Cu(II) salts have also been used as catalysts for the Ullmann reaction, although in these cases it has been hypothesized that reduction to a Cu(I)

species happens with the concomitant oxidation of phenoxide or amines present in the reaction mixture.[11,12] Our Hammett analysis shows that electron deficient *para*-susbtituted aryl iodides facilitate more rapid turnover rates. The positive sign of the ρ value indicates the buildup of negative charge in the transition state involving iodobenzene. We obtained a better correlation against σ^- as compared to σ_p^+. Similar behavior, that is better correlation with σ^- over σ_p^+, has been observed in oxidative addition reactions.[47] Thus, an oxidative addition step is likely to be present during the Ullmann ether coupling catalyzed by meso Cu/MnO_x. It must be noted that the oxidative addition of aryl iodides to Pd(0) and Ni(0) complexes show ρ = 2.7 and 2.0, respectively ,[48,49] whereas a smaller value, ρ = 0.9, has been reported for the oxidative addition of aryl iodides to Rh(I) complex containing a diarylamido/bis(phosphine) pincer ligand (**Table 3.3**).[47] Based on these values, the meso Cu/MnO_x – aryl iodide transition state resembles more that of the less nucleophilic Rh(I)-diarylamido/bis(phosphine) complex than that of the Pd(0) and Ni(0) species.

Table 3.3 Comparison of ρ values

Catalyst system	Oxidative addition species	Rho value	Reference
$Ni^0(PEt_3)_4$	Ar-I	2.0	*J. Am. Chem. Soc.* **1979**, *101*, 6319-6332.
$Pd^0(PPh_3)_4$	Ar-I	2.7	*J. Am. Chem. Soc.* **1991**, *113*, 8375-8384.
$Pd^0(PPh_3)_4$	Ar-OTf	2.5	*Organometallics* **1995**, *14*, 1810-1817.
Rh(PNP)	Ar-I	0.9	*Organometallics* **2011**, *30*, 2472-2482.
$Ta(silox)_3$	C-N	2.1	*J. Am. Chem. Soc.* **1996**, *118*, 5132-5133.
Meso Cu/MnO_x	Ar-I	1.0	This work

In addition, we observed faster reaction rates in the presence of electron donating groups on the phenol ring. The negative ρ value also indicates the development of positively charged species in the transition state. The magnitude of ρ indicates that a phenoxy radical species is not formed as the formation of radicals usually lead to small ρ values.[41] The addition of radical inhibitor had no effect in the reaction rate and no biphenyl was produced reinforcing the idea that no radicals formed during the reaction. The development of a positive charge is probable due to the coordination of phenol or phenoxide anion to the copper center.

Based on our observations, we propose a mechanism for the coupling reaction catalyzed by meso Cu/MnO_x. First, catalytically active Cu(I) center is generated from the Cu(II) species by reaction with phenolate ion (formed by base). The reduction of Cu(II) to Cu(I) is well-known in presence of alkoxide, where a β-H elimination from a Cu(II)-alkoxide species followed by subsequent deprotonation has been observed.[50] The iodobenzene molecule undergoes oxidative addition to the Cu(I) oxide on the surface resulting in the formation of Cu-I and O-aryl bonds. The oxidative addition is followed by nucleophilic addition of phenoxide ion. Finally a reductive elimination produces the desired biaryl product. The typical oxidation state changes that occurred on the copper center, e.g. Cu(I)/Cu(III) cycling, in molecular systems during the Ullman cross-coupling reaction is avoided with this catalyst because of the delocalization of the charge on the Cu/MnO_x surface. Whether the oxidative addition of aryl halide or coordination of the nucleophiles (-O, -N or -S) happens first is a question that remains to be answered. Mechanistic studies by Buchwald and Hartwig showed formation of the Cu(I)-nucleophile bond prior to oxidative addition.[25,26] On the other hand, works of Monnier

and Stahl confirmed that oxidative addition preceded the nucleophilic addition in some systems.[46,51] The nature of the nucleophiles and ligands along with reaction conditions largely influence the mechanism of Ullmann coupling reaction.

3.7 Conclusion

In summary, we report the use of the thermally stable and reusable mesoporous copper-supported manganese oxide material as a catalyst for Ullman cross-coupling reaction. We demonstrate broad substrate scope and excellent functional group tolerability in C-O, C-N and C-S bond formation reactions. The catalytic protocol circumvents the use of additional ligands. The catalyst was reusable without any significant loss of activity after four cycles. Our experimental and computational work provided evidence for oxidative addition of the aryl iodide substrate assisted by the O atoms on the surface of the catalyst. Similarly to oxidative additions on single metal centers, rate acceleration in the presence of electron withdrawing groups on the aryl halide ring is observed. The Hammett analysis indicates that the Cu-O moiety in which the aryl iodide is added acts more like a Rh(I) species than a Ni(0) or Pd(0) intermediate. Future work will focus on using experimental and computational studies to understand the oxidative addition of aryl iodides to Cu/MnO_x and elucidate the full mechanism of cross-coupling.

3.8 References

(1) Cristau, H.-J.; Cellier, P. P.; Hamada, S.; Spindler, J.-F.; Taillefer, M. *Organic Letters* **2004**, *6*, 913-916.

(2) Salih, M. Q.; Beaudry, C. M. *Organic Letters* **2013**, *15*, 4540-4543.

(3) Haumesser, J.; Pereira, A. M. V. M.; Gisselbrecht, J.-P.; Merahi, K.; Choua, S.; Weiss, J.; Cavaleiro, J. A. S.; Ruppert, R. *Organic Letters* **2013**, *15*, 6282-6285.

(4) Hwang, J. Y.; Kawasuji, T.; Lowes, D. J.; Clark, J. A.; Connelly, M. C.; Zhu, F.; Guiguemde, W. A.; Sigal, M. S.; Wilson, E. B.; DeRisi, J. L.; Guy, R. K. *Journal of Medicinal Chemistry* **2011**, *54*, 7084-7093.

(5) Devambatla, R. K. V.; Namjoshi, O. A.; Choudhary, S.; Hamel, E.; Shaffer, C. V.; Rohena, C. C.; Mooberry, S. L.; Gangjee, A. *Journal of Medicinal Chemistry* **2016**, *59*, 5752-5765.

(6) Yang, D.; Fu, H. *Chem. Eur. J.* **2010**, *16*, 2366-2370.

(7) Jammi, S.; Sakthivel, S.; Rout, L.; Mukherjee, T.; Mandal, S.; Mitra, R.; Saha, P.; Punniyamurthy, T. *J. Org. Chem.* **2009**, *74*, 1971-1976.

(8) Benyahya, S.; Monnier, F.; Taillefer, M.; Man, M. W. C.; Bied, C.; Ouazzani, F. *Adv. Synth. Catal.* **2008**, *350*, 2205-2208.

(9) Evano, G.; Blanchard, N.; Toumi, M. *Chem. Rev.* **2008**, *108*, 3054-3131.

(10) Ullmann, F.; Bielecki, J. *Berichte der deutschen chemischen Gesellschaft* **1901**, *34*, 2174-2185.

(11) Weingarten, H. *The Journal of organic chemistry* **1964**, *29*, 3624-3626.

(12) Paine, A. J. *J. Am. Chem. Soc.* **1987**, *109*, 1496-1502.

(13) Sperotto, E.; van Klink, G. P. M.; van Koten, G.; de Vries, J. G. *Dalton Transactions* **2010**, *39*, 10338-10351.

(14) Sambiagio, C.; Marsden, S. P.; Blacker, A. J.; McGowan, P. C. *Chem. Soc. Rev.* **2014**, *43*, 3525-3550.

(15) Sheldon, R.; Downing, R. *Appl. Catal., A: Gen.* **1999**, *189*, 163-183.

(16) Lipshutz, B. H.; Unger, J. B.; Taft, B. R. *Org. Lett.* **2007**, *9*, 1089-1092.

(17) Jiao, J.; Zhang, X.-R.; Chang, N.-H.; Wang, J.; Wei, J.-F.; Shi, X.-Y.; Chen, Z.-G. *J. Org. Chem.* **2011**, *76*, 1180-1183.

(18) Mulla, S. A.; Inamdar, S. M.; Pathan, M. Y.; Chavan, S. S. *Tetrahedron Lett.* **2012**, *53*, 1826-1829.

(19) Zhang, P.; Yuan, J.; Li, H.; Liu, X.; Xu, X.; Antonietti, M.; Wang, Y. *RSC Advances* **2013**, *3*, 1890-1895.

(20) Jadhav, V. H.; Dumbre, D. K.; Phapale, V. B.; Borate, H. B.; Wakharkar, R. D. *Catal. Commn.* **2007**, *8*, 65-68.

(21) Shelke, S. N.; Bankar, S. R.; Mhaske, G. R.; Kadam, S. S.; Murade, D. K.; Bhorkade, S. B.; Rathi, A. K.; Bundaleski, N.; Teodoro, O. M.; Zboril, R. *ACS Sustainable Chemistry & Engineering* **2014**, *2*, 1699-1706.

(22) Ling, P.; Li, D.; Wang, X. . *Mol. Catal. A: Chem.* **2012**, *357*, 112-116.

(23) Wang, M.; Yuan, B.; Ma, T.; Jiang, H.; Li, Y. *RSC Advances* **2012**, *2*, 5528-5530.

(24) Weingarten, H. *J. Org. Chem.* **1964**, *29*, 3624-3626.

(25) Tye, J. W.; Weng, Z.; Johns, A. M.; Incarvito, C. D.; Hartwig, J. F. *J. Am. Chem. Soc.* **2008**, *130*, 9971-9983.

(26) Strieter, E. R.; Bhayana, B.; Buchwald, S. L. *J. Am. Chem. Soc.* **2008**, *131*, 78-88.

(27) Taguchi, A.; Schüth, F. *Microporous Mesoporous Mater.* **2005**, *77*, 1-45.

(28) Perego, C.; Millini, R. *Chem. Soc. Rev.* **2013**, *42*, 3956-3976.

(29) Biswas, S.; Dutta, B.; Mullick, K.; Kuo, C.-H.; Poyraz, A. S.; Suib, S. L. *ACS Catal.* **2015**, *5*, 4394-4403.

(30) Biswas, S.; Poyraz, A. S.; Meng, Y.; Kuo, C.-H.; Guild, C.; Tripp, H.; Suib, S. L. *Appl. Catal., B: Environ.* **2015**, *165*, 731-741.

(31) Biswas, S.; Mullick, K.; Chen, S.-Y.; Kriz, D. A.; Shakil, M.; Kuo, C.-H.; Angeles-Boza, A. M.; Rossi, A. R.; Suib, S. L. *ACS Catal.* **2016**, *6*, 5069-5080.

(32) Dutta, B.; Biswas, S.; Sharma, V.; Savage, N. O.; Alpay, S.; Suib, S. L. *Angew. Chem.* **2016**, *128*, 2211-2215.

(33) Kresse, G.; Hafner, J. *Physical Review B* **1993**, *47*, 558.

(34) Blöchl, P. E. *Physical Review B* **1994**, *50*, 17953.

(35) Perdew, J. P.; Burke, K.; Ernzerhof, M. *Physical review letters* **1996**, *77*, 3865.

(36) Monkhorst, H. J.; Pack, J. D. *Physical review B* **1976**, *13*, 5188.

(37) Genuino, H. C.; Dharmarathna, S.; Njagi, E. C.; Mei, M. C.; Suib, S. L. *J. Phys. Chem. C* **2012**, *116*, 12066-12078.

(38) Jones, G. O.; Liu, P.; Houk, K. N.; Buchwald, S. L. *Journal of the American Chemical Society* **2010**, *132*, 6205-6213.

(39) Bunnett, J. F.; Kim, J. K. *J. Am. Chem. Soc.* **1970**, *92*, 7463-7464.

(40) Creutz, S. E.; Lotito, K. J.; Fu, G. C.; Peters, J. C. *Science* **2012**, *338*, 647-651.

(41) Johnson, C. D. *The Hammett Equation*; Cambridge University Press, 1973.

(42) Henkelman, G.; Arnaldsson, A.; Jónsson, H. *Computational Materials Science* **2006**, *36*, 354-360.

(43) Peral, J.; Ollis, D. F. . *Mol. Catal. A: Chem.* **1997**, *115*, 347-354.

(44) Dharmarathna, S.; King'ondu, C. K.; Pahalagedara, L.; Kuo, C.-H.; Zhang, Y.; Suib, S. L. *Appl. Catal., B: Environ.* **2014**, *147*, 124-131.

(45) Huffman, L. M.; Stahl, S. S. *J. Am. Chem. Soc.* **2008**, *130*, 9196-9197.

(46) Casitas, A.; King, A. E.; Parella, T.; Costas, M.; Stahl, S. S.; Ribas, X. *Chem. Sci.* **2010**, *1*, 326-330.

(47) Puri, M.; Gatard, S.; Smith, D. A.; Ozerov, O. V. *Organometallics* **2011**, *30*, 2472-2482.

(48) Amatore, C.; Azzabi, M.; Jutand, A. *Journal of the American Chemical Society* **1991**, *113*, 8375-8384.

(49) Tsou, T. T.; Kochi, J. K. *Journal of the American Chemical Society* **1979**, *101*, 6319-6332.

(50) Franc, G.; Jutand, A. *Dalton Transactions* **2010**, *39*, 7873-7875.

(51) Monnier, F.; Taillefer, M. *Angew. Chem., Int. Ed.* **2009**, *48*, 6954-6971.

CHAPTER 4. Heterogeneous Mesoporous Manganese Oxide Catalyst for Aerobic and Additive-Free Oxidative Aromatization of N-Heterocycles

4.1 Abstract

In this chapter, we report a heterogeneous, aerobic, additive free and environmentally benign catalytic protocol for oxidative aromatization of saturated nitrogen-heterocycles using mesoporous manganese oxide material. The mesoporous manganese oxide material was synthesized using inverse surfactant micelle as a soft template. The material presented aggregated nanocrystalline nature with monomodal mesoporous size distribution. A broad substrate scope was observed in our catalytic protocol. The aromatized products can be separated by easy filtration and the catalyst is reusable up to fourth cycle. Surface active Mn^{3+} species along with labile lattice oxygen were found to play an important role in the catalytic activity. Mild reaction conditions (air atmosphere and absence of any oxidative or basic promoters), ease of product separation by simple filtration and significant reusability make this mesoporous manganese oxide material an economical and ecofriendly catalyst for the syntheses of versatile aromatic derivatives.

4.2 Introduction

Nitrogen containing heterocyclic aromatic compounds are common intermediates in pharmaceutical and biologically relevant molecules.[1,2] The typical procedure to access the heteroarenes involve dehydrogenation reaction from the corresponding saturated heterocycles. One process is the acceptor-less dehydrogenation (scheme 4.1a), which has been accomplished with ruthenium, iron and iridium based homogeneous molecular catalysts along with metal-free boron based catalysts.[3-9] The second process utilizes catalytic oxidative dehydrogenation of saturated nitrogen heterocycles under oxygen atmosphere (scheme 4.1b). Several homogeneous catalysts have been successfully employed for this process.[10-14]

From environmental perspective, heterogeneous catalysts are much more efficient in terms of easy product separation and catalyst reusability. Some existing heterogeneous catalysts for oxidative aromatization of N heterocycles are Rh, Pd and Cu based catalysts, Pd_3Pb, Pt nanowires, Au nanoparticles and Ru supported on different metal oxide supports.[15-22] However, most of the systems are based on noble metals and no structure-activity relationship has been performed. Beller and coworkers have reported an efficient heterogeneous iron-nitrogen doped graphene core-shell catalyst in this regard.[23] Broad substrate scope with excellent reusability has been observed for the core-shell catalysts. Another study by Stahl and coworkers utilized a cobalt oxide supported nitrogen doped graphene catalysts for oxidative aromatization at lower temperature.[24] Despite good catalytic performance, these systems required either difficult catalyst preparation methods or use of high oxygen pressure and basic additives. Therefore, a simple and efficient

heterogeneous catalytic system for oxidative aromatization of N-heterocycles under aerobic and atmospheric conditions in highly desirable.

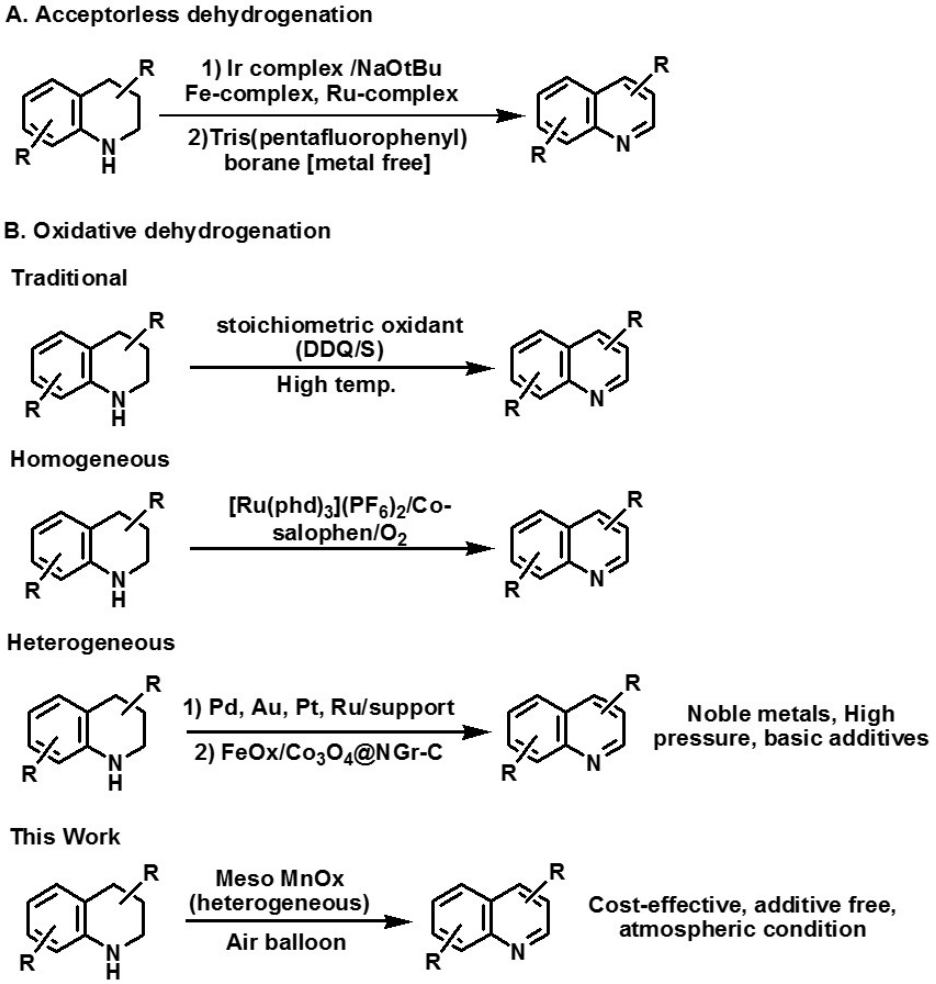

Scheme 4.1 Various routes to synthesize N-heterocyclic aromatic compounds

Mesoporous manganese oxide materials prepared by inverse-micelle templated self-assembly method showed excellent performance in aerobic oxidation of alcohols to aldehydes, amines to imines, anilines to azo compounds, tandem oxidative reactions from alcohols and oxidative coupling of alkynes to diyne derivatives.[25-28] These mix valent manganese oxide materials have versatile structural forms with high thermal stability. The manganese redox cycle and labile lattice oxygen molecules are proved as dominant

factors in the catalytic performance. Herein, we present our effort to utilize the mesoporous manganese oxide materials for aerobic dehydrogenation of saturated N heterocycles to the corresponding aromatic derivatives. Use of inexpensive manganese oxide, air as the terminal oxidant, atmospheric reaction condition and absence of any kind of additives, with proper reusability are the notable features of our catalytic protocol.

4.3 Experimental Section

4.3.1 Synthesis of mesoporous manganese oxide (meso MnO_x)

In a typical synthesis 0.02 mol of manganese nitrate tetrahydrate ($Mn(NO_3)_2 \cdot 4H_2O$) and 0.134 mol of 1-butanol were added into a 120 mL beaker. To this solution 0.00034 mol of poly(ethylene glycol)-block-poly(propylene glycol)-block-poly(ethylene glycol) (Pluoronic P123, $PEO_{20}PPO_{70}PEO_{20}$, molar mass 5750 g mol^{-1}) and 0.032 mol of concentrated nitric acid (HNO_3) were added and stirred at room temperature until the solution became clear (light pink). The resulting clear solution was then kept in an oven at 120°C for 3 h under air. The black product was collected and washed with excess ethanol, centrifuged, and dried in a vacuum oven overnight. At the end, the dried black powders were subjected to a heating cycle. First they were heated at 150°C for 12 h and cooled down to room temperature under ambient conditions followed by a second heating step of 250°C for 4 h. The structural proeties can be tuned by further heat treatment of 350°C for 3 h, 450°C for 2 h and 550°C for 1 h.

4.3.2 Catalyst Characterization

Powder X-Ray diffraction (PXRD) data were collected by a Rigaku Ultima IV diffractometer (Cu Kα radiation, λ=1.5406 Å) with an operating voltage of 40 kV and a current of 44 mA. The PXRD patterns were collected over a 2θ range of 5–75° with a continuous scan rate of 1.0° min^{-1}. The Nitrogen adsorption desorption experiments were performed with a Quantachrome Autosorb-1-1C automated adsorption system. The samples were treated at 150°C for 6 h under helium prior to measurement. X-ray photoelectron spectroscopy (XPS) was done on a PHI model 590 spectrometer with multiprobes (ΦPhysical Electronics Industries Inc.), using Al-K radiation (λ= 1486.6 eV) as the radiation source and was fitted using CasaXPS software (version 2.3.12). The powder samples were pressed on carbon tape mounted on adhesive copper tape stuck to a sample stage placed in the analysis chamber. For correction of surface charging, the C 1s photoelectron line at 284.6 eV was taken as a reference. A mixture of Gaussian (70%) and Lorentzian (30%) functions was used for the least-squares curve fitting procedure.

4.3.3 Catalytic Activity Measurements

4.3.3.1 Reaction procedure of oxidative aromatization:

In a typical reaction, a mixture of 1,2,3,4-tetrahydroquinoline (0.25 mmol), meso MnO_x (25 mg) and DMF (5 mL) was added in a 25 mL round bottom flask (two-necked flask was used for time dependent study) equipped with a condenser. The reaction mixture was heated to reflux under vigorous stirring (700 rpm) for the required time under an air balloon. After reaction, the mixture was cooled and the catalyst was removed by filtration. The product analysis was done using GC-MS (gas chromatography-mass

spectrometry). The conversion was determined based on the concentration of substrate. Most reactions were repeated twice and the average values were used. The products were isolated by filtering off the catalyst followed by evaporation of solvent. For isolation, the reactions have been performed in acetonitrile (at 80°C) for easy solvent evaporation. The isolated products were identified by the ^{1}H NMR and ^{13}C NMR spectra and matched with authentic data from literature.

4.3.3.2 Analysis of reaction products

The GC-MS analyses were performed by a 7820A GC system connected with a mass detector of 5975 series MSD from Agilent Technologies and a nonpolar cross-linked methyl siloxane column with dimensions of 12 in × 0.200 mm × 0.33 µm was used. The ^{1}H and ^{13}C NMR spectra were recorded on a Bruker AVANCE III- 400 MHz spectrometer. ^{1}H NMR spectra were collected at 400 MHz with chemical shift referenced to the residual peak in $CDCl_3$ (δ: H 7.26 ppm). ^{13}C NMR spectra were collected at 100 MHz and referenced to residual peak in $CDCl_3$ (δ: C 77.0 ppm). Multiplicities are written as s (singlet), d (doublet), t (triplet), and m (multiplet).

4.4 Structural characterization of Meso MnO_x

The physicochemical and morphological features of the material were characterized by powder X-ray diffraction (PXRD), and N_2 sorption techniques. The PXRD results (**Figure 4.1A**) reveal absence of distinct diffraction pattern in the wide angle (5° - 75°) range which indicated the poorly crystalline nature of the material at low calcination temperature. The material transformed to the bixbyite (Mn_2O_3) phase with at calcination temperature above 450°C. The mesoporosity of the material was confirmed

by N_2 sorption experiments (**Figure 4.1B**), where a Type IV adsorption isotherm followed by a Type I hysteresis loop was observed irrespective of calcination temperature. The Brunauer–Emmett–Teller (BET) method was used to calculate surface areas of the different Cs-MnO_x materials **(Table 4.1)**. Of the different meso MnO_x materials prepared by controlling calcination temperature, meso-MnO_x-350 exhibited the maximum surface area (226 m^2/g). The pore sizes of meso MnOx were calculated by BJH method from desorption branch of the isotherm. An increse of pore size with rising calcination temperature has been observed.

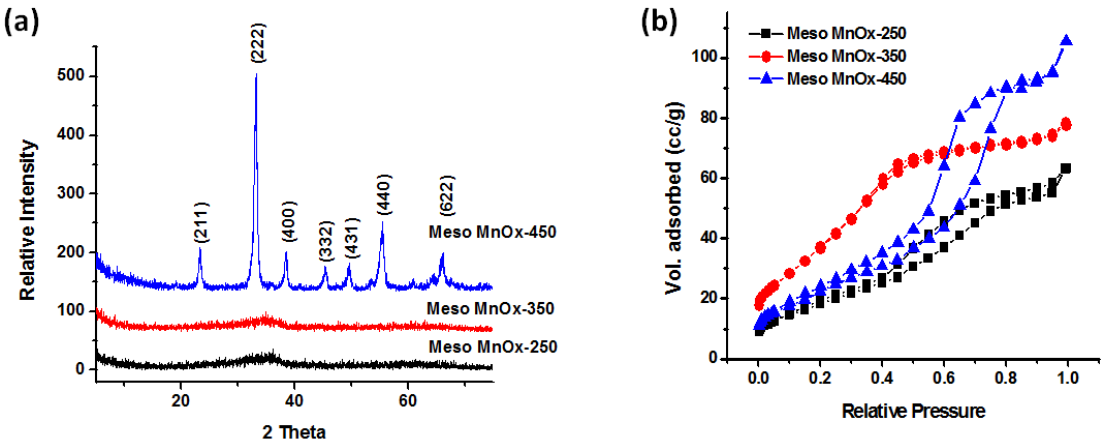

Figure 4.1 (a) Powder X-ray diffraction of meso MnOx at different calcination temperatures. The diffraction patterns at 450°C calcination can be indexed to Mn_2O_3 phase, whereas calcination temperatures at 250°C and 350°C displayed an amorphous nature. (b) Nitrogen adsorption isotherms of meso MnOx at different calcination temperatures. A type IV adsorption isotherm followed by a type I hysteresis loop were observed for all the materials, which confirmed the mesoporous structure.

Table 4.1 Physicochemical properties of meso MnO_x at different calcination temp

Catalyst	Structure	Surface Area S_{BET} (m^2g^{-1})	BJH des. pore size(nm)	Pore volume (cc g^{-1})
Meso MnO_x-250	Amorphous	182	3.4	0.21
Meso MnO_x-350	Amorphous	226	3.4	0.24
Meso MnO_x-450	Mn_2O_3	150	4.3	0.26
Meso MnO_x-550	Mn_2O_3	120	9.6	0.42

4.5 Catalytic reaction

4.5.1 Optimization of reaction condition

Table 4.2 Comparison of catalysts for aromatization of 1,2,3,4-tetrahydroquinoline [a]

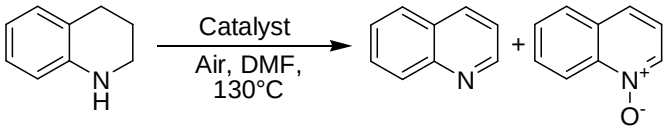

Entry	Catalyst	Catalyst amount (mg)	Conv.[b] (%)	Selec.[b] (%)
1	Meso MnO_x	25	50	>99
2	Meso Cs/MnO_x	25	50	>99
3	K-OMS-2	25	65	70
4	AMO	25	60	90
5	C-Mn_2O_3	25	1	>99
6	No	0	1	>99
7	Meso MnO_x	5	11	>99
8	Meso MnO_x	10	25	>99
9	Meso MnO_x	50	80	>99

[a] Reaction conditions: 1,2,3,4-tetrahydroquinoline (0.25 mmol), catalyst (required amount), DMF (5 mL), 130°C, air balloon, 5 h. [b] Conversions and selectivity were determined by GC-MS based on concentration of 1,2,3,4-tetrahydroquinoline.

To examine the activity of the manganese oxide catalysts we initially selected 1,2,3,4-tetrahydroquinoline as the test substrate. In a comparative study, 1,2,3,4-tetrahydroquinoline was reacted with different phases of well-known manganese oxide materials for oxidation reactions. The mesoporous manganese oxide material (meso MnOx), prepared by an inverse micelle templated self-assembly method provided a 50% conversion with >99% selectivity to the target compound quinolone in aerobic conditions (Table 4.2, Entry 1). No improvement of activity was observed by introducing Cs promoter ions (Table 4.2, Entry 2). Relatively higher conversions were achieved using two other active manganese oxide phases, octahedral molecular sieves (K-OMS-2) and amorphous manganese oxide (AMO), however selectivity decreased significantly due to formation of N-oxide by over oxidation (Table 4.2, Entries 3 and 4). Notably, a reaction with commercial nonporous Mn_2O_3 gave negligible conversion, similar to catalyst-free conditions (Table 4.2, Entries 5 and 6). The continual increase of performance with catalyst loading (Table 4.2, Entries 7-9) indicates that the system is not suffering from adsorption and mass transfer. The reaction was also surveyed with different solvents of varying polarity. As revealed in Table 4.3, the reaction was facilitated in the presence of polar solvents and N,N-dimethylformamide (DMF) emerged as the best solvent.

Table 4.3 Effect of solvents in aromatization of 1,2,3,4-tetrahydroquinoline

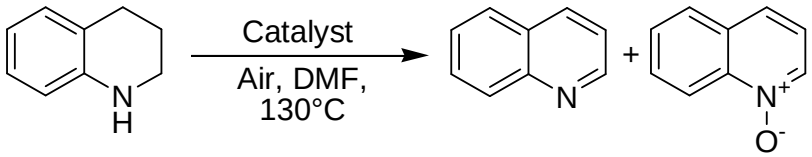

Entry	Solvent	Temperature (°C)	Conversion[b] (%)	Selectivity[b] (%)
1	DMF	130	50	>99
2	Acetonitrile	80	23	>99
3	Dioxane	100	28	>99
4	Toluene	110	15	>99
5	Hexane	60	14	>99

[a] Reaction conditions: 1,2,3,4-tetrahydroquinoline (0.25 mmol), meso MnO_x (25 mg), DMF (5 mL), 130°C, air balloon, 5 h. [b] Conversions and selectivity were determined by GC-MS based on concentration of 1,2,3,4-tetrahydroquinoline.

4.5.2 Comparison with different catalysts

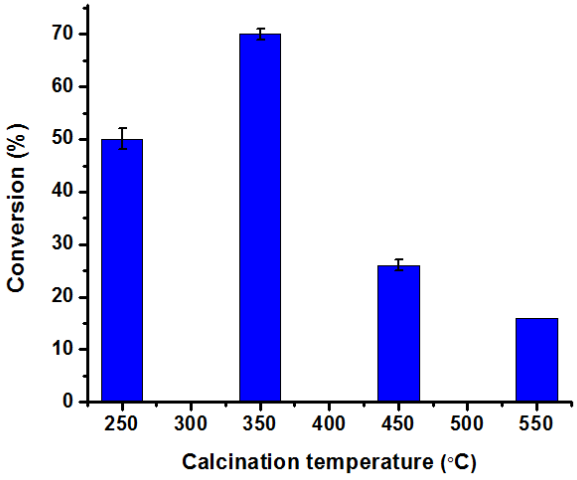

Figure 4.2 Effect of calcination temperature in the performance of meso MnO_x. Reaction condition: 1,2,3,4-tetrahydroquinoline (0.25 mmol), meso MnO_x (25 mg), DMF (5 mL), 130°C, air balloon, 5 h.

The high surface area and nanocrystalline nature of the material is critical for achieving high efficiency. High accessible surface area provides larger amounts of catalytically active sites and thereby promoting activity. The performance of the meso MnO_x material was investigated as a function of calcination temperatures, since calcination has a remarkable effect on the physicochemical properties of the material (Figure 4.2).[29] The highest conversion (72%) was achieved when the materials was calcined to 350°C (highest surface area, 226 m^2g^{-1}) and the conversion decreased significantly when the material was heated to 450°C (26%) and 550°C (16%) due to lowering of surface area (150 and 120 m^2g^{-1} respectively). The presence of mesoporous network is another important factor, as it facilitates the adsorption and diffusion of the substrates. As observed, the commercial non-porous manganese oxide was totally inactive in the present reaction conditions.

4.5.3 Role of oxidants

Table 4.4. Effect of oxidants and additives in aromatization of 1,2,3,4-tetrahydroquinoline

Entry	Oxidant	Additives	Conversion[b] (%)	Selectivity[b] (%)
1	Air	none	50	>99
2	O_2	none	49	83
3[c]	Air	none	25	>99
4[c]	O_2 (10 bar)	none	44	>99
5	N_2	none	18	>99

[a] Reaction conditions: 1,2,3,4-tetrahydroquinoline (0.25 mmol), meso MnO_x (25 mg), DMF (5 mL), 130°C, air balloon, 5 h. [b] Conversions and selectivity were determined by GC-MS based on concentration of 1,2,3,4-tetrahydroquinoline. [c] 10 mg catalyst was used.

While investigating the role of oxidant, we found that reaction under pure molecular oxygen instead of air did not improve the conversion but reduced the selectivity of quinoline due to over oxidation (Table 4.4, Entry 1 and 2). However, conversion was increased significantly under a pressurized oxygen system using lower amounts of catalyst (Table 4.4, Entry 3 and 4). This is due to the higher solubility of oxygen in the solvent under high pressure. The importance of aerobic conditions in the reaction can be seen by a reaction under nitrogen (Table 4.4, Entry 5), which yielded much lower conversion (18%). Therefore, after extensive screening of all reaction parameters, we have selected using of meso MnO_x-350 catalyst under aerobic and additive free condition in DMF at 130°C as the optimal reaction condition.

4.5.4 Reusability and heterogeneity

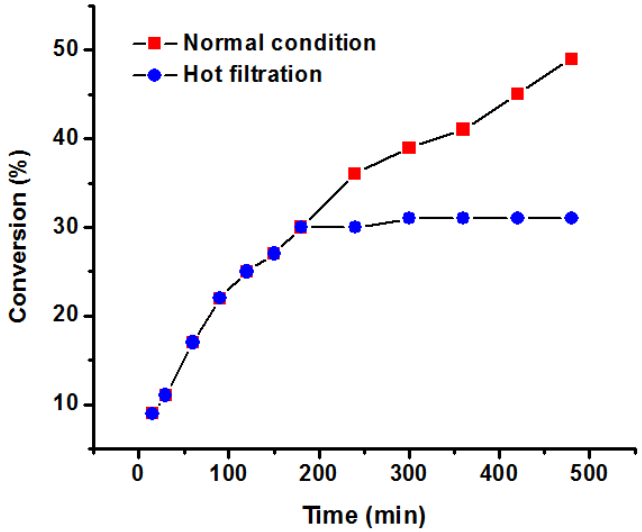

Figure 4.3 Hot filtration test. Reaction condition: 1,2,3,4-tetrahydroquinoline (0.25 mmol), meso MnO_x (25 mg), DMF (5 mL), 130°C, air balloon. Catalyst was removed at 30% conversion (at 3 h).

Preventing deactivation of catalysts due to aggregation and leaching of active metals in solution is a challenge for heterogeneous catalytic systems. In order to verify

the leaching of active metals, we performed hot filtration test of dehydrogenation (Figure 4.3) of 1,2,3,4-tetrahydroquinoline using meso MnO_x. The catalyst was removed from the reaction system after 3 h (at about 30% conversion) and the filtrate was kept in the same reaction condition for next 20 h. No further reaction was observed, which confirmed absence of active metals in the solution. To check the reusability, the catalyst was retrieved from the reaction mixture by simple filtration and washed with excess DMF and ethanol. The catalyst was reactivated at 250°C for 30 min prior to reuse to remove any adsorbed substrates. As observed in Figure 4.4a the catalyst can be reused for at least four times without any loss of activity and selectivity. Additionally, the X-ray diffraction studies confirmed that the amorphous nature of the catalyst was retained after multiple reuse cycles (Figure 4.4b). Therefore, our catalyst is heterogeneous, stable and reusable.

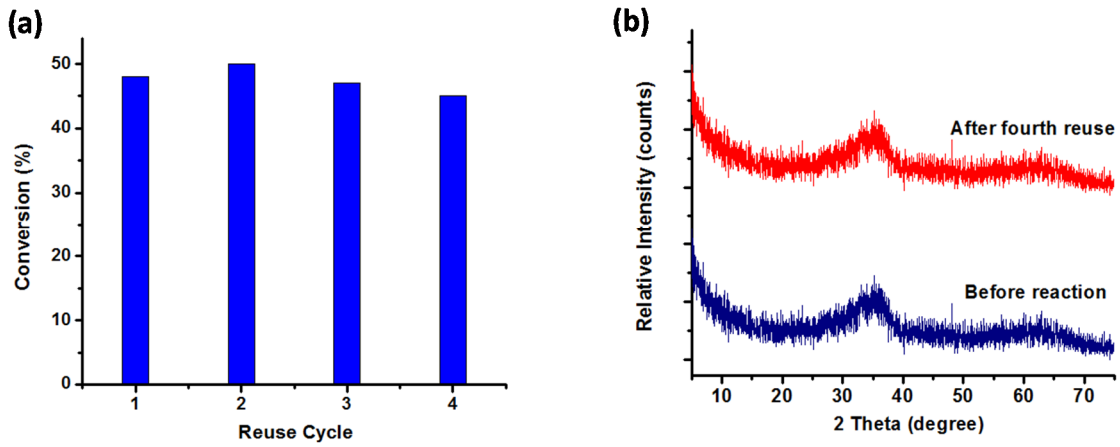

Figure 4.4. (a) Reusability test. Reaction condition: 1,2,3,4-tetrahydroquinoline (0.25 mmol), meso MnO_x (25 mg), DMF (5 mL), 130°C, air balloon, 5 h. (b) PXRD before and after fourth reuse.

4.5.5 Kinetic study

The kinetic aspects of the reaction was determined by conducting a time-dependent study (Figure 4.5). Formation of quinoline N-oxide was observed in trace amounts after 3

h. A first order rate equation was derived with respect to 1,2,3,4-tetrahydroquinoline with a rate constant of 0.00761 min^{-1} (Figure 4.6). A series of time-dependent experiments were performed in the temperature range of 80 - 140°C. The apparent activation energy was estimated as 8.3±0.2 kcal mol^{-1} using Arrhenius equation (Figure 4.7).

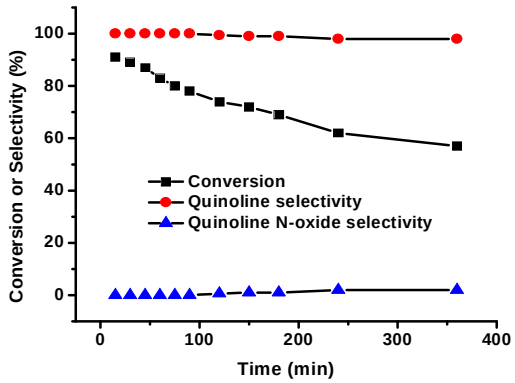

Figure 4.5 Time dependent study. Reaction condition: 1,2,3,4-tetrahydroquinoline (0.25 mmol), meso MnO_x (25 mg), DMF (5 mL), 130°C, air balloon.

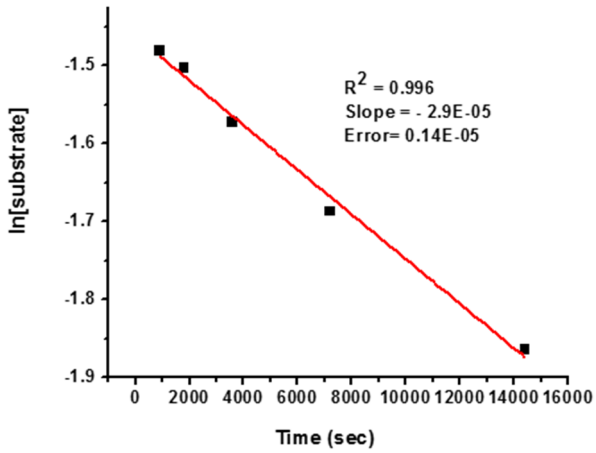

Figure 4.6 Kinetic study. Reaction condition: 1,2,3,4-tetrahydroquinoline (0.25 mmol), meso MnO_x (25 mg), DMF (5 mL), 130°C, air balloon. The reaction depreciated a first order rate with respect to substrate having a rate constant of $3\times10^{-5}\pm0.1\times10^{-5}s^{-1}$.

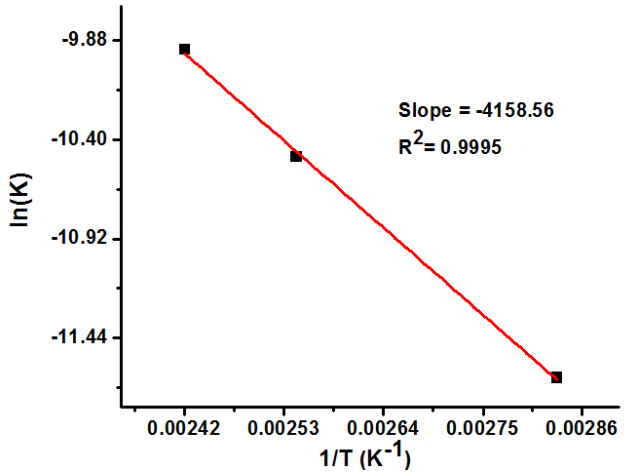

Figure 4.7 Arrhenius plot for the oxidation of 1,2,3,4-tetrahydroquinoline by meso MnO_x. The apparent activation energy was estimated as 8.3±0.2 Kcal mol^{-1}. Reaction condition: 1,2,3,4-tetrahydroquinoline (0.25 mmol), meso MnO_x (25 mg), DMF (5 mL), 5 h, air balloon. K: rate constant.

4.5.6 Substrate scope and functional group tolerability

While evaluating the substrate scope, we found that this methodology works well for diverse N based aromatic heterocycles. The products can be isolated easily by filtration followed by solvent evaporation. Isolated yields of some of the aromatized products along with their NMR spectra are provided (see supporting information). Presence of electron donating substituents in the aromatic ring of 1,2,3,4-tetrahydroquinoline did not alter the catalytic activity (Entry 2 and 3, Table 2). It is notable that the present protocol can be applicable to functional group containing electron lone pairs (OMe), which is inactive in the boron based catalytic system due to coordination, as mentioned by Kojima *et al.*[7] Presence of electron withdrawing group (NO_2) in the aromatic ring resulted moderate (70%) conversion (Entry 5, Table 2). These results suggested that the catalytic efficiency depends on the nature of substituents in the

aromatic ring of 1,2,3,4-tetrahydroquinoline. Substitution at 2 position of the saturated ring of 1,2,3,4-tetrahydroquinoline resulted lower conversion due to induced steric effect, which retards the abstraction of α C-H hydrogen (Entry 5, Table 2). Quinoxaline and indole derivatives are representative structural motifs in biologically and pharmaceutically relevant molecules.[11,30] The oxidative dehydrogenation method by meso MnOx could be an attractive synthetic route for preparation of quinoxaline and indole. As observed, a substituted 2-methylindoline and a saturated 1,2,3,4-tetrahydroquinoxaline can be effectively aromatized with quantitative conversion (>99%) and selectivity (Entry 6 and 7, Table 2). The excellent functional group tolerance of the present protocol can be exhibited by oxidative aromatization of Hantzsch ester, which yielded the desired aromatic product with quantitative conversion (>99%) and excellent selectivity (>99%) in lower temperature and shorter reaction time (Entry 8, Table 2).

Table 4.5 Oxidation of N-heterocycles by meso MnO_x [a]

Entry	Substrate	Product	Conv.[b] (%)	Selec.[b] (%)	TON[c]
1	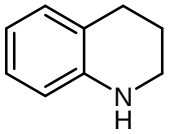	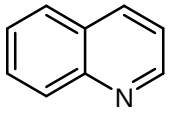	>99	95	1.7
2	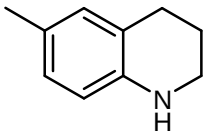	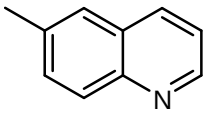	>99	>99	1.7
3	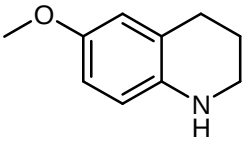	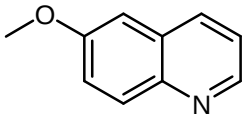	>99	93 (89)	1.7
4	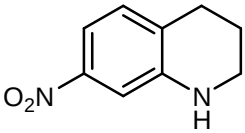	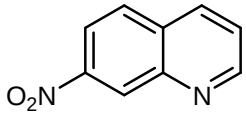	70	>99	1.4
5	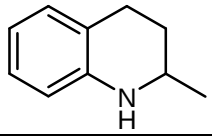	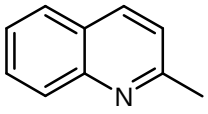	80	>99	1.5

6	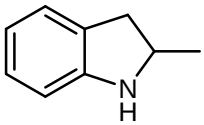	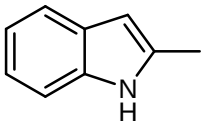	>99	>99	1.7
7	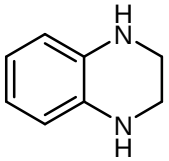	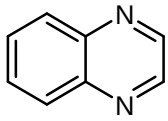	>99	>99 (92)	1.7
8 [d]	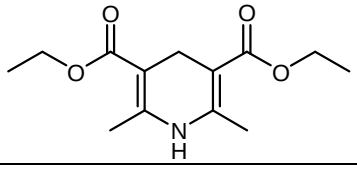	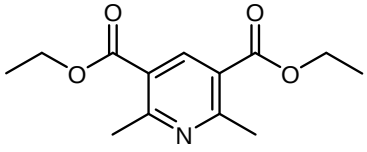	>99	>99(94)	1.7

[a] Reaction conditions: substrate (0.25 mmol), meso MnO_x (25 mg), DMF (3 mL), 130 °C, 20 h, air balloon. [b] Conversion and selectivity was determined by GC-MS. Numbers in parenthesis refer to yields of isolated products. Isolation was carried out in acetonitrile at 80°C. [c] TON = moles of amines converted / moles of catalyst. [d] 120°C and 5 h.

Spectral characterization of isolated aromatized products

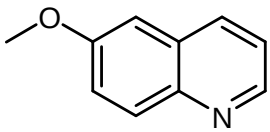

6-methoxyquinoline

Appearance: Yellow oil

^{1}H NMR (400 MHz, Chloroform-*d*) δ 8.76 (dd, *J* = 4.2, 1.5 Hz, 1H), 8.03 (dd, *J* = 19.4, 8.7 Hz, 2H), 7.36 (dt, *J* = 8.2, 3.3 Hz, 2H), 7.06 (d, *J* = 2.8 Hz, 1H), 3.92 (s, 3H).

^{13}C NMR (101 MHz, Chloroform-*d*): δ 158.02, 147.77, 144.21, 135.35, 130.57, 129.58, 122.71, 121.59, 105.34, 55.70.

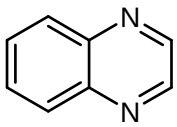

Quinoxaline

Appearance: Yellow oil

^{1}H NMR (400 MHz, Chloroform-d) δ 8.84 (s, 1H), 8.11 (dd, J = 6.4, 3.5 Hz, 1H), 7.78 (dd, J = 6.4, 3.4 Hz, 1H).

^{13}C NMR (101 MHz, Chloroform-*d*) δ 145.21, 130.32, 129.75.

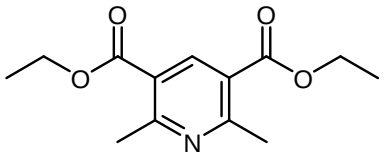

Diethyl 2,6-dimethylpyridine-3,5-dicarboxylate

Appearance: White powder

^{1}H NMR (400 MHz, Chloroform-*d*) δ 8.59 (s, *J* = 2.4Hz, 1H), 4.32 (m, *J* = 2.4Hz, 4H), 2.76 (d, *J* = 2.5 Hz, 6H), 1.34 (td, *J* = 2.5 Hz, 6H).

^{13}C NMR (101 MHz, Chloroform-*d*) δ 160.06, 162.35, 141.01, 123.19, 61.51, 25.09, 14.41.

4.6 Discussion

This study featured catalytic aerobic oxidative aromatization of saturated N-heterocycles in presence of meso MnOx material. Diverse heterocyclic derivatives were converted to the corresponding aromatized products efficiently. According to the report of Beller and co-workers, the reaction is initiated by forming a radical intermediate by transfer of electron from 1,2,3,4-tetrahydroquinoline to the metal center of the catalyst. By introducing a radical scavenger 2,6-Di-*tert*-butyl-4-methylphenol in the reaction mixture, we were able to trap the radical intermediate as observed from the GC-MS. This result suggested a similar reaction pathways for our system as observed by Beller *et al.*[23] The radical species was formed by an electron transfer to the active Mn centers followed by α C-H dehydrogenation to form an imine (C=N) intermediate (Scheme 4.2). The final aromatized product was formed by a tautomerism and another dehydrogenation from the cyclic imine fragment.

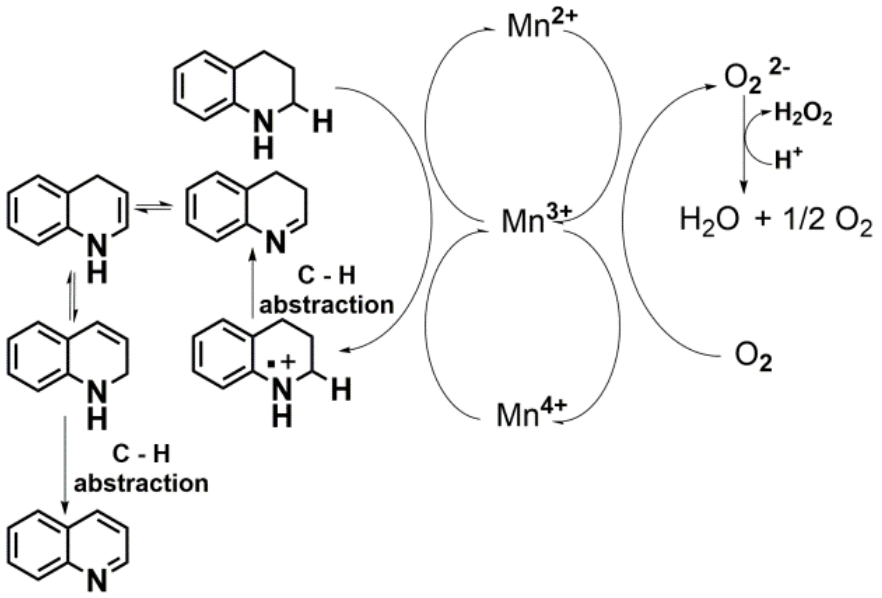

Scheme **4.2** Proposed mechanism of aromatization of 1,2,3,4-tetrahydroquinoline

The formation of the radical intermediate resulted reduction of surface active Mn centers, which lead to release of labile lattice oxygen. Under catalytic turnover conditions, the reduced Mn species can be re-oxidized by dioxygen with production of H_2O_2, which could be easily decomposed to water over manganese oxide.[31] The aerobic atmosphere is critical as loss of lattice oxygen should be replenished by the aerial oxygen. This is consistent with the observation of lower catalytic efficiency under nitrogen atmosphere (18% conversion) compared to aerobic conditions (50% conversion). Additionally, we characterize the used material by XPS after reaction under nitrogen atmosphere (Figure 4.8). The significant decrease (22.8%) in lattice oxygen (O_s) amounts compared to the bare material (62.6%) indicates the presence of oxygen vacancies due to incomplete replenishment under nitrogen atmosphere (Table 4.6). Whereas, from the Mn 2p spectra, a mixture of Mn valency (a higher Mn oxidation state at 642.5 eV and a lower Mn oxidation state at 639.4 eV)[32] was observed due to incomplete re-oxidation of reduced Mn species under nitrogen atmosphere. These results

suggested our proposed mechanism of multielectron transfer among the Mn centers with involvement of labile lattice oxygen in the catalytic cycle.

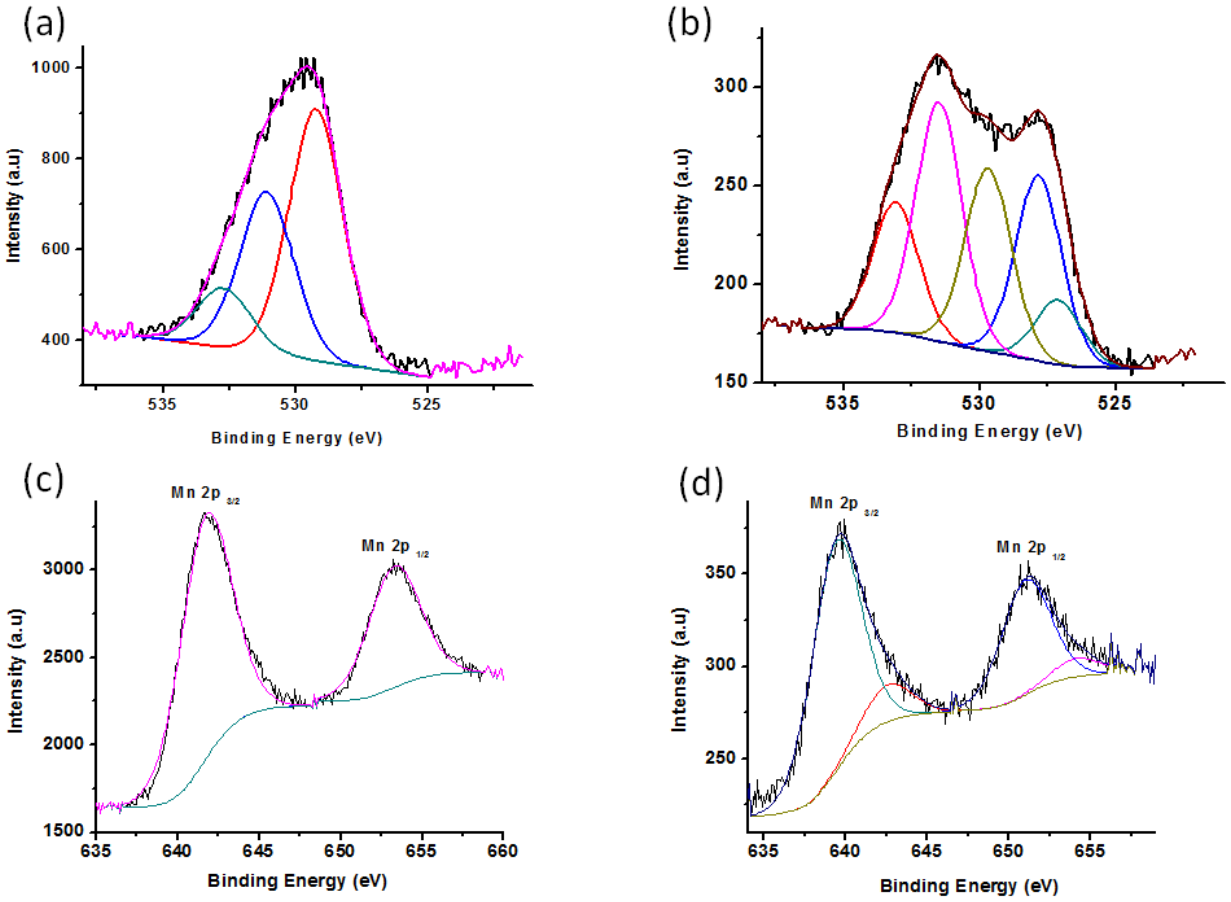

Figure 4.8 XPS of meso MnOx. O 1s (a) before reaction and (b) after reaction under nitrogen. And Mn 2p (c) before reaction and (d) after reaction under nitrogen.

Table 4.6 Summary of XPS results

Meso MnOx	Mn (eV)				O_s		O_{ads}		O_{mw}	
	$2p_{3/2}$		$2p_{1/2}$		BE (eV)	%Area	BE (eV)	%Area	BE (eV)	%Area
Before reaction	641.7	-	652.4	-	529.2	62.6	530.9	27.3	532.8	9.9
Reaction under N_2	639.4	642.5	651.0	654.0	529.6	22.8	531.4	29.7	533.0	16.26

The reaction pathways were further verified by a reaction with a double substituted tetrahydroquinoline derivative (1,2,3,4-Tetrahydro-2,2,4,7-tetramethylquinoline), where no reaction with the catalyst was observed (Scheme 4.3). This suggested that an α C-H dehydrogenation removal is essential in order to form the cyclic imine intermediate. This is also in agreement with the rate acceleration by presence of NHPI, which is known for C-H removal from hydrocarbons. Additionally, a reaction of 1,2,3,4-tetrahydronaphlthalene only produced the oxidized products (corresponding alcohol and ketone) with negligible conversion (Scheme 4.4) indicating that direct C-C dehydrogenation is unlikely to occur in present reaction system. Therefore, the presence of N in the saturated cyclic alkane part is necessary in order to begin the reaction by transferring electron to the Mn center.

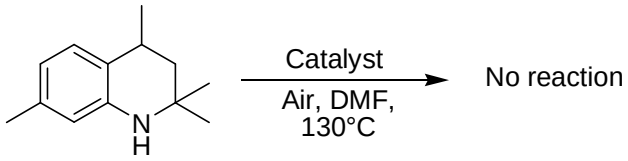

Scheme 4.3 Reaction with a 1,2,3,4-tetrahydroquinoline derivatives having double substitution at alpha position. Reaction procedure: 1,2,3,4-Tetrahydro-2,2,4,7-tetramethylquinoline (0.25 mmol) meso MnO_x (25 mg), DMF (5 mL), 130°C, air balloon, 5 h.

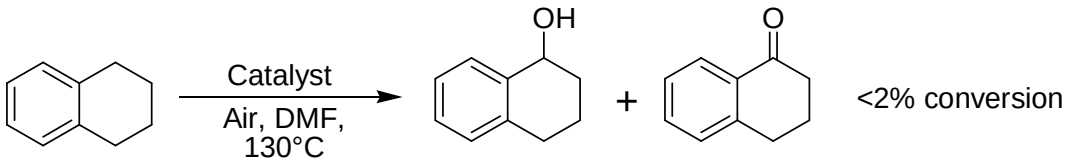

Scheme 4.4 Reaction with 1,2,3,4-tetrahydronaphlthalene. Reaction procedure: 1,2,3,4-tetrahydronaphlthalene (0.25 mmol) meso MnO_x (25 mg), DMF (5 mL), 130°C, air balloon, 5 h.

4.7 Conclusion

In summary, we demonstrated a heterogeneous, cost-effective and mild reaction procedure for oxidative aromatization of diverse nitrogen heterocycles with easily abundant manganese oxide materials. Air as the terminal oxidant, absence of precious metals and ligand additives, along with excellent catalyst reusability and easy isolation of the aromatized products make our catalytic protocol green and environmentally benign. The mechanistic studies invoked a Mn-mediated radical species formation, followed by two successive dehydrogenation and tautomerism. Although the optimal condition required high temperature (130°C) and DMF as solvent, the reaction indeed succeeded even at much lower temperature (80°C) in acetonitrile with formation of desired product in >95% yield if higher amounts of catalyst was used. High surface area, nanocrystalline nature and involvement of labile lattice oxygen were considered also as important factors for this oxidation methodology.

4.8 References

(1) Deiters, A.; Martin, S. F. *Chem. Rev.* **2004**, *104*, 2199-2238.

(2) Vitaku, E.; Smith, D. T.; Njardarson, J. T. *Journal of medicinal chemistry* **2014**, *57*, 10257-10274.

(3) Chakraborty, S.; Brennessel, W. W.; Jones, W. D. *J. Am. Chem. Soc.* **2014**, *136*, 8564-8567.

(4) Yamaguchi, R.; Ikeda, C.; Takahashi, Y.; Fujita, K.-i. *J. Am. Chem. Soc.* **2009**, *131*, 8410-8412.

(5) Fujita, K.-i.; Tanaka, Y.; Kobayashi, M.; Yamaguchi, R. *J. Am. Chem. Soc.* **2014**, *136*, 4829-4832.

(6) Wu, J.; Talwar, D.; Johnston, S.; Yan, M.; Xiao, J. *Angew. Chem.* **2013**, *125*, 7121-7125.

(7) Kojima, M.; Kanai, M. *Angew. Chem.* **2016**, *128*, 12412-12415.

(8) Talwar, D.; Gonzalez-de-Castro, A.; Li, H. Y.; Xiao, J. *Angew. Chem., Int. Ed.* **2015**, *54*, 5223-5227.

(9) Yao, W.; Zhang, Y.; Jia, X.; Huang, Z. *Angew. Chem., Int. Ed.* **2014**, *53*, 1390-1394.

(10) Wendlandt, A. E.; Stahl, S. S. *J. Am. Chem. Soc.* **2013**, *136*, 506-512.
(11) Wendlandt, A. E.; Stahl, S. S. *J. Am. Chem. Soc.* **2014**, *136*, 11910-11913.
(12) Evans, D. L.; Minster, D. K.; Jordis, U.; Hecht, S. M.; Mazzu Jr, A. L.; Meyers, A. *J. Org. Chem.* **1979**, *44*, 497-501.
(13) Zhou, W.; Taboonpong, P.; Aboo, A. H.; Zhang, L.; Jiang, J.; Xiao, J. *Synlett* **2016**.
(14) Wendlandt, A. E.; Stahl, S. S. *Angew. Chem., Int. Ed.* **2015**, *54*, 14638-14658.
(15) Yamaguchi, K.; Mizuno, N. *Angew. Chem., Int. Ed.* **2003**, *42*, 1480-1483.
(16) Damodara, D.; Arundhathi, R.; Likhar, P. R. *Adv. Synth. Catal.* **2014**, *356*, 189-198.
(17) Amende, M.; Gleichweit, C.; Werner, K.; Schernich, S.; Zhao, W.; Lorenz, M. P.; Höfert, O.; Papp, C.; Koch, M.; Wasserscheid, P. *ACS Catal.* **2014**, *4*, 657-665.
(18) Furukawa, S.; Suga, A.; Komatsu, T. *Chem. Commun.* **2014**, *50*, 3277-3280.
(19) So, M. H.; Liu, Y.; Ho, C. M.; Che, C. M. *Chemistry–An Asian Journal* **2009**, *4*, 1551-1561.
(20) Jawale, D. V.; Gravel, E.; Shah, N.; Dauvois, V.; Li, H.; Namboothiri, I. N.; Doris, E. *Chem. Eur. J.* **2015**, *21*, 7039-7042.
(21) Yuan, H.; Yoo, W.-J.; Miyamura, H.; Kobayashi, S. *J. Am. Chem. Soc.* **2012**, *134*, 13970-13973.
(22) Ge, D.; Hu, L.; Wang, J.; Li, X.; Qi, F.; Lu, J.; Cao, X.; Gu, H. *ChemCatChem* **2013**, *5*, 2183-2186.
(23) Cui, X.; Li, Y.; Bachmann, S.; Scalone, M.; Surkus, A.-E.; Junge, K.; Topf, C.; Beller, M. *J. Am. Chem. Soc.* **2015**, *137*, 10652-10658.
(24) Iosub, A. V.; Stahl, S. S. *Org. Lett.* **2015**, *17*, 4404-4407.
(25) Biswas, S.; Dutta, B.; Mullick, K.; Kuo, C.-H.; Poyraz, A. S.; Suib, S. L. *ACS Catal.* **2015**, *5*, 4394-4403.
(26) Biswas, S.; Poyraz, A. S.; Meng, Y.; Kuo, C.-H.; Guild, C.; Tripp, H.; Suib, S. L. *Appl. Catal., B: Environ.* **2015**, *165*, 731-741.
(27) Biswas, S.; Mullick, K.; Chen, S.-Y.; Kriz, D. A.; Shakil, M.; Kuo, C.-H.; Angeles-Boza, A. M.; Rossi, A. R.; Suib, S. L. *ACS Catal.* **2016**, *6*, 5069-5080.
(28) Dutta, B.; Biswas, S.; Sharma, V.; Savage, N. O.; Alpay, S.; Suib, S. L. *Angew. Chem.* **2016**, *128*, 2211-2215.
(29) Poyraz, A. S.; Kuo, C.-H.; Biswas, S.; King'ondu, C. K.; Suib, S. L. *Nat. Commun.* **2013**, *4*.
(30) Seitz, L. E.; Suling, W. J.; Reynolds, R. C. *Journal of medicinal chemistry* **2002**, *45*, 5604-5606.
(31) Makwana, V. D.; Son, Y.-C.; Howell, A. R.; Suib, S. L. *J. Catal.* **2002**, *210*, 46-52.
(32) Genuino, H. C.; Dharmarathna, S.; Njagi, E. C.; Mei, M. C.; Suib, S. L. *J. Phys. Chem. C* **2012**, *116*, 12066-12078.

CHAPTER 5. FUTURE PERSPECTIVE

Catalysis plays a vital role in the chemical industry in terms of economic viability and environmental sustainability. Traditionally, the catalysts can be subdivided in two categories: homogeneous (reactant and catalyst in same phase) and heterogeneous (reactant and catalyst in different phase). The catalytic active sites of homogeneous catalysts are clearly defined and controlled, which makes them intrinsically active and selective. Moreover, they can overcome mass transfer limitation and thereby can operate at low and moderate temperature. However, the stability of homogeneous catalysts and their cumbersome preparation procedures are some drawbacks, especially when used in large scale reactions. In this regard, due to the advantages of easy separation, notable stability in harsh conditions and proper reusability make heterogeneous catalysis favorable to the chemical industry. However, the development of efficient heterogeneous catalysts has been hindered by the limited knowledge of active sites, which resulted unwanted side reactions to limit the synthesis utility of a chemical reaction. The nature of catalytically active sites are difficult to predict for traditional metal oxides or supported metal particle based heterogeneous catalysts, as it depends on many factors including, surface area, nanoparticle dispersion and exposure of active surface atoms. However, irrespective of the nature, catalysis is primarily a molecular phenomenon since it involves the chemical transformation of molecules into other molecules. Therefore, fundamental knowledge of reaction mechanism in critical for designing diverse types of catalysts. In this research we extensively studies the reaction mechanism (catalytic cycles, role of metal centers, nature of the intermediates and kinetic analyses) of both homogeneous and heterogeneous catalytic reactions.

In chapter 2, we focused on a typical inorganic metal-ligand homogeneous catalysts for CO_2 reduction reactions. The reaction steps have been evaluated and the reactivity was correlated with the nature of the ligand and the metal-ligand environment. As a future perspective, the developed homogeneous Re complexes can be grafted on a solid support to develop a hybrid homogenous-heterogeneous catalyst. By designing that, we can retain the activity of the Re complexes as it's homogeneous form, whereas the advantages of the heterogeneous catalysts can be introduced by easy separation from the reaction medium. Proper selection of ligand and optimization of synthesis condition is necessary for designing of the catalysts. Moreover relatively easier ligand synthesis procedure described in our research may encourage design of functionally diverse set of metal-ligand systems by introducing suitable substitution on ligand framework. Additionally, Much has to be done on substitution of active metal center from Rhenium (Re) to low cost and abundant metal sources like Manganese, Cobalt or Iron; the consequence being more acceptability in industrial application. Theoretical calculations and mechanistic understanding will shed light onto structure-activity relationship and hence design of superior molecular catalysts would be possible.

The heterogeneous mesoporous copper manganese oxide described in chapter 3 can be applied to other Cu based coupling reactions. Our thorough analyses of the catalytic cycles will be a benchmark for developing Cu base heterogeneous catalysts as the catalytic cycles we described (phenol co-ordination, oxidative addition and reductive elimination) typically studied in homogeneous systems only. Our study showed a synergy between homogeneous and heterogeneous catalysis, where we discussed the role of oxide surface as a ligand to distribute the charge of the metal center. In future, the study can be further extended to other

active metal supported mesoporous metal oxide catalysts. One promising candidate is supported Au-based catalysts. Au nanoparticles have attracted interests in numerous catalytic reactions such as low-temperature oxidation of CO, hydrochlorination of alkyne, and liquid phase oxidation of alcohols. The biggest problem of using Au based catalysts are their instability, due to agglomeration of Au nanoparticles. The high surface area mesoporous manganese oxide material descried here can be a promising support for Au nanoparticles. As an added advantage, in case of Au mediated catalytic oxidation reactions, manganese oxide can also act as a co-catalyst, where a synergy between Au and manganese oxide can make the reaction more facile.

The developed catalytic oxidation methodologies described in chapter 4 maintain the 'source reduction', the fundamental goal of 'green chemistry'. The mesoporous manganese oxide materials were able to produce aromatic N-based heterocycles using heterogeneous catalytic pathways. Proper reusability, less waste generation, air as oxidant and atmospheric conditions are the key parameters of the catalytic protocol. The synthesis protocols can be applied to other metal oxide based materials such as cobalt and iron oxide. One possible extension can be synthesized mesoporous mixed-metal oxides using two or more active metal sources (Mn-Fe, Mn-Co or Mn-Ni). Mixed-metal oxide materials are typically more active in catalytic reactions than a single metal oxides due to introduction of different surface properties, and synergetic effect. As observed in our case, a heterocycle is present in the substrate to initiate the reaction by transferring the electron to the active Mn centers. We also found that direct C-C bond activation by H atom abstraction is a challenge. The mesoporous mixed-metal oxide can be utilized in direct C-C bond activation reactions since they will be more active than a single metal oxide based catalysts.